

Principal component analysis of trace element data from the Upper Zone of the Bushveld Complex: constraints on possible tectonic provenance

By

Selby Sebola

Submitted in partial fulfilment of the requirements for the degree:

Master of science in Geology

In the Faculty of Natural & Agricultural Sciences
University of Pretoria
Pretoria

2nd of January 2023

DECLARATION OF ORIGINALITY

I, Selby Sebola declare that this research project, which I hereby submit for the degree Master of science in Geology at the University of Pretoria, is my own work and has not previously been submitted by me for a degree at this or any other tertiary institution.

SIGNATURE

DATE

ABSTRACT

The Kaapvaal Craton in South Africa is characterised by ultramafic to mafic complexes, and several mafic intrusions are associated closely with different sections of the craton. The focus of this research is the Transvaal basin in the Kaapvaal Craton that hosts the Bushveld Complex. This complex is the most extensive mafic layered intrusion on Earth, with the magmas ranging from Fe-rich to Si-rich. The extensive body of research on this area is a good foundation for the current study, which focuses on the Upper Zone and upper Main Zone (UUMZ) of the complex. The Bushveld Complex is endowed with rich mineral deposits, lending it robust economic significance, allowing substantial contributions to the global economy through various avenues relating to mineral processing and distribution.

Objectively, this research project seeks to provide tectonic constraints on the origin of the magma emplaced in the UUMZ through geochemical analyses of trace elements and rare earth element (REE) data from Bierkraal boreholes (western limb) and Magnetite Layer 21 (eastern limb), respectively. In this research approach, the geochemistry of basaltic rocks is considered a predictive indicator in determining the likely tectonic setting in which the parental magma originated. A global database of basaltic rock data was employed for this project, namely the GEOROC database, which was subdivided according to tectonic settings (convergent plate margin, oceanic island, submarine ridge, and oceanic plateau) for comparing the geochemical signatures against that of the Bushveld Complex. The overall data were analysed following a multidisciplinary approach, i.e. combining geostatistics and programming. Principal component analysis (PCA) was conducted of the Bierkraal trace element data (sampled in the western limb of the complex) by employing various software applications to generate a probability distribution function of the variables, i.e. the trace elements in this context. Initially, PCA identifies the elements that impart the most significant variation to the dataset. These elements function as indicators and identifiers of specific geological and chemical processes.

Overall, the geochemical data from the Bierkraal area and those from Layer 21 are crucial for narrowing down the potential tectonic settings exhibiting similar signatures. The settings and locations most synonymous to those of the Bushveld appear to be those of the Kaula and Nihau islands of Hawaii. In addition, Hawaii data exhibit more depletions in elements such as Nb and Y relative to those of the UUMZ of the Bushveld Complex. The same data show overlaps with data from the Fiji and Tonga islands. These oceanic island-island arc settings are influenced primarily by mantle hotspots/plumes. On the other hand, the REE apatite data show a more generalised overlap with most identified tectonic settings within arc-related settings. The geochemical signatures showing the most similarity are those from the lower 300 m segment of the Upper Zone, characterised by multiple magnetite layers, and those from the East Scotia Ridge spreading centre, located approximately 1 288 km to the east of the tip of South America. This ridge is a back-arc tectonic environment associated with diverging plate motions and subsequent rifting, allowing molten rock to push upward and build new crust. Both geochemical signatures from the Bierkraal trace element data and REE apatite data can be related to an enriched magmatic source (i.e. E-MORB). Conventionally, an enriched geochemical signature is associated with magma derived from the lower parts of the mantle. However, taking the geological location and age of the Bushveld complex into consideration, the E-MORB geochemical signature identified in the Upper Zone could be created by the melting of Archaean crust during the upwelling of depleted (N-MORB) magma.

ACKNOWLEDGEMENTS

I would like to thank my project supervisor, Professor Richard James Roberts (who prefers to be called James), for the support, input, and valuable insights I received during this research project. I thank IMDEX ioGAS™, Dr Lorenzo Milani, and Noleen Pauls for helping me to access the software. Special thanks are due to Dr Susan Winkler for her time and geological conversations on some theories and ideas. Thank you to my housemates (Vongani and Nhlalala) for their support and patience over the last 18 months. I particularly thank my family (my father and mother and my sisters, Tsumbedzo and Candy) for their understanding and support throughout the research project. Thank you for being patient with me.

TABLE OF CONTENT

DECLARATION OF ORIGINALITY	i
ABSTRACT.....	ii
ACKNOWLEDGEMENTS.....	iii
TABLE OF CONTENT	iv
LIST OF FIGURES.....	vi
LIST OF TABLES.....	ix
LIST OF ACRONYMS AND SYMBOLS	x
INTRODUCTION.....	1
GEOLOGICAL SETTING AND BACKGROUND	7
Development of the Kaapvaal Craton.....	8
Stratigraphy of the Kaapvaal Craton.....	13
Pongola Supergroup	8
Witwatersrand Supergroup	14
Ventersdorp and Transvaal supergroups.....	15
Waterberg and Soutpansberg groups.....	16
Bushveld Complex.....	17
Formation and intrusion of the Bushveld Complex	18
Rustenburg Layered Suite	20
Upper Zone	22
Western Bushveld Complex.....	24
Background to Bierkraal data	25
Eastern Bushveld (complimentary REE data).....	27
METHODOLOGY	28
Data description.....	28
Bierkraal borehole	28
Sampling.....	29
Data processing.....	31
Brief introduction to Principal component analysis	32
RESULTS	34
Comparison of Bierkraal trace element data to identified settings	40
Rare earth element data (apatite)	44
DISCUSSION.....	50
Discriminant diagrams (Bierkraal trace element data).....	50

Background to identified tectonic settings.....	57
Arc-related volcanism	57
Oceanic island volcanism	60
Implications of the results for the potential tectonic environment	68
Apatite rare earth element data from Magnetite Layer 21.....	70
Geochemical overlaps and discrepancies	72
E-MORB source vs Archaean crustal input	74
SUMMARY AND CONCLUSIONS	75
REFERENCES	79

LIST OF FIGURES

Figure 1 shows a disentangled map of the Bushveld Complex, with the red box indicating the location of the Bierkraal farm (study area) as per Yuan et al. (2017).

Figure 2 shows the distribution of mid-ocean ridge basalts, ocean island basalts, arc-related basalts, and Large Igneous Provinces after NGS (1999); Wignall (2001); Bryan & Ernst (2008); Xia et al. (2014).

Figure 3 shows the localities in the Kaapvaal Craton. The thick dashed line represents the geophysical boundary of the craton. The terrain boundaries were inferred and situated to coincide with the lineaments (Colesberg and Thabazimbi-Murchison), shear zones (Hout-River and Palala) and fault (Inyoka) identified, as per Eglington and Armstrong (2004).

Figure 4 shows the distribution of volcanic, plutonic, and sedimentary rocks in different periods during the evolution of the Kaapvaal Craton. The Bushveld Complex is shown in panel K, using additional colours, due to its significance in this study (modified after Eglington and Armstrong, 2004).

Figure 5. A stratigraphic column/sequence shows rock units in the Kaapvaal Craton, Southern Africa (after Condie and Wronkiewicz, 1990).

Figure 6 shows a simplified map of the Bushveld Complex, with the different stratigraphic units coded. The accompanying legend shows the ages of the lithologies as per Bamisaiye (2015, PhD thesis).

Figure 7 shows a section through the Rustenburg Layered Suite on the left, agglomerated with the Bierkraal drill cores from the Upper and Main zones on the right as per Tegner et al. (2006).

Figure 8 is a simplified stratigraphic column of the Upper Zone and upper Main Zone (UUMZ). It highlights the location of the Pyroxenite Marker (PM), magnetite layers, mineral variations, and the relatively constant Sr isotopic ratios (Cawthorn & Walraven, 1998).

Figure 9 (a) shows a simplified map of the Bushveld Complex, with the red area indicating the locations of BK3, BK1, and BK3. (b) Stratigraphic column through the Upper Zone of the Bushveld, with the appearance of apatite in UZc. Olivine in UZb and titanium-bearing magnetite in UZc, as per Yuan et al. (2017), categorize the different subzones.

Figure 10 is a sketch of the correlation between the three boreholes (BK1, BK2, and BK3) as per Britt (2015; MSc).

Figure 11 is a map of the western and far western limbs of the Upper Zone of the RLS close to Rustenburg. The map also shows the locations of BK2, BK2, and BK3 (Britt, 2015; MSc).

Figure 12a shows the locations of the drill holes in the Bierkraal farm. (b) shows the stratigraphic locations with depth for the boreholes as earlier modified after Barnes & Maier (2002) and Yuan et al. (2017).

Figure 13. Sample location frequencies, with the colour's olive, blue, green, and black representing Ryukyu, Mariana, Scotia, and Tonga arcs, respectively. Additionally - orange, grey, and sky blue represent the Caribbean-Colombian, Kerguelen, and Manihiki plateaus, while yellow (Hawaiian islands), pink (Ninety East Ridge), and red (Upper Zone).

Figure 14 is a 2D biplot representing the first (PC1) and second (PC2) principal components, with the black arrow indicating the Upper Zone data (red). Note that the following locations are distinguished by the corresponding colours: Mariana (blue), Tonga (black), Scotia (green), Hawaii (yellow), Manihiki (light blue), Ryukyu (olive green), Ninety East Ridge (pink), Caribbean Colombian (orange) and Kerguelen (grey)

Figure 15 shows a scree plot of the eigenvalues generated by the principal components.

Figure 16 a and b are eigenvector plots for the first (PC1) and second (PC2) principal components of the dataset.

Figure 17. MORB normalized trace element concentration plot (modified after Gale et al., 2013) sampled from convergent margins around Tonga (dark-grey colour), with (a) Tonga islands (b) Rochambeau ridge–Lau basin (c) Northwest spreading centre (d) Niuafu 'ou-Lau basin (e) Fonualei spreading centre (f) Eastern Lau spreading centre (g) Central Lau spreading centre (h) Fiji Islands. Note that the red line represents Bierkraal data from the Upper Zone of the Bushveld Complex.

Figure 18. MORB normalized trace element concentration plot (modified after Gale et al., 2013) sampled from convergent margins around Scotia (green colour), with (a) the South Shetland Islands (b) South Sandwich Island arc (c) South Sandwich arc basin. The red pattern represents the Bushveld data.

Figure 19. MORB normalized trace element concentration plot (modified after Gale et al., 2013) sampled from Mariana (blue-colour), with (a) Mariana trough (b) Mariana arc (c) Kyushu–Palau Ridge. The red pattern represents the Upper Zone data.

Figure 20. MORB normalised trace element concentration plot (modified after Gale et al., 2013) sampled from the ocean island of Hawaii (yellow colour)- (a) Nihau and (b) Kaula, and the red pattern shows the Bushveld data.

Figure 21. MORB normalised rare earth element concentrations (modified after Gale et al., 2013) sampled from convergent margins in and around Tonga (grey colour), with (a) Tonga Trench (b) Tonga islands (c) Tonga forearc (d) Lau basin (e) Fiji Islands. Note that the red and light brown lines represent two different populations of apatite sampled from the Upper Zone of the Bushveld Complex.

Figure 22. MORB normalised rare earth element concentrations (modified after Gale et al., 2013) sampled from different locations in Scotia (represented by the green colour), with (a) South Shetland Island arc (b) South Sandwich Island arc (c) South Sandwich arc basin (d) East Scotia Ridge. Note that the red and light brown lines represent two different populations of apatite sampled from the Upper Zone of the Bushveld Complex.

Figure 23. rare earth element patterns (modified after Gale et al., 2013) from different convergent margins associated Mariana (blue colour) with (a) Kyushu–Palau Ridge, (b) Mariana trough (c) Mariana arc. The other patterns represent the Bushveld Complex.

Figure 24. MORB normalized rare earth element concentrations (modified after Gale et al., 2013) sampled from the ocean islands of Hawaii (yellow colour), with (a) the Hawaiian islands and (b) the Hawaiian arch. Note that the red and light brown lines represent two different populations of apatite (lower 300 m and upper 325 m, respectively) sampled from the Upper Zone of the Bushveld Complex.

Figure 25 is a volcanic discriminant diagram that compares continental and oceanic geochemical arrays modified after Pearce (1983). Note that the tectonic settings are colour-coded like the previous diagrams; red-Bushveld data, black-Tonga, blue-Mariana, green-Scotia, and yellow-Hawaii.

Figure 26 is a ternary discriminant diagram for various MORB and continental tholeiites, modified after Meschede (1986). Note that the arrow indicates the Bushveld data relative to other locations.

Figure 27 is a Y/Nb versus Zr/Nb diagram, modified after Xia and Li (2019) and Wilson (1989).

Figure 28 is a Y/Nb versus Zr/Nb diagram, modified after Xia and Li (2019) and Wilson (1989) with the Bushveld data represented by the red dots. Note that (a) shows the Bushveld data plotted with Hawaii-yellow, (b) Tonga-black, (c) Scotia-green (d) Mariana-blue.

Figure 29 shows the locations of the most common island arcs, intra-oceanic arcs, and some of the plate boundaries after De Ronde et al. (2003).

Figure 30 is a cross-section through the upper 140 km in a subduction zone process- indicating some of the upper mantle and crustal components after Stern (2002).

Figure 31 (a) and (b) are maps of the Kermadec-Tonga arc system depicting the estimated plate motions after Hawkins (1995) and Turner et al. (1997), respectively.

Figure 32(a) is a regional map of the Izu-Bonin – Mariana arc system (b) shows the tectonic setting of the Mariana arc after Stern et al. (2003).

Figure 33 (a) shows the tectonic setting of the Scotia Ridge (east) within the Atlantic. The boxed Sandwich plate in (a) is located between Antarctica, South America, and the Scotia plate (b) a map showing the East Scotia Ridge and Sandwich plate. This ridge is formed from the east to west divergence of the Sandwich and Scotia plates, after Leat et al. (2000).

Figure 34 shows the islands that makeup Hawaii. The white triangles indicate the summit of different shield volcanoes. The geological features (dike, rift, vent, caldera, and fault) are from Sherrod et al. (2007), after Lautze et al. (2017).

Figure 35 is a map showing the magma genesis for the Hawaiian islands. Again, the most recognized islands have their respective ages indicating the shield-building processes. Note that the ages decrease in the southeast (Lautze et al., 2017).

Figure 36 is a bathymetry map showing the locations of the two samples in Hawaii- Kaula, and Nihau, after Garcia et al. (2016).

LIST OF TABLES

Table 1. Eigenvalues and cumulative frequencies (%) of the 11 principal components	44
Table 2. Eigenvector contributions for all the trace elements in principal components	45
Table 3. The growth stages, approximate age, and rock types, Niihau, and Kaula, after Cousens and Clague (2015)	73

LIST OF ACRONYMS AND SYMBOLS

$\delta^{18}O$	Measure of the ratio of stable oxygen-18 isotopes
BK	Bierkraal farm in the Bushveld Complex
Ga	Billion years
HFSE	High Field Strength Elements
GCDkit	Geochemical toolkit
Ka	Thousand years
LILE	Large Ion Lithophile Element
LG	Lower Group in the Critical Zone of the Bushveld Complex
Ma	Million years
MG	Middle Group in the Critical Zone of the Bushveld Complex
MML	Main Magnetite Layer in the Bushveld Complex
MORB	Mid Oceanic Ridge Basalts
N/A	Not Applicable
NE	Northeast
OIB	Ocean Island Basalt
PCA	Principal Component Analysis
PGE	Platinum Group Element
PM	Pyroxenite Marker Bushveld Complex
REE	Rare Earth Element
RLS	Rustenburg Layered Suite of the Bushveld Complex
SACS	South African Committee for Stratigraphy
SW	Southwest
TTG	Tonalite Trondjemite Granodiorite rocks
UG	Upper Group in the Critical Zone of the Bushveld Complex
UUMZ	Upper Zone and Upper Main Zone of the Bushveld Complex
UZ	Upper Zone of the Bushveld Complex

CHAPTER 1 - INTRODUCTION

South Africa's Bushveld Complex is a huge layered igneous intrusion and is widely known for its rich mineral deposits, including the largest deposits of chromite and platinum in the world, which have significant value for the South African economy and the minerals are used worldwide.

Evaluation and understanding of layered intrusions could provide relevant and crucial information for understanding the dynamism of different magmatic processes, combined with the emplacement of magmas in different tectonic environments (Scoates et al., 2021; Smith and Maier 2021; Chaumba, 2022). In addition, analytical geochemistry assessment of the inferred sources of the magma(s) could help in the study of these processes (Keir-Sage et al., 2021; Chaumba, 2022; Yudovskaya et al., 2022). Accordingly, mineralogical, and petrographic studies are essential for understanding such processes and have been applied globally (Bhattacharjee and Mondal, 2021; Scoates et al., 2021; Smith and Maier 2021; Chaumba, 2022; Lee et al., 2022; Smol'kin and Mokrushin 2022;).

The Bushveld Complex is the most extensive mafic layered intrusion on the planet (Clarke et al., 2009; Yuan et al., 2017; Hasch and Latypov 2021). The complex consists of five limbs/compartments, namely the southeastern, western, far western, eastern, and northern limbs (Yuan et al., 2017; Hasch and Latypov 2021). Cawthorn (2015) and Cawthorn & Walraven (1998) estimated the size of the intrusion area at 65 000 km². The origin and formation of the Bushveld complex have been studied by several researchers (Guilbert, 1962; Ferguson and Botha, 1963; Cameron and Desborough, 1964; Buchanan et al; 1981; Eales and Cawthorn, 1996; Buick et al. 2001; Naldrett et al., 2009; Naldrett et al., 2011), dating its genesis and emplacement to approximately 2.06 Ga. The Bushveld Complex is the location of deposits of platinum group elements (PGEs), vanadium, and chromium that are economically valuable deposits. The formation of the Bushveld Complex involved a diverse variety of magmas with compositions ranging from iron-rich to silica-rich (Fischer et al., 2016). These differences in magma composition can be linked to several geological processes that happened during its development (Fischer et al., 2016). The combined effects of fractional

crystallization, magma mixing, assimilation, and the presence of multiple magma chambers contribute to the wide range of magmas found within the Bushveld Complex (Spandler et al., 2005; Fischer et al., 2016; VanTongeren, 2018; Yao et al., 2021). These geological processes, acting over millions of years, have shaped the complex's intricate and diverse magmatic history (Spandler et al., 2005).

This project focuses on the Upper Zone/ Upper Main Zone (UUMZ), which characterizes the last intrusive phase in the mafic sequence of the Bushveld. The Upper Zone of the Bushveld Complex contains several thick layers of anorthosite and magnetite (Scoon and Mitchell, 2012; Yuan et al., 2017). Geochemical variations persist within the silicate mineralogy of the Upper Zone and form as magma migrates to the final emplacement site (Scoon and Mitchell, 2012; Yuan et al., 2017). Previous research was conducted in the highlighted Bierkraal farm (figure 1) of the western limb of the Bushveld Complex (Yuan et al., 2017). Preliminary results yielded relatively low concentrations of K and Zr (Yuan et al., 2017). The factors contributing to the lower Zr and K concentrations have been influenced by local variations in the magma composition, cooling rates, and subsequent mineral crystallization processes. Other magmas within the Bushveld stratigraphy have different concentrations, but in this study only those of the UUMZ were analysed .

Kruger et al. (1987) studied the Sr isotopic ratios in the UUMZ, suggesting that the parental magma derived from a single source or possibly a single magma chamber. Drill cores from the Bierkraal section of the Bushveld were subsequently analysed by Yuan et al. (2017) with a specific interest in the trace element abundances and signatures. The analysis and investigation by Yuan et al. (2017) of the UUMZ established that the stratigraphic units formed from multiple pulses of plagioclase-laden magma. Cawthorn et al. (1991) regarded these units as products of the crystallisation of the final significant magma injection into the Bushveld magma chamber. Several authors (Cawthorn et al., 1991; Van Tongeren & Mathez, 2013) viewed the UUMZ as a crystallisation product of the last magmatic pulse/injection into the Bushveld magma chamber. Numerous authors have indicated that significant volumes of magma erupted from the Upper Zone resident magma chamber. All these postulations derived from bulk summation models that used the relatively low Zr and K concentrations as principal verifications.

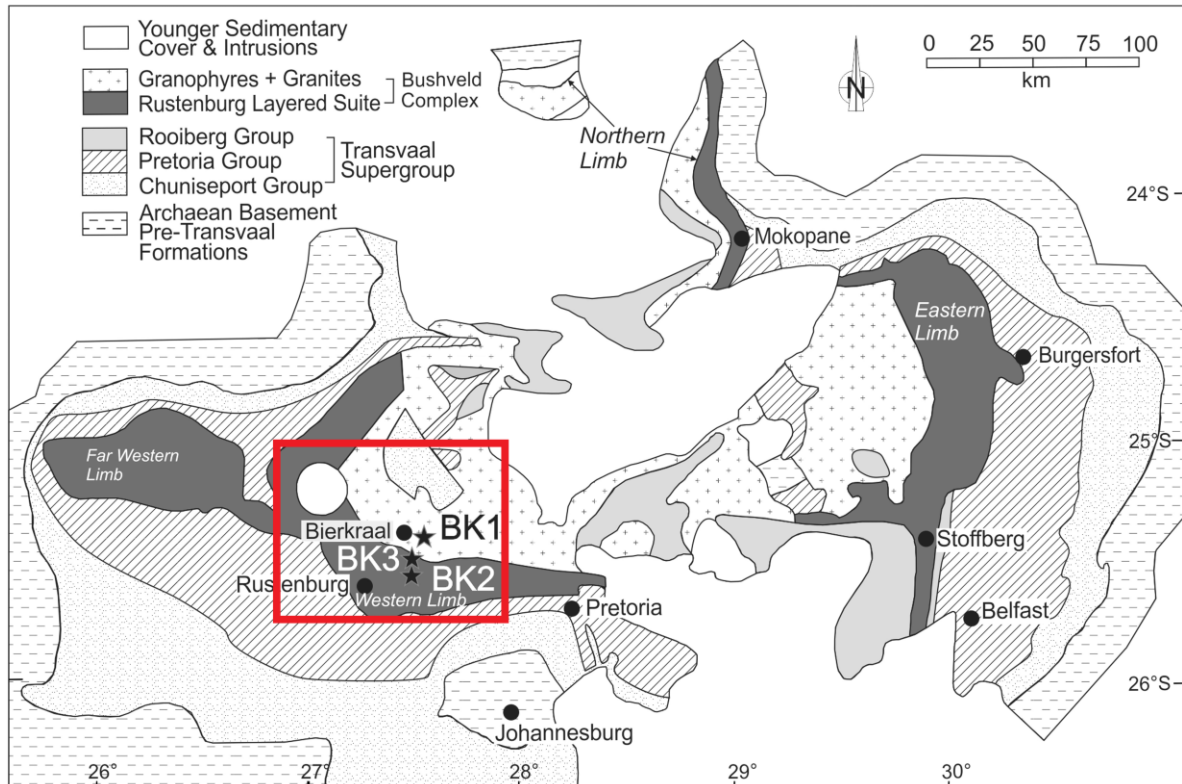


Figure 1. Map of the Bushveld Complex (after Yuan et al., 2017), with the red box indicating the location of the Bierkraal farm (study area).

The western and eastern limbs (Fig. 1) show distinct and unique layers that are not related to magma differentiation processes. Although several authors have identified an extensive usual fractionation trend, with depth, and reversals in the anorthite content of plagioclase, not much research has been conducted on the tectonic emplacement environment of the Bushveld Complex. These reversals in anorthite content accompany the appearance and disappearance of various minerals, such as augite, pyroxene, and plagioclase.

The mantle has a heterogeneous trace element composition and is a primary source of basaltic magma (Le Roux et al., 2002; Hofmann, 2003; Jackson and Dasgupta, 2008; Stracke, 2012). Trace

elements are critical in understanding the geochemical processes that occur within the Earth . These elements can provide vital information about the history and evolution of the mantle (Xia and Li, 2019). Basaltic magma is formed in the mantle through partial melting of mantle rocks (Xia and Li, 2019). For this project, the geochemistry of basaltic rocks is a predictive indicator for determining the likely tectonic setting in which the parental magma originated, as certain tectonic settings impart distinctive and specific geochemical signatures (Xia and Li, 2019; Niu, 2021) . Accordingly, basaltic magmas are considered proportionally reliable for identifying their tectonic origin (Xia and Li, 2019). Note that major elements were not considered in the current study because they are not established indicators of tectonic origin relative to trace elements (Stern, 2002; Niu, 2021). Specific trace element patterns have been proven to be associated with certain magmatic environments, despite ambiguities (Wilson, 1989 ; Wang and Glover, 1992; Pearce and Parkinson, 1993; Xia and Li, 2019; Niu, 2021). Interpreting mafic magmas and their genesis is considered more straightforward than interpreting felsic magmas (Hofmann, 2003; Xia and Li, 2019; Niu, 2021) .

Newly formed magma is subjected to various geochemical and geophysical processes, which force low-density material (magma) to migrate upwards through various zones of weakness. Changing temperature and pressure conditions affect these chemical reactions and alterations, leading to the formation of geochemically distinct magmas. Accordingly, different tectonic environments produce different magmas, which, fundamentally, is what this research study entails (see Fig. 2).

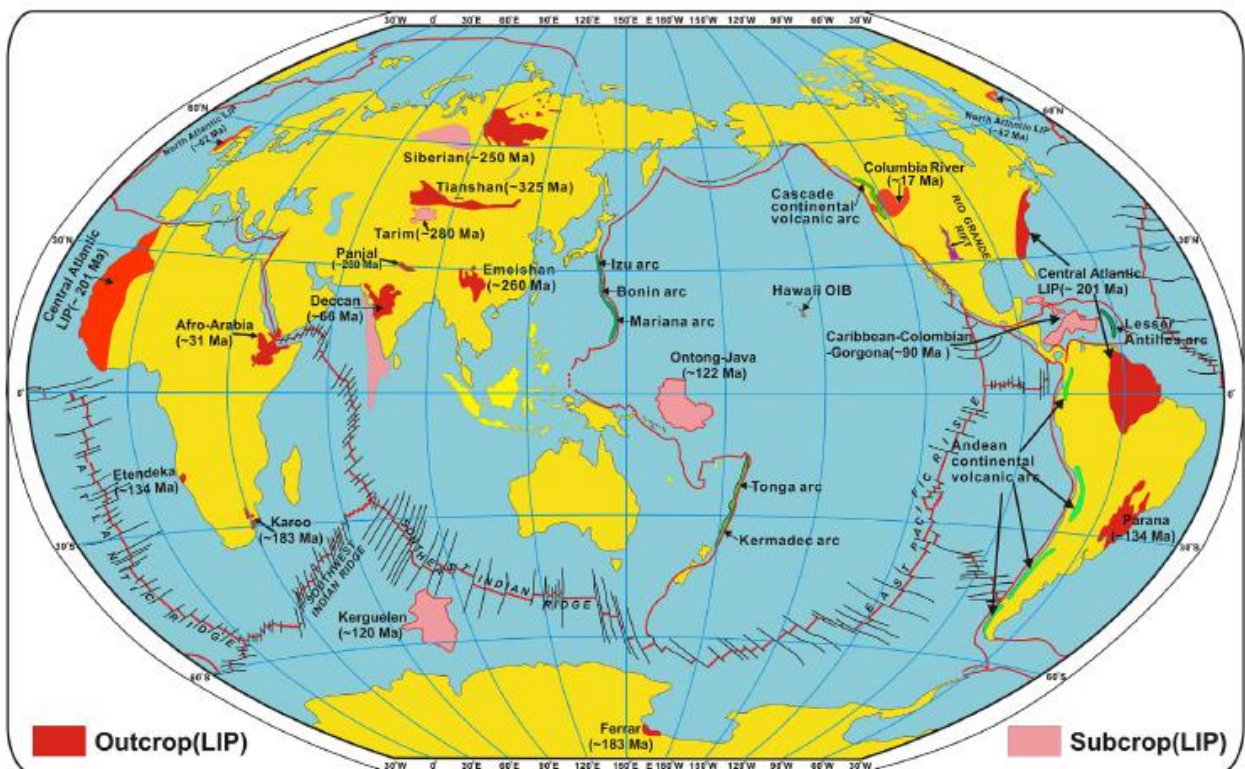


Figure 2. Distribution of mid-ocean ridge basalts, ocean island basalts, arc-related basalts, and large igneous provinces (after Wignall, 2001; Bryan & Ernst, 2008; Xia et al., 2014).

Principal Component Analysis (PCA) of 11 trace elements (i.e. Cr, Co, Ni, Cu, Zn, Rb, Sr, Y, Zr, Nb, Ba) from the Bierkraal area generated the initial results of this study. The PCA technique was used in this study to compare the geochemical signature of the Upper zone of the Bushveld Complex with those of other tectonic regions to restrict the complex's emplacement environment. Only BK1 samples (refer to Fig. 9a for the location) were considered for analyses, as they contain the full array of trace element data. The PCA method relies on the variation within the dataset, and considerable variation was identified in this research. This study aims to identify potential geochemical processes, either through iteration or elimination, from a geological perspective. The scattering of the dataset was interpreted as a by-product of different geological and geochemical processes that derived from different magmatic environments and source regions. Furthermore, separating the data set into distinct groupings could reflect different volumes of melting or source characteristics.

Most research on the Bushveld complex focuses on crystallisation products and how they are formed. However, in this study, borehole data from the Upper Zone of the complex's western compartment are investigated to establish the potential tectonic setting of the Bushveld Complex. Understanding the tectonic environment of this orebody could initiate renewed interest in greenfield and brownfield exploration. Therefore, this investigation includes analysing and comparing the geochemical components of the complex to those of known tectonic settings. In addition, this study could help identify and explain geological anomalies in layered intrusions.

In this study I focused on comparing basaltic data with trace element data from the UUMZ s. The trace element data are supplemented by recent apatite REE data from Magnetite Layer 21 in the Upper Zone of the Bushveld Complex (Van Tongeren & Mathez, 2012). Currently, this is the only REE data available for the Upper Zone of the complex.

Basaltic data sources were considered from different tectonic settings worldwide for the current research project (Fig. 2). A global database (GEOROC), subdivided according to tectonic settings (convergent plate margins, ocean islands, submarine ridges, and oceanic plateaus), was

employed in this research to compare global geochemical trace element signatures against those of the Bushveld Complex. Several literature sources have indicated basaltic magma as having derived from a primitive source, whereas others consider the magma as having derived from a depleted mantle source (Taniuchi et al., 2020).

I applied a multidisciplinary approach to achieve the project objectives, i.e. combining geostatistics and programming. The PCA performed on the trace elements is the result of using computer applications such as GCDkit, R, and ioGAS™ concurrently. Principal Component Analysis (PCA) is a useful statistical technique for analyzing and understanding the tectonic setting of a region based on various geochemical or geological data (Chen et al., 2023). PCA helps identify and extract the most significant patterns and relationships within a dataset by reducing its dimensionality (Chen et al., 2023; Zhang et al., 2023). This technique generates correlated variables and obtains linear functions from the available components (Chen et al., 2023). In exploration, the major advantage of using PCA is distinguishing elemental associations within a correlation or covariance matrix (Chen et al., 2023). In a PCA, each tectonic setting is used to identify the trace elements that impart the most variation to the overall dataset (Chen et al., 2023).

Following Yuan et al. (2017), the working hypothesis for this research project is that the Upper Zone of the Bushveld Complex formed from a single magma chamber, with the melt deriving from a tectonic setting. The methodology included analyses of the trace element properties from Bierkraal borehole data (Yuan et al., 2017) and additional REE data from Van Tongeren & Mathez (2012). Initially, PCA identified the elements that imparted the most significant variation to the dataset. These elements function as indicators and identifiers of specific geological and chemical processes. Therefore, the settings found geochemically dissimilar to those indicated in the Bushveld data (including trace element and REE data) were discarded, whereas those found similar were used in modelling the tectonic setting of the Upper Zone and upper Main Zone (UUMZ).

CHAPTER 2 - GEOLOGICAL SETTING AND BACKGROUND

The Kaapvaal and Zimbabwe cratons in southern Africa are characterised by ultramafic to mafic complexes, including the Bushveld and Molopo (Botswana) complexes. Several mafic intrusions identify with different sections of the Kaapvaal Craton (Wilson and Anhaeusser, 1998) which hosts some of the most economically significant sedimentary basins globally (including the Witwatersrand and Pongola supergroups). Several basins originated in the northern part of the craton (Walraven et al., 1990; Olsson et al., 2010; Walraven and Hattingh, 1993); however, in this research project, the emphasis is on the Transvaal basin, which was intruded by the Bushveld Complex.

The Ancient Gneiss Complex of Swaziland is a chronologically complex and heterogeneous Palaeo-Archaean crustal unit containing a variety of similar looking TTG gneisses that vary in age between ~3640 and ~3200 Ma. The Ancient Gneiss Complex contains the oldest dated zircons in southern Africa ($3702 \pm a$ Ma) according to Eglington and Armstrong (2004). The same author identified the southeastern section of the Kaapvaal Craton as the initial nucleus of the craton, with early development and formation of the gneiss complex between 3550 Ma and 3683 Ma, followed by the formation of the Onverwacht Group (part of the Barberton Supergroup). According to Kröner et al. (1996), the genesis of the Onverwacht Group volcanism dates to ~3.55 Ga (as recorded in the Theespruit Formation). De Ronde and De Wit (1994) interpreted the interlayered sheets and felsic tuffs at the top of the Onverwacht Group as a genetically correlated tonalite–trondhjemite–granodiorite (TTG) pluton at the southern part of the Barberton greenstone belt. This postulation stems from the similarity in age (~3.45 Ga) between the Onverwacht succession and TTG pluton identified towards the south of the greenstone belt. Considering the Sm–Nd data from the southeastern edge of the craton, De Wit et al. (1992) suggested that the proto-craton extended south for a further 200 Ma, implying that the proto-craton, estimated at 3.4 Ga, covered a larger area than initially surmised. According to Eglington and Armstrong (2004), this explanation derives mainly from the age and geology of the younger Moodies and Fig Tree groups, which form part of the Barberton Supergroup. Zircons inherited from volcanic successions within these younger groups could indicate the presence of older crust north of the suture zone. De Wit et al. (1992) inferred this likely suture zone as regionally significant in separating the central Witwatersrand terrain from the southeastern Swaziland terrain.

Development of the Kaapvaal Craton

Figure 3 shows a summary of the events leading to the formation and distribution of the rocks of the Kaapvaal Craton. Figure 4b, c shows two main igneous activities that occurred at 3.3 Ga and 3.25 Ga that are both evident in the Witwatersrand and Swaziland terrains. Most widespread igneous activity before 3.37 Ga occurred around the Barberton Greenstone area, with evidence of volcanism

towards the southeastern, central, western, and northern parts of the craton. The igneous activity in the Barberton area was influenced strongly by the sedimentary Fig Tree and Moodies groups and various granitoid intrusions into the area (Eglington and Armstrong, 2004). Several other regions exerted influence, such as the southern parts (Swaziland), the Witwatersrand terrain (including Halfway House and the Vredefort domes), the Giyani greenstone belt of the Polokwane (formerly Pietersburg) terrain, as well as the central parts of the Limpopo belt. Granitoid belts (mostly TTG) along the eastern edges of the craton have crystallisation ages ranging from 3.37 Ga to 3.14 Ga. These parts of the craton were subject to several granite intrusions (Fig. 4d), including the Mpuluzi Granite, Nelspruit Suite, and Makhutswi Gneiss, just to the north of Barberton.

The Moodies Group represents the final depositional component of the Barberton greenstone belt. This deposition terminated at ~ 3.1 Ga, roughly 400 Ma after the initiation of volcanic activity in the area. During this termination period (3.1 Ga), the central craton area experienced plutonic activity and the deposition of the Dominion Group (Eglington and Armstrong, 2004). Early parts of the Murchison greenstone belt (Polokwane/Pietersburg terrain) and the formation of associated greenstone belts in the region coincide with the period mentioned above. Much of the dated volcanism in the Murchison greenstone belt occurred around 2.95 Ga.

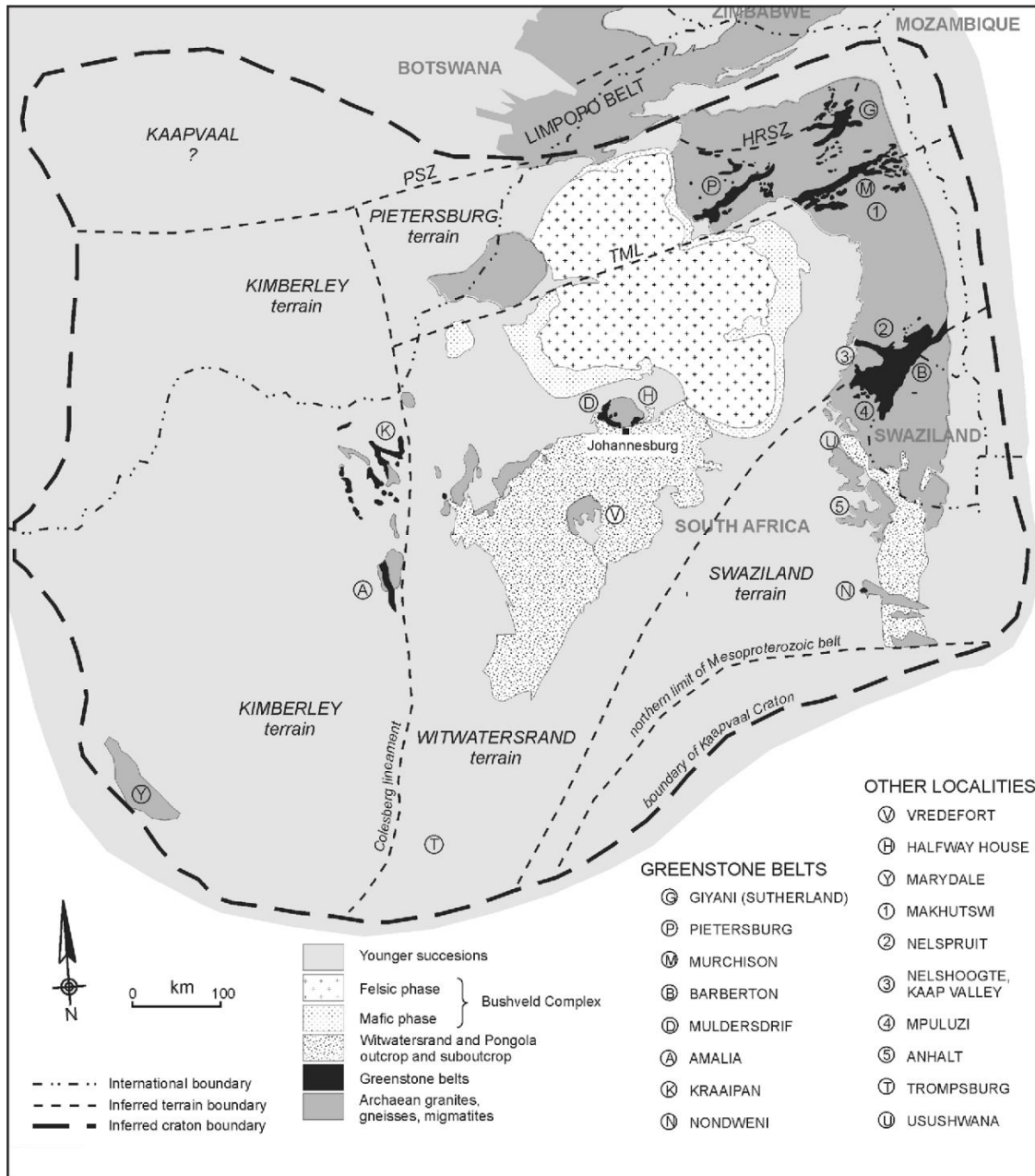
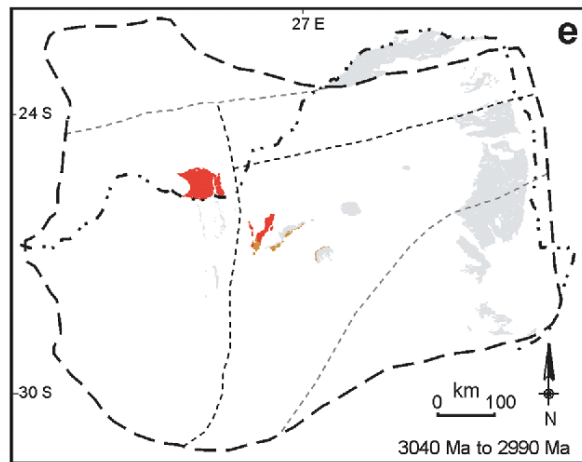
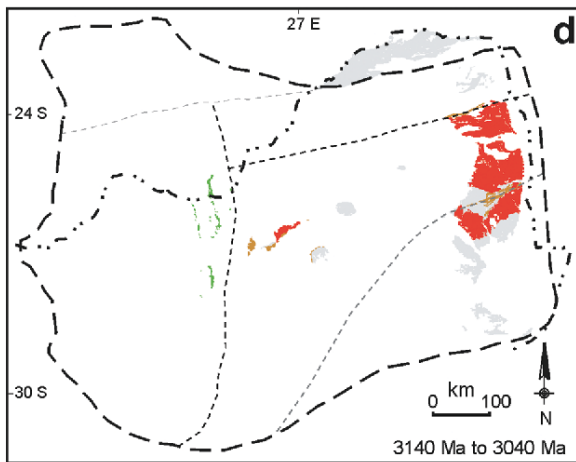
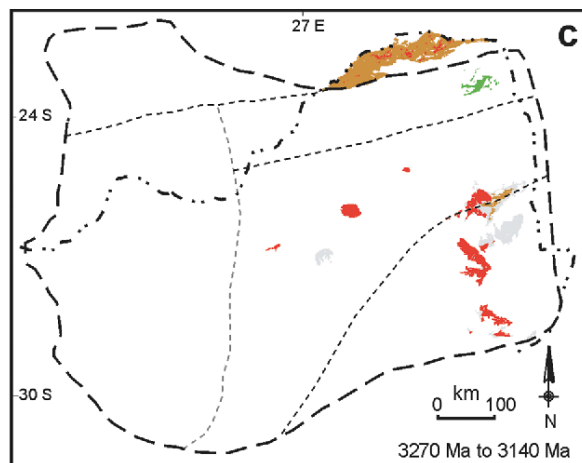
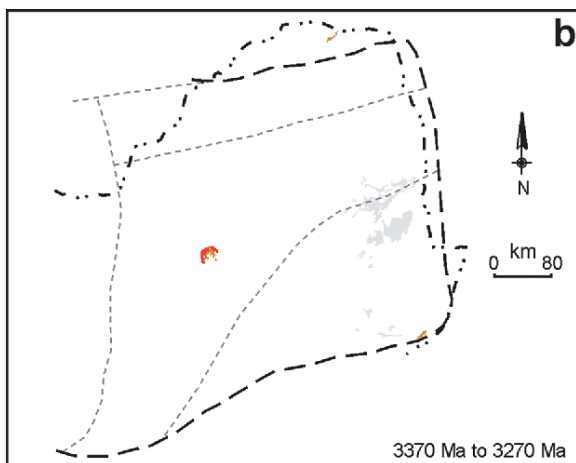
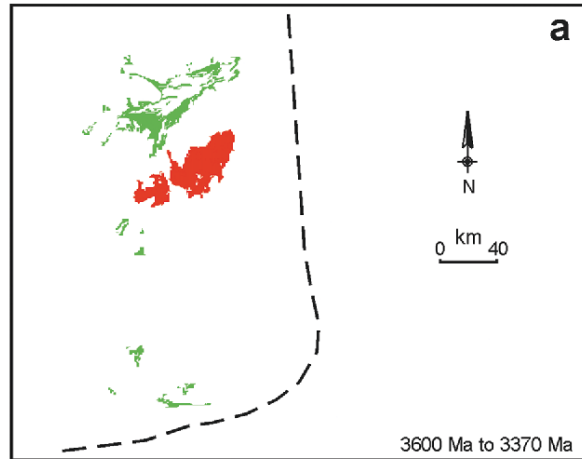


Figure 3. Localities in the Kaapvaal Craton. The thick dashed line represents the geophysical boundary of the craton. The terrain boundaries were inferred and situated to coincide with the units identified by Eglington and Armstrong (2004). These are lineaments (Colesberg and Thabazimbi–Murchison), shear zones (Hout River and Palala) and the Inyoka fault.

Legend

- · — · Inferred craton boundary
 - - - - - Inferred terrain boundary
 - · - · - International boundary
-
- | | | |
|---|---|--|
| <ul style="list-style-type: none"> Intrusive Volcanic / hypabyssal Sedimentary | } | Formed during
the time period
stated |
|---|---|--|
-
- Pre-existing crust



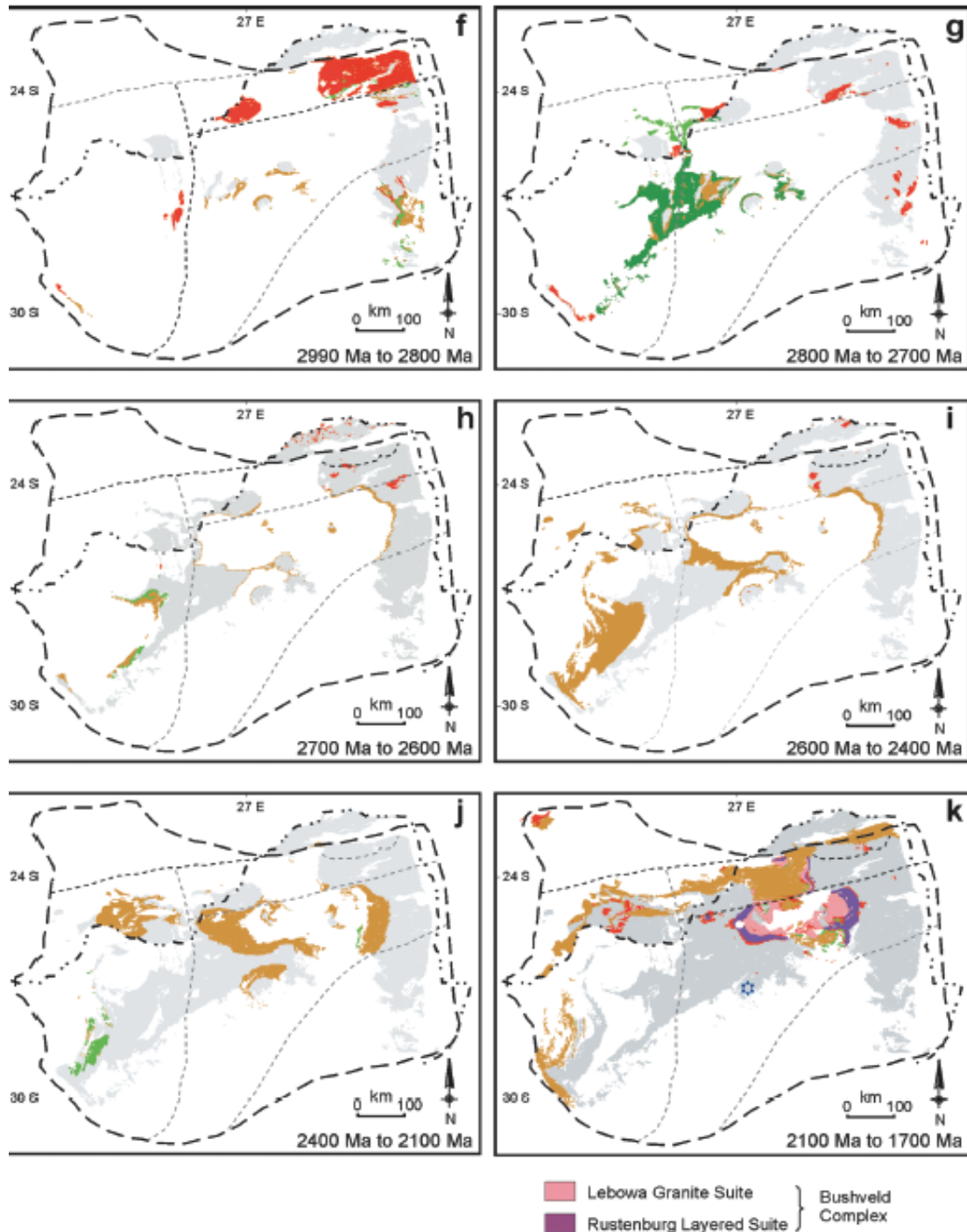


Figure 4. Distribution of volcanic, plutonic, and sedimentary rocks in different periods during the evolution of the Kaapvaal Craton. The Bushveld Complex is shown in panel K, using additional colours because of its significance in this study (modified after Eglington and Armstrong, 2004).

Both sides of the Kimberley–Witwatersrand boundary are intruded by granite (3.04–2.88 Ga), as shown in Figure 3e, f. A magmatic anomaly marks the boundary between them. Schmitz et al. (unpublished) attributed this anomaly to juxtaposing the terrains – Kimberly, Witwatersrand, Swaziland, and Petersburg – now known as Polokwane (in figure 3 above). In contrast, De Wit & Tinker (2004) suggested that the anomaly formed from magnetic lithologies related to thrusting within a shallow crustal depth. Notwithstanding, the Swaziland and Witwatersrand terrains were stable enough for the formation and development of sedimentary basins, with the Witwatersrand Supergroup located centrally and the Pongola Supergroup southeast of the Kaapvaal Craton (Fig. 4f). The Central Rand Group of the Witwatersrand Supergroup contains sedimentation younger than 2.91 Ga (Armstrong et al., 1991). Volcanism was active in the Kaapvaal Craton up to 2.6 Ga, primarily along the western and northern margins (Fig. 4f). By 2.87 Ga, sedimentation in the southeast was complete, coinciding with the intrusion of the Usushwana Complex into the Pongola Supergroup (Eglington and Armstrong, 2004). Figure 4g shows the development and intrusion of the igneous rocks of the Ventersdorp Supergroup (~2.71 Ga) coinciding with the termination of the Central Rand Group deposition (Tinker et al., 2002).

The development of the preserved limits of the craton concluded around 2.75 Ga, possibly through craton–mobile belt interactions (Limpopo and Namaqua–Natal belts) or above the cratonic lithosphere. Tinker et al. (2002) suggested that the craton was more extensive than previously reported or currently preserved. These authors also identified extensive geochronological evidence between 2.75 and 2.65 Ga, indicative of high-grade metamorphism. The proto basins in the Transvaal Supergroup, and the intrusion of granites associated with the Limpopo orogeny developed between 2.65 and 2.5 Ga (Eglington and Armstrong, 2004). Igneous activity associated with the Limpopo Belt continued up to 2.5 Ga with the intrusion of post-tectonic granites (Fig. 4i). Ironstone (Asbestos Hills Subgroup and Penge Formation) and carbonate (Malmani Subgroup) sediments from the Transvaal Supergroup show evidence of magmatic activity from the western and central (Griqualand) areas from 2.6 Ga to 2.4 Ga, as shown in Figure 4i. The deposition of the Transvaal Supergroup concluded owing to the extensive volcanism of the Dullstroom Formation and Rooiberg Group before 2.1 Ga. The intrusion of the granitic rocks was, therefore, coeval with the intrusion of the Bushveld Complex at ~2.06 Ga (Harmer and Armstrong, unpublished data) (Fig. 4k). Most of the Kaapvaal Craton shows extensive metamorphism, with temperatures ≥ 500 °C; however, the southern part of the craton is the only exception. In this study, the development of the Kaapvaal Craton was considered and analysed up to the events that led to the intrusion of the Bushveld Complex.

Stratigraphy of the Kaapvaal Craton

The descriptions that follow derive from the stratigraphic sequences above the Moodies Group (Fig. 5).

Pongola Supergroup

Age of the basement rocks in the Pongola Supergroup is estimated at between 3.6 Ga and 3.0 Ga (Button et al., 1981). The Nsuze and Mozaan groups overlie these basement rocks. The Mozaan Group (Fig. 5) from Weilers (1990) was identified as the last deposition event of the Pongola Supergroup. This group comprises alternating layers of quartz arenite and pelitic rocks, with minor conglomerate and banded iron formations. The Nsuze Group comprises thick layers of volcanic magma (mafic to felsic), minor arkose, quartz, dolomite, and pelitic rocks (Watchorn, 1980; Weilers, 1990). Von Brunn and Hobday (1976) interpreted most of these sedimentary rocks as the reflection of a fluvial deposition environment (possibly shore marine).

Several studies have been conducted on the stratigraphic units in the Pongola Supergroup, ranging from U–Pb zircons to Rb–Sr isochron analyses, for identifying possible age limitations. Hegner et al. (1984) analysed the Sm–Nd errorchron and U–Pb zircons for the Nsuze volcanic rocks and postulated approximate ages of 2934 ± 114 Ma and 2940 ± 22 Ma, respectively. Barton et al. (1983) studied Rb–Sr whole-rock isochron data and constrained the maximum age of the Pongola sediments to 3028 ± 14 Ma (from the underlying Mpuluzi Granite). Most authors interpret the results above as a depositional period spanning 3000–2940 Ma for the Nsuze Group, followed by the Mozaan Group at 2940–2880 Ma (Weilers, 1990). Accordingly, Jahn and Condie (1995) estimated a deposition age of ≤ 150 Ma.

KAAPVAAL CRATON, SOUTHERN AFRICA

Age (Ma)	Formation*	Group	Supergroup	
≈ 1800		Soutpansberg Waterberg		
U				
2200 - 2400	Silverton Strubenkop Timeball Hill	Pretoria	Up	Transvaal
A/P Boundary		Chuniespoort		
2600	Black Reef Selati	Wolkberg	Lo	
U				
2700	Bothavill		Ventersdorp	
2800 - 2850	K8 Booyens	Central Rand	Witwatersrand	
2900 - 2950	Roodepoort Promise Brixton Parktown Orange Grove	West Rand		
3070		Dominion		
<i>Relation Unknown</i>				
2920 - 2940		Mozaan Nsuzi	Pongola	
U				
3300 3400		Moodies Fig Tree	Swaziland	
3450		Onverwacht Scharpenberg		

* Not all formations are listed
 U = major unconformities.

Figure 5. Stratigraphic column/sequence showing rock units in the Kaapvaal Craton, southern Africa (after Condie and Wronkiewicz, 1990).

Witwatersrand Supergroup

The Witwatersrand Supergroup comprises the upper Central Rand Group and lower West Rand Group (Fig. 5). The lower West Rand Group overlies Archaean basement rocks of the Kaapvaal Craton (Jahn and Condie, 1995). Equal proportions of shale and quartzite make up the upper Central Rand Group, with the volcanic rocks in the Jeppestown Subgroup. Tankard et al. (1982) identified a basal shallow-marine environment as a potential palaeoenvironment for the deposition of the West

Rand Group. The Central Rand Group comprises a mixture of quartzite, sub-greywacke, conglomerate, and shale (Pretorius, 1976). The overlying Ventersdorp and Dominion subgroups were instrumental in identifying and constraining the depositional age of the Witwatersrand sediments (John and Condie, 1995). Armstrong et al. (1991) calculated an age of 3074 ± 6 Ma using U–Pb zircons obtained through ion microprobe analysis.

Similarly, Armstrong et al. (1991) obtained zircon ages for the lower and middle Ventersdorp Supergroup and Klipriviersberg Group lavas (ca 2718 ± 8 Ma and 2699 ± 16 Ma, respectively). Accordingly, the deposition of the Witwatersrand sediments lasted for 350 Ma, between 3070 and 2720 Ma (John and Condie, 1995). Most zircons sampled in the Witwatersrand basin yield U–Pb ages no younger than 3000–2900 Ma. Robb et al. (1989) used these ages as evidence against pre-existing granites during the deposition of the West Rand Group.

Ventersdorp and Transvaal supergroups

The Ventersdorp Supergroup mainly comprises a succession of volcanic rocks (basalt, komatiite, rhyodacite, and minor chemical and clastic sediments). Downward coarsening units of carbonate, pelite, quartzite, and conglomerate characterise the Bothaville Formation (Button, 1981). These sediments were deposited in an alluvial plain type setting and, potentially, in a rift valley setting (Tankard et al., 1982).

On the other hand, three groups characterise and form the Transvaal Supergroup. From top to bottom, these groups include (1) the upper Pretoria Group, which consists of marine tidal pelite and quartzite, and relatively small amounts of volcanic and carbonate rocks. The Silverton, Strubenkop and Timeball Hill formations are dominated by quartzite and pelite. The sediments in these formations derive from north/northeast sedimentation, controlled by uplifting around the Limpopo region (Tankard et al., 1982). (2) The Chuniespoort Group has mainly carbonate rocks (including dolomite) and minor clastic rocks. (3) The lower Wolkberg Group (Black Reef and Selati formations) comprises shallow-marine to fluvial siltstone, feldspar to sub-greywacke, siltstone, arkose, conglomerate, pelite

and basaltic flows. The entire sequence in the Transvaal Supergroup evolved from localised rifting to a massive cratonic basin, followed by Pretoria Group deposition in a reactivated rift basin (Eriksson & Clendenin, 1990).

Precise zircon ages constrain the deposition age for the Ventersdorp Supergroup to 2718 ± 8 Ma for the lower Ventersdorp lavas and 2699 ± 16 Ma for the middle Ventersdorp group (Armstrong et al., 1991). These authors suggested that the carbonate Pb–Pb (2557 ± 49 Ma) for limestones in the Boetsap area (Part of a village situated in the Northern Cape) represents late diagenesis. Accordingly, the Bothaville, Selati, and Black reef formations were deposited between 2600 and 2700 Ma (John and Condie, 1995), implying that the Pretoria Group is younger than 2550 Ma. Hamilton (1977) estimated the granites postdating the Transvaal Supergroup at $\sim 2095 \pm 24$ Ma based on Rb–Sr data. According to John and Condie (1995), a lengthy hiatus between the Pretoria and Chuniespoort groups marks the Archaean–Proterozoic boundary. These authors suggested that the deposition of the Pretoria Group occurred ≥ 2400 Ma.

Waterberg and Soutpansberg groups

Tankard et al. (1982) suggested that the Soutpansberg and Waterberg groups are at equal stratigraphic levels. The Waterberg Group comprises $\sim 80\%$ sandstone and $\leq 10\%$ fine-grained pelite, and conglomerate. Jansen (1970) identified volcanoclastic sedimentary rocks and trachytic volcanic rocks around the southern sections of the Transvaal basin. Immature and mature sandstones dominate the lithologies in both these supergroups. Immature red sandstones are a variation of these sandstones and are described as some of the oldest preserved red beds on Earth (Truswell, 1990). The mature sandstone shows no red pigmentation. The deposition environment is similar to a fluvial environment within a continental rift setting (John and Condie, 1995). The Soutpansberg Group comprises subaerial basaltic flows and sandstones, conglomerate, and arkose, possibly deposited in a braided stream within a continental environment (Jansen, 1970). The deposition of both the Soutpansberg and Waterberg groups postdates the intrusion of the Bushveld granites (1913 ± 30 Ma), although an alkaline complex intruded the sedimentary succession (Jahn and Condie, 1995). Accordingly, the deposition of both these groups occurred between 1850 and 1750 Ma.

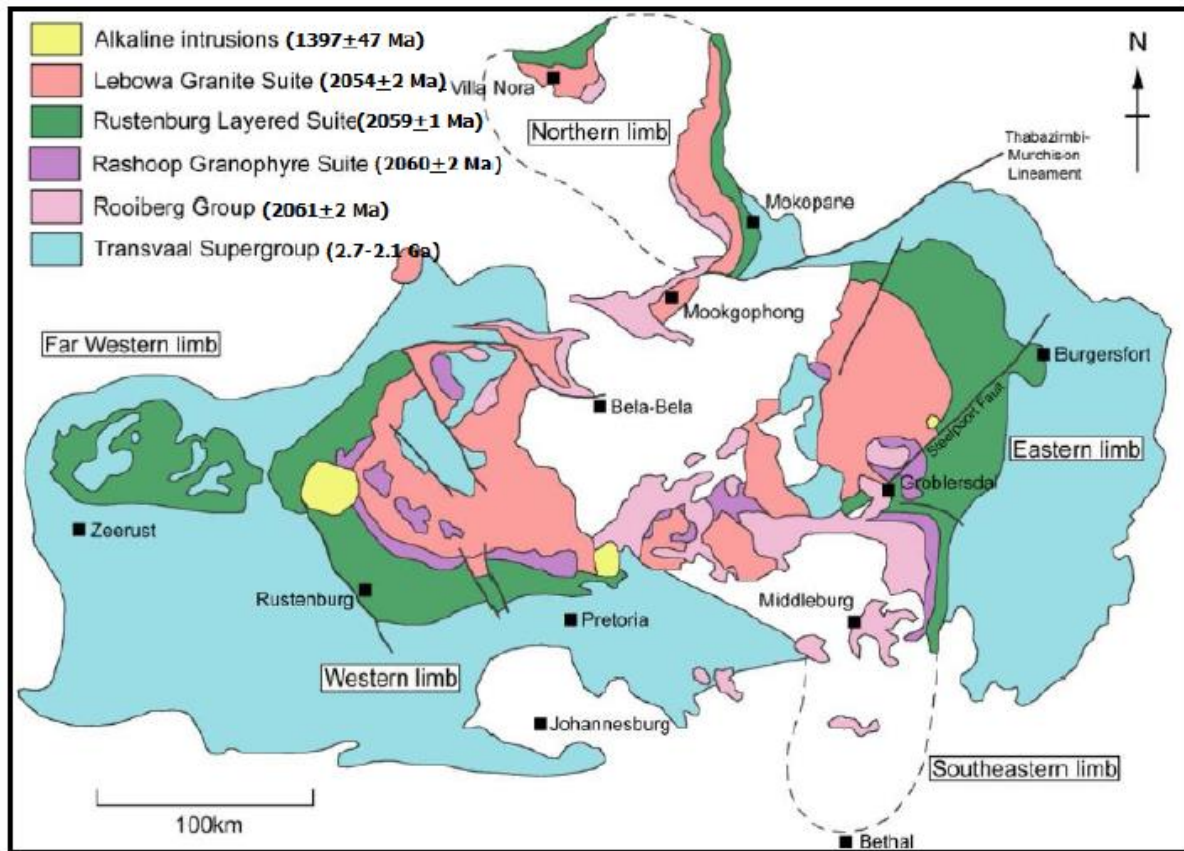


Figure 6. Simplified map of the Bushveld Complex, with the different stratigraphic units coded. The legend shows the ages of the lithologies (after Bamisaiye, 2015, PhD thesis).

The Bushveld Complex

The Bushveld Complex (Fig. 6) is a massive, layered intrusion emplaced into the 'stable' Kaapvaal Craton or relatively stable cratonic environment (Cawthorn & Walraven, 1998). This complex comprises several intrusions of varying ages, chemistry, and morphology. Hatton (1995) identified the complex as an intrusive event equivalent to a flood basalt and attributed its genesis to mantle plumes. The emplacement of the complex occurred through magmas that intruded the chemical and clastic sedimentary rocks of the Pretoria Group (Cawthorn & Walraven, 1998). The injections of magma

occurred over a relatively short period. Buick et al. (2001) calculated an emplacement age of under 1 Ma, using U–Pb titanite ages. Skursch et al. (2022) reported Zircon U–Pb chronology and Hf isotopes ages of 2054.3 ± 0.7 to 2056.5 ± 0.9 Ma. Following emplacement, the denseness of the Bushveld Complex caused sagging of the central portion of the complex. Webb et al. (2011) calculated a gentle dip angle (between 15° and 20°) for the complex, with the strata generally dipping centrally, which activated several N–S-trending faults within this igneous complex.

The mafic/ultramafic rocks of the Bushveld Complex lie between the clastic rocks of the Pretoria Group and the overlying felsic roof rocks of the Rooiberg Group (Tegner et al., 2006). Tegner et al. (2006) identified four other intrusions into the Bushveld Complex, namely the Rooiberg Group, Rustenburg Layered Suite (RLS), Rашoop Granophyric Suite and the Lebowa Granite Suite. Lenhardt & Eriksson (2012) analysed the Rb–Sr content and calculated a relatively young age for the intrusions. The Rooiberg Group is considered older than the other intrusions and forms part of the roof rocks to the RLS, which was emplaced before the Lebowa Granite Suite. The Rашoop Granophyric Suite intruded at the contact between the RLS and the Lebowa Granite Suite. Discrete limbs define the RLS. Eales & Cawthorn (1996) suggested that the western and eastern limbs connect at depth, and the postulation of these authors forms part of the argument in the current study.

Formation and intrusion of the Bushveld Complex

The complexity of the relationship between the different intrusions in the Bushveld Complex and a lack of outcrops in other domains are partly reasons for disagreement between several authors over the formation of the complex. A prevalent argument or suggestion for the formation of the complex is that a high volume of magma would be required to form a layered intrusion of this magnitude and that it would have had to erupt over a short period.

Hatton (1998) proposed a model often referred to in the current study. This model attributed the formation of the Bushveld Complex to the melting of sedimentary and detrital material within a subducting plate boundary near the margin of the Kaapvaal Craton. Alternatively, a prior model, developed by Hatton & Schweitzer (1995), which has since gained popularity in geology circles, proposed the intrusion of a magmatic plume beneath the Kaapvaal Craton. Another model (Cawthorn and Walraven, 1998) suggested that the Bushveld Complex developed through the accretion of several magma influxes, with the initial magma having an ultramafic composition and later intrusions categorised as normal tholeiite (Von Gruenewaldt, 1979).

A collection of the $^{87}\text{Sr}/^{86}\text{Sr}$ isotopic ratios in the Bushveld Complex stratigraphy shows that the magma chamber potentially formed in two major stages (Kruger, 2005). The initial open-system stage of integration (including the lower central zone, Critical Zone, and Lower Zone) shows multiple influxes of silicate melts with contrasting isotopic compositions (Cawthorn & Walraven, 1998). The formation of these magmas included various processes, such as spontaneous mixing and fractionation, which influenced the deposition of cumulate minerals. Sustained shifts in isotopic ratios, development, formation of unconformities, and significant changes in major mineral compositions characterise the boundaries between these zones. According to Kruger (2005), the boundaries correspond to more significant influxes of magma.

According to Kruger (2005), the Lower Zone and lower Critical Zone are in a belt that stretches from the northeastern part of the complex (which includes Burgersfort and Steelpoort on the eastern limb) to the western part (Rustenburg). Figure 7 shows some sections of the igneous complex, including thick layers of pyroxenite and harzburgite, as well as the chromitite layers of the lower Critical Zone. Stratigraphically exclusive and vastly abrupt increases in Sr isotopic ratios imply contamination of the magma chamber by less-dense felsic liquid (which forms part of the roof). The contamination led to the precipitation of the chromitite layers (Cawthorn & Walraven, 1998). This postulation suggested that each chromitite layer represents an area of expansion, erosion, and deformation of the magma chamber. Further, these layers formed from in situ contamination by the felsic roof rocks of the Rooiberg Group, which intruded the noritic and orthopyroxene-bearing liquids of the Critical Zone (Cawthorn & Walraven, 1998).

The new melt initially intruded the northern limb to the north of the Thabazimbi Murchison Lineament (TML), contaminated the floor rocks, mixed with sulphur, and eventually precipitated the Platreef, according to Cawthorn & Walraven (1998). The new magma precipitated the Platreef along the floor rocks before flowing southwards towards the magma chamber. As a result, the high influx of magma eroded an unconformity along the Critical Zone (Fig. 7), which triggered the formation of the Main Zone (Cawthorn & Walraven, 1998). The Main Zone in the magma chamber includes the Merensky Reef, which precipitated along the unconformity. Furthermore, Upper Zone magma intruded the magma chamber from the southern lobe (Bethal) and the TML (Cawthorn & Walraven,

1998). This erosion is the reason for a 'gap' in parts of the western limb of the complex (Cawthorn & Walraven, 1998). The base of the magma influx coincides with the Pyroxenite Marker (PM) in the northern lobe and forms part of the stratigraphic and petrological base of the Upper Zone. The pattern of the outcrops and the harmony between isotopic and geochemical units indicate that the Bushveld Complex was a shallow and wide sill-like sheet with lobate features upon the onset of crystallisation. The mineral deposits and rock strata are continuous over the entire intrusion (Cawthorn & Walraven, 1998).

The occurrence of diapir domes, minor transgressions of the mafic intrusion, and the chilled zones along the host rocks (Uken, 1998) influenced the floor rocks of the RLS (Fig. 6). Localised extensions across reactivated significant lineaments, such as the Thabazimbi Murchison Lineament, with a northeast–southwest inclination (McCourt, 1995), Steelpoort fault (Cawthorn et al., 2002) and, according to Hartzler (1989), the Crocodile River fault. Bumby et al. (1998) identified the first and second deformation events in this area as by-products of the Bushveld intrusions. These intrusions produced faulting and folding along a southwest–northeast principal stress direction, with the intrusion of the Bushveld Complex occurring along with a similar trend to the second deformation. A third deformation event (D3) occurred after the Bushveld intrusion (post-Bushveld).

Rustenburg Layered Suite

The terms Rustenburg Layered Suite (RLS) and the Bushveld Complex are mostly used interchangeably in the literature. The RLS contains large parts of the Bushveld Complex and was formed from multiple pulses of mafic to ultramafic magma (Eales & Cawthorn, 1996). This layered suite, part of the Bushveld Complex in the northern part of South Africa, is the last significant intrusion into the complex. Van der Merwe (1976) calculated the thickness of the RLS as ~7 750 m in the western limb, 7 000 m in the northern limb, and 9 000 m in the eastern limb. The suite covers an area of ~65 000 km² and consists of ultramafic layers that serve as hosts to some of the largest PGE reserves on Earth. Chromite is associated with the Platinum Group Elements (PGEs) prevalently sampled and manufactured from the RLS. Eales & Cawthorn (1996) suggested that the injection of multiple pulses of magma (with varying compositions) into a crystallising pile/mush of residual magma resulted in alternating zones of incompatible chemistries. Accordingly, the RLS is separated into individual zones to distinguish these geochemically significant zones, which are classified based on lithological and mineralogical variations.

The RLS zones are (top to bottom) Upper Zone (study area), Main Zone, Critical Zone, and Lower Zone (Fig. 7). The Lower Zone comprises orthopyroxene -rich mafic to ultramafic layers, with overlying Critical Zone rocks (Robb and Mungall, 2020). The appearance of chromite differentiates the Critical Zone from the surrounding zones. The Critical Zone is further subdivided into the (1) upper Critical Zone (consisting of norite and anorthosite), and (2) lower Critical Zone (completely ultramafic). The lower Critical Zone and the Lower Zone occur individually within sections of the Bushveld Complex, whereas the upper Critical Zone is visible throughout the perimeter of the RLS (Scoon and Teigler, 1994). The thick and laterally elongated Main and Upper zones overlie the Critical Zone. The lower Critical Zone and Upper Zone chromitite seams vary in occurrence across horizontal discontinuities. They are labelled by differentiating the Upper Group (UG), Middle Group (MG), and Lower Group (LG) seams (Cousins et al., 1964; Scoon and Teigler, 1994).

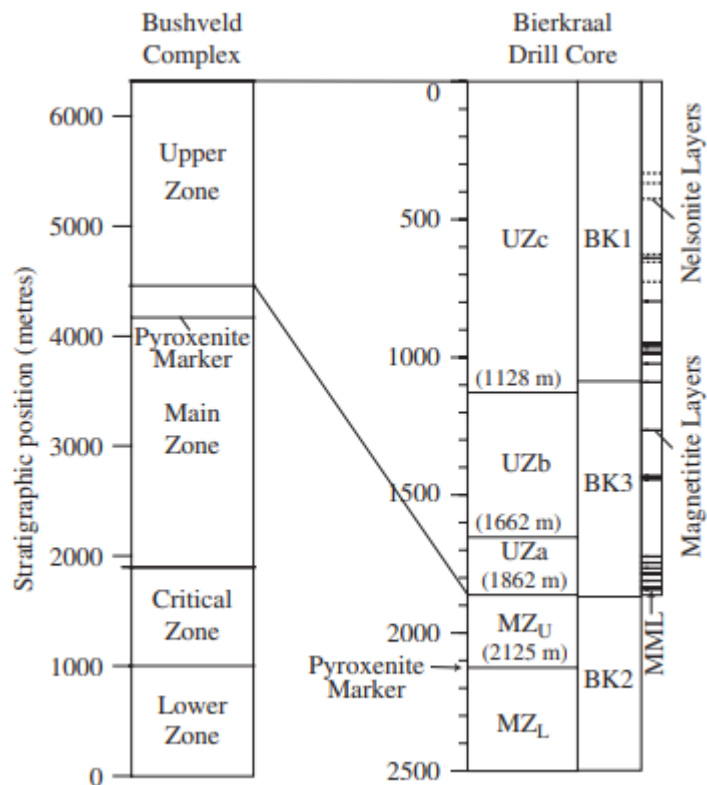


Figure 7. Section through the Rustenburg Layered Suite on the left, agglomerated with the Bierkraal drill cores from the Upper and Main zones on the right (after Tegner et al., 2006).

Upper Zone

This zone is ~2 100 m thick and, according to Kruger et al. (1987), represents the terminal stages of crystallisation of the RLS. The same author identified this zone as a product of magma injection into the PM. Moreover, this final crystallisation stage forms the most differentiated and felsic magmatic compositions throughout the RLS. In terms of rock units, this zone primarily consists of ferro-gabbro and diorite, with highly differentiated mineralogy (Fig. 8).

The South African Committee for Stratigraphy (SACS) identified the lower boundary of the Upper Zone as the point above the PM where cumulus magnetite first occurs. This zone contains several layers of anorthosite and magnetite (Von Gruenewaldt, 1973; Kruger et al., 1987). The minerals identified in the Upper Zone include olivine, plagioclase, clinopyroxene, orthopyroxene, apatite, and magnetite. Highly evolved compositions such as apatite are located towards the top of the Upper Zone, indicating prolonged differentiation of a more evolved melt (Eales & Cawthorn, 1996).

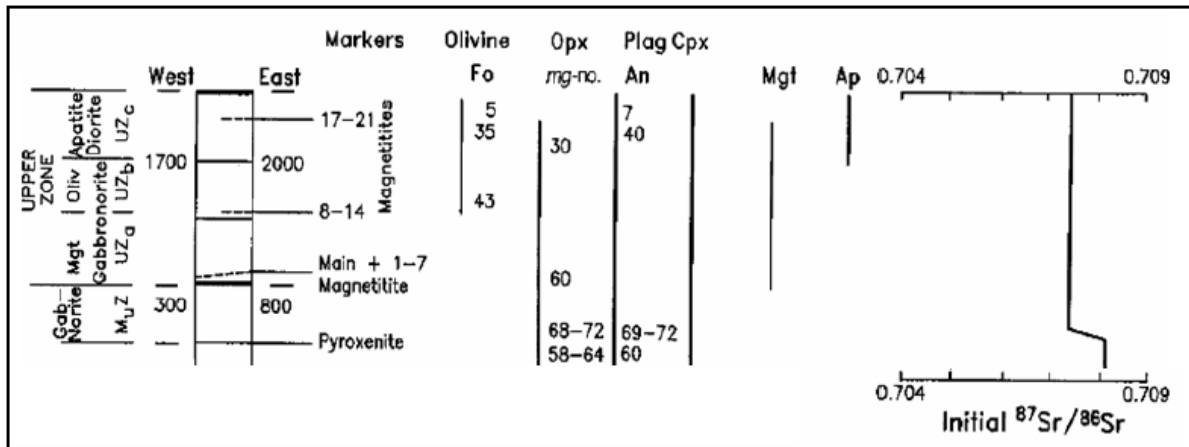


Figure 8. Simplified stratigraphic column of the Upper Zone and upper Main Zone (UUMZ). The locations of the Pyroxenite Marker (PM), magnetite layers, mineral variations, and the relatively constant Sr isotopic ratios are indicated (Cawthorn & Walraven, 1998).

Focusing on the Sr/Sr isotopic ratios, Kruger et al. (1987) proposed that a single homogenous magma formed the Upper Zone (Fig. 8). These ratios are constant for most of the Upper Zone and estimated at 0.70731. Kruger et al. (1987) indicated the PM as the lower boundary of the Upper Zone and considered differentiation and crystallisation as the driving forces for its formation, followed by observation of the mineral progression throughout the Upper Zone. Wager & Brown (1967) first suggested three subdivisions of the Upper Zone (Fig. 8), focusing on the appearance of cumulus minerals unique to specific depths. The subdivision of the Upper Zone comprises UZa, UZb, and UZc, with UZa showing the first appearance of magnetite (cumulus), UZb showing the first appearance of olivine, and UZc the first appearance of cumulus apatite. The Upper Zone shows geochemical reversals in the mineralogy and significant compositional changes. Tegner et al. (2006) used minerals such as anorthite and olivine (Mg#) to analyse geochemical changes in the Upper Zone and identified several cycles of magmatic replenishment.

Western Bushveld Complex (study area)

The western Bushveld Complex is divided into two main divisions, namely the general western Bushveld that dips towards the centre of the intrusion at low angles, and the far western Bushveld Complex. According to Coertze (1970), minerals including pyroxene form the far western compartment, with minor additions of lower Critical Zone chromitite. Felsic rocks constitute most of the Pilanesberg Complex, which has a circular structure and is situated in the central part of the Bushveld Complex (Cawthorn & Walraven, 1998). Rocks of the Main Zone are prominent in this area, with minor parts from the Upper Zone. This compartment also hosts laterally extensive and well-developed Critical Zone rocks.

Measurements conducted by Bumby et al. (1998) indicated that this compartment trends NNW. These authors also identified three significant faults in the section, namely the Brits, Rustenburg and Welgevonden faults. Field evidence from Coertze (1970) suggested that the Pretoria Group (including the Magaliesburg Formation quartzite) underlies the RLS; therefore, some xenoliths in the RLS rocks derive from the Pretoria Group quartzite. The RLS volcanism transported some Magaliesburg quartzite xenoliths to most areas across the western Bushveld and towards the SW of Pilanesberg complex (Coertze, 1970). Supporting this argument, Eriksson et al. (1995) described the cross-cutting relationship between Pretoria Group sediments (quartzite) and RLS volcanism. Eriksson et al. (1995) attributed the localised quartzite xenoliths to a process of contact metamorphism, which subsequently formed silica hornfels. Bristow et al. (1993) identified anorthosite xenoliths as evidence for the interaction of RLS magma with rocks from the Critical Zone. Such interaction suggests direct crystallisation from the residual magma chamber (Eales & Cawthorn, 1996). In addition, localised folding of floor rocks occurred, which Von Gruenewaldt and Hutton (1987) suggested formed from ductile deformation caused by the emplacement of the Bushveld Complex.

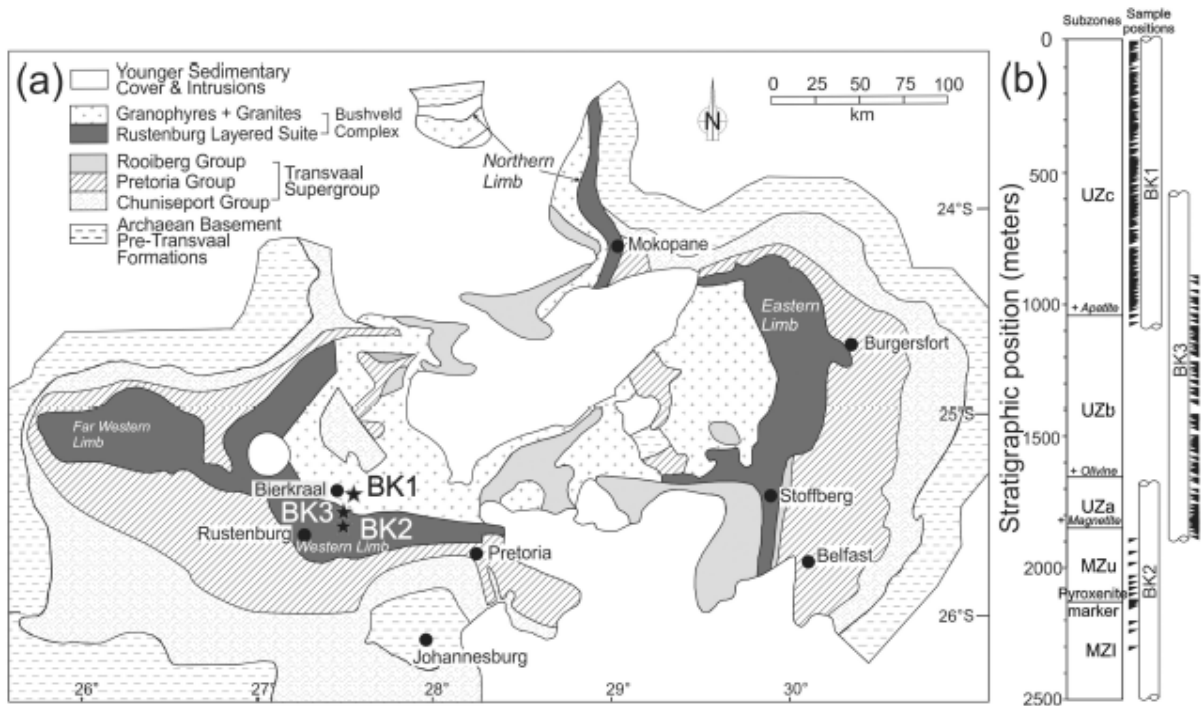


Figure 9. (a) Simplified map of the Bushveld Complex, with the red area indicating the locations of BK3, BK1, and BK3. (b) Stratigraphic column through the Upper Zone of the Bushveld Complex, with the appearance of apatite in UZc, olivine in UZb and titanium-bearing magnetite in UZc (Yuan et al., 2017), categorising the different subzones.

Background to Bierkraal data

Information about the Upper Zone of the RLS derives from analyses of drill cores from the western limb, close to Rustenburg (Fig. 9a). The Geological Survey of South Africa (now the Council for Geoscience) initially explored the area (highlighted in Fig. 7) in the 1970s by drilling three boreholes. These boreholes provided an entire stratigraphic column of the Upper Zone and parts of the Main Zone (Walraven & Wolmarans, 1979). These boreholes are BK1, BK2, and BK3 on the farm Bierkraal, where drilling started. Numerous studies inferred the connection between the boreholes using the first appearance of cumulus apatite, similarly in the eastern part of the complex, and the V_2O_5 content.

The correlation of the boreholes to depth is shown in Figure 10. Previous work on the boreholes was done by Cawthorn & McCarthy (1985), Merkle & von Gruenewaldt (1986), Kruger et al. (1987), and Tegner et al. (2006), to name a few.

The first borehole (BK1) ranges from the Lebowa Granite Suite to depths of ~1 600 m, intersecting a thick magnetite layer. The second borehole (BK2) starts from the main magnetite layer (MML) through the Main Zone to the PM in the upper Main Zone. The third borehole (BK3) was drilled to supplement and help understand the gap (Fig. 8b) between the bottom of BK1 and the top of BK2 (Britt, 2015, MSc).

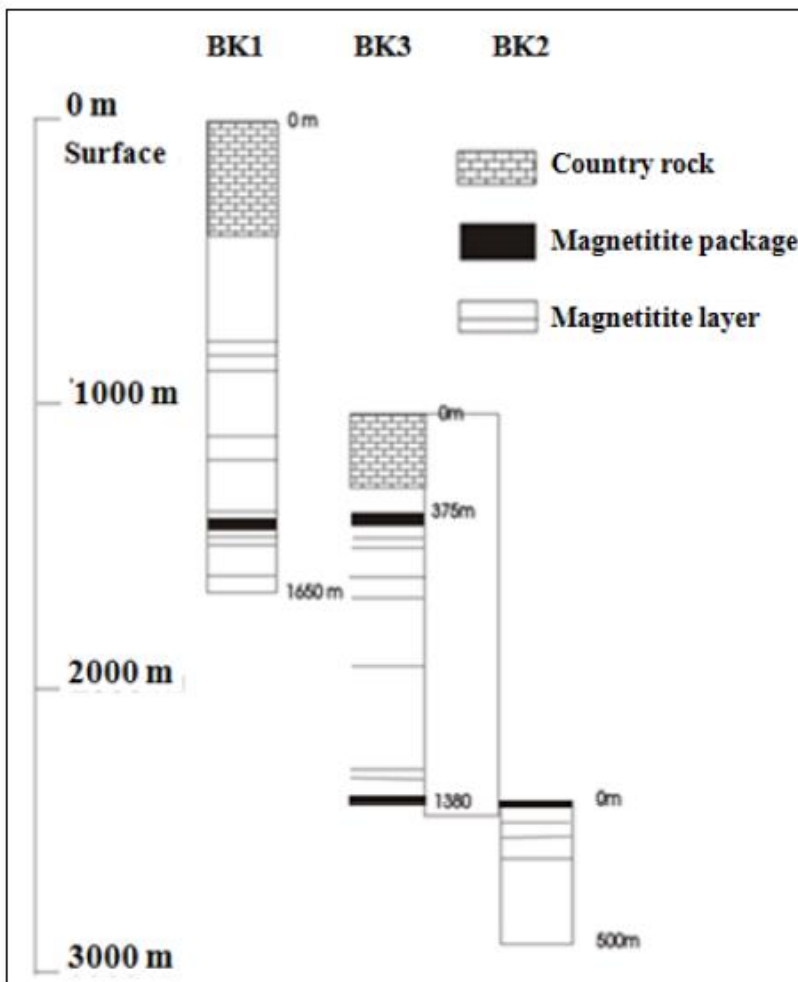


Figure 10. Sketch of the correlation between the three boreholes (BK1, BK2, and BK3) (after Britt, 2015).

Eastern Bushveld (complementary REE data)

The RLS was intruded along a regional unconformity, which separates the underlying Pretoria Group sediments from the residual rocks (Zintwana et al., 2012) and the Rooiberg felsic rocks (Cheney & Twist, 1991). The lithologies and outcrops are more exposed in the eastern limb of the Bushveld Complex as regards the nature of the topography (Sharp, 1981). These rock layers dip at $\sim 60^\circ$ near the contact area and flatten towards the centre; therefore, the mining activities in this area focus primarily on the low-dipping strata. The Main Zone in this unit contains norite, gabbro, pyroxenite, and anorthosite, with a thickness between 0 and 3 000 m (Kinnaird, 2005).

Magnetite bands and gabbros are evident in the Upper Zone. Molyneux (1974) identified 25 magnetite layers on the eastern limb of the complex, with the vanadium concentration in the magnetite layers being economically significant. The Lower Zone divides into an upper pyroxenite subzone and a lower harzburgite and pyroxenite subzone. The orientation and structure of the floor rocks in the Lower Zone influence the overall thickness approximated at 1 584 m. Cawthorn et al. (2006) analysed the Main Zone and identified minor pyroxenite and norite occurring in direct contact with the Transvaal Supergroup. Uken (1998) suggested that the RLS in this limb has been intruded by floor rocks formed from diapiric processes.

CHAPTER 3 - METHODOLOGY

Data description

The foundation of this study is a basaltic database constructed from different tectonic settings by employing GEOROC, an online database/depository for storing different types of geochemical data. For this research project, the tectonic settings identified are convergent plate margins, ocean islands, submarine ridges, and oceanic plateaus. The data were collected exclusively on basaltic rock samples using the URL: Georoc.mph-mainz.gwdg.de/Georoc/Entry.html. Furthermore, GEOROC data with standard basaltic tectonic settings were incorporated into data from the UUMZ (Yuan et al., 2017). The interquartile range statistical approach was used for cleaning and filtering data and discarding any outliers. The upper and lower boundaries for individual elements within different locations were established in this manner. Overall, ~350 samples were available for this research project.

Seven different sample locations were identified based on Britt (2015; MSc thesis, Fig. 11) and the above-mentioned tectonic settings, including the Hawaiian Islands, Manihiki Plateau, Mariana, Scotia, and Tonga arcs, and UUMZ drill hole data from the Bierkraal farm.

Bierkraal boreholes

Drill-core data from the northeast portion of the Rustenburg Layered Suite (RLS) are interpreted as the Upper Zone of the RLS in the western limb of the complex. Three boreholes drilled by the former Geological Survey of South Africa (now the Council for Geoscience) were considered in this study (Yuan et al., 2017). According to Walraven & Wolmarans (1979), the three boreholes were part of an initiative aimed at establishing and identifying the overall stratigraphy of the Upper Zone. These boreholes, named BK1, BK2, and BK3, were drilled on a farm called Bierkraal just NE of Rustenburg (Fig. 11) (Yuan et al., 2017). In Chapter 2, the correlation between the boreholes is discussed.

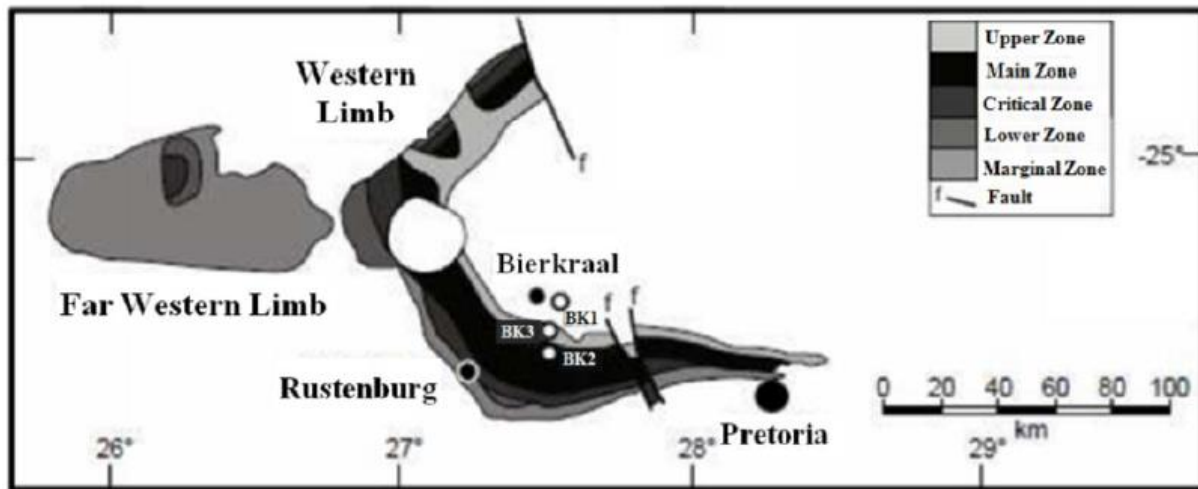


Figure 11. Map of the western and far western limbs of the Upper Zone of the RLS close to Rustenburg. The locations of boreholes BK2, BK2, and BK3 (Britt, 2015; MSc) are indicated.

Sampling

Yuan et al. (2017) collected ~260 samples from the Bierkraal drill cores, with a focus on the UUMZ stratigraphy. The average distance between the samples is ~10 m (Fig. 12).

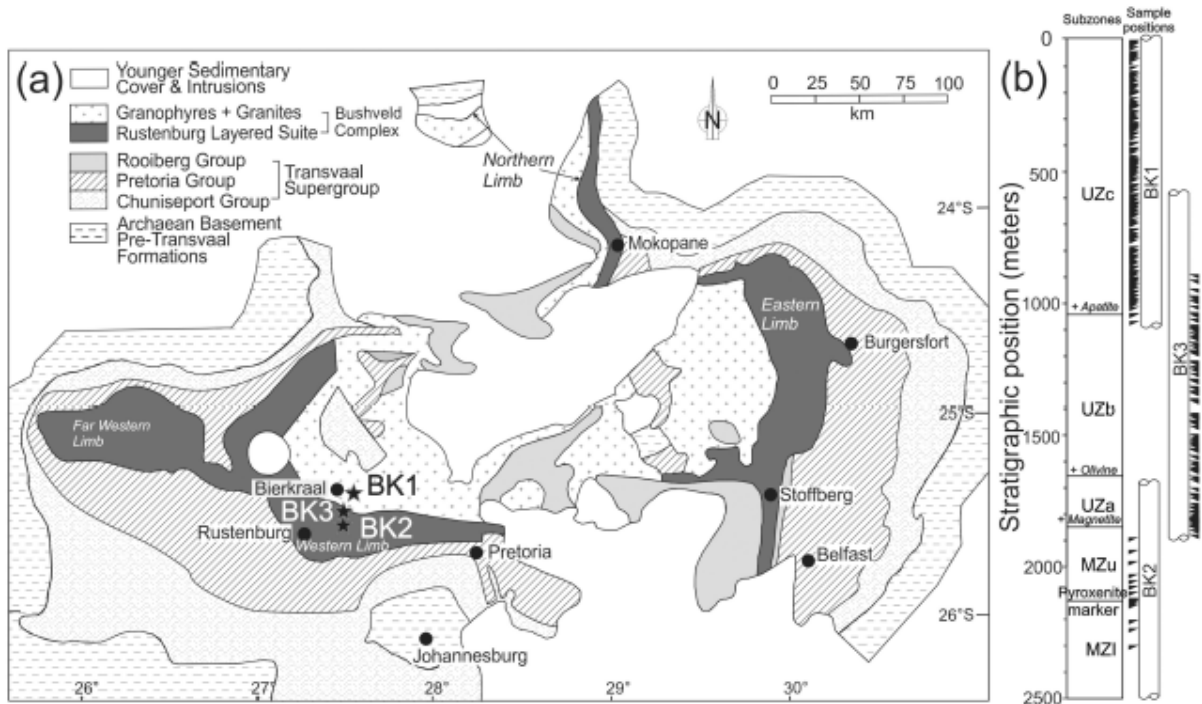


Figure 12. Locations of the drill holes on the Bierkraal farm (9a); stratigraphic locations with the depths of the boreholes (b), as earlier modified after Barnes & Maier (2002) and Yuan et al. (2017).

Several authors have conducted detailed studies on the drill cores, with an emphasis on the origin of magnetite. However, there is a lack of detailed petrography for the area. The correlation of the drill cores is visible in the stratigraphic position of the MML for BK3 and BK2 (Fig. 12b). The appearance and crystallisation of apatite for BK3 and BK1 support this correlation (Walraven & Wolmarans, 1979; Kruger et al. 1987; Tegner et al. 2006). The entire up-to-bottom sequence contains a maximum interval from 415 m to 1 600 m in depth for BK1, followed by 550 m to 1 420 m in depth for BK3, and the bottom interval depth is from 200 m to 673 m for BK2. Walraven & Wolmarans (1979) assumed and identified the core as vertical and the layering of the igneous strata as dipping $\sim 24^\circ$ NNE. As such, Yuan et al. (2017) aimed to correct the gap/distance between individual sample locations and individual stratigraphic positions. According to Tegner et al. (2006), the stratigraphic positions are marked using a metre scale, and diorite marks the ‘zero metre’ reference level (411.8 m for BK1). The overall stratigraphic thickness determined in the current research project aligns with that of Yuan et al. (2017), namely $\sim 2\,128$ m.

Samples from the Scotia Arc (which is situated between South America and Antarctica and is one of the Earth's most important ocean gateways and former land bridge) derive from several projects, one of which was conducted by Harvey & Atkin (1982). These authors oversaw the chemical

analysis of over 100 samples from various locations in the Scotia Islands. The analysis process includes crushing and milling of rocks, followed by X-ray fluorescence (XRF) analysis. The application of inductively coupled plasma mass spectrometry (ICP-MS) complements the XRF results. From these processes and results, elements can be identified for statistical analysis and any anomalous signatures. This can be used to highlight or eliminate geological processes, based on elemental enrichments or depletions.

Shaw et al. (2008) conducted the analytical procedures for samples from the Mariana Arc in the western Pacific Ocean, north of Guam. Generally, all the trace element samples from various locations on the island were prepared and analysed using procedures similar to those employed for the samples from the Scotia Islands. However, owing to the wide range of volcanic processes, the sampling methods differed slightly.

Data processing

In the current research project, trace element observations and analyses were limited to 11 trace elements based on the available data from the Bierkraal drill cores. The lack of a full array of trace elements for this study implies that the results could become preliminary if new data became available for the study area. However, the 11 trace elements anchor the results of this study. Several trace elements classify as transition metals (Cr, Co, Ni, Cu, and Zn), followed by large-ion lithophile elements (LILEs, such as Rb, Sr, and Ba). High field-strength elements include Zr and Nb, and Y is the only REE in the Bierkraal borehole data.

A comprehensive database of all the preliminary locations was generated using the Excel application (Microsoft, USA), including SiO₂ and MgO as major elements. The cleaning of tectonic settings focus on the separate basaltic geochemical data. The cleaning process entails identifying and discarding relevant outliers using the interquartile range statistical approach, derived from Tukey (1977). Tukey's method is a statistical approach used to determine whether a value should be considered an outlier or not. In this method, demarcation of subsequent boundaries is conducted

using the upper and lower quartiles. The establishment of the database continued with PCA, using both the GeoChemical Data toolkit GCDkit and ioGAS™, which are geochemical data exploration software. Janousek et al. (2006) described GCDkit as statistical and graphical software that manages and interprets various forms of data. A PCA approach was adopted for these data, as it could be a valuable tool for identifying elemental associations within a large dataset.

Brief theoretical introduction to Principal Component Analyses

This multivariate statistical approach does not require a hypothesised approach to generate a probability distribution for the variables (Jimenez-Espinosa et al., 1993). A subgroup of correlated variables is identified from a geochemical dataset; therefore, several components are sampled from the original data as linear functions (Jimenez-Espinosa et al., 1993). Normalising the input trace element data helps negate the influence of extreme values. One main advantage of PCA in exploration is its ability to distinguish elemental associations within the correlation matrix structure into several groups of elements (in this instance, trace elements), thereby accounting for most of the variation observed in the original data (Jimenez-Espinosa et al., 1993). Accordingly, a limited number of components represents multiple/several elements in the original dataset. The individual components represent linear functions of elemental concentration, thereby providing broader efficiency regarding information deflation/compression over the original dataset while enhancing its interpretability. As a PCA can only generate components using the original number of variables in the dataset, limitations are placed on data generated from a small number of samples.

Potential geological processes are inferred through elemental enrichment or depletion using the multivariate data from the PCA. In other words, this statistical approach initiates geochemical investigations rather than identifying and instantaneously solving geological problems. In this approach, trace elements highlighted by the PCA drive the geochemical investigation. The resulting PCAs are used, subsequently, to narrow down the tectonic settings. To obtain credible results in the current study, only the generated results were analysed, with previous publications considered for interpretation. The REE data from tectonic settings identified by PCA are normalised to MORB (after Gale et al., 2013). The computer applications mentioned above produced the statistical and graphical outputs from the data.

CHAPTER 4 - RESULTS

The analytical data and results of this study derived from the procedures explained in Chapter 3 (Methodology). Overall, 336 samples were analysed in this study with the PCA anchors. Figure 13 shows the sample frequencies from the various locations.

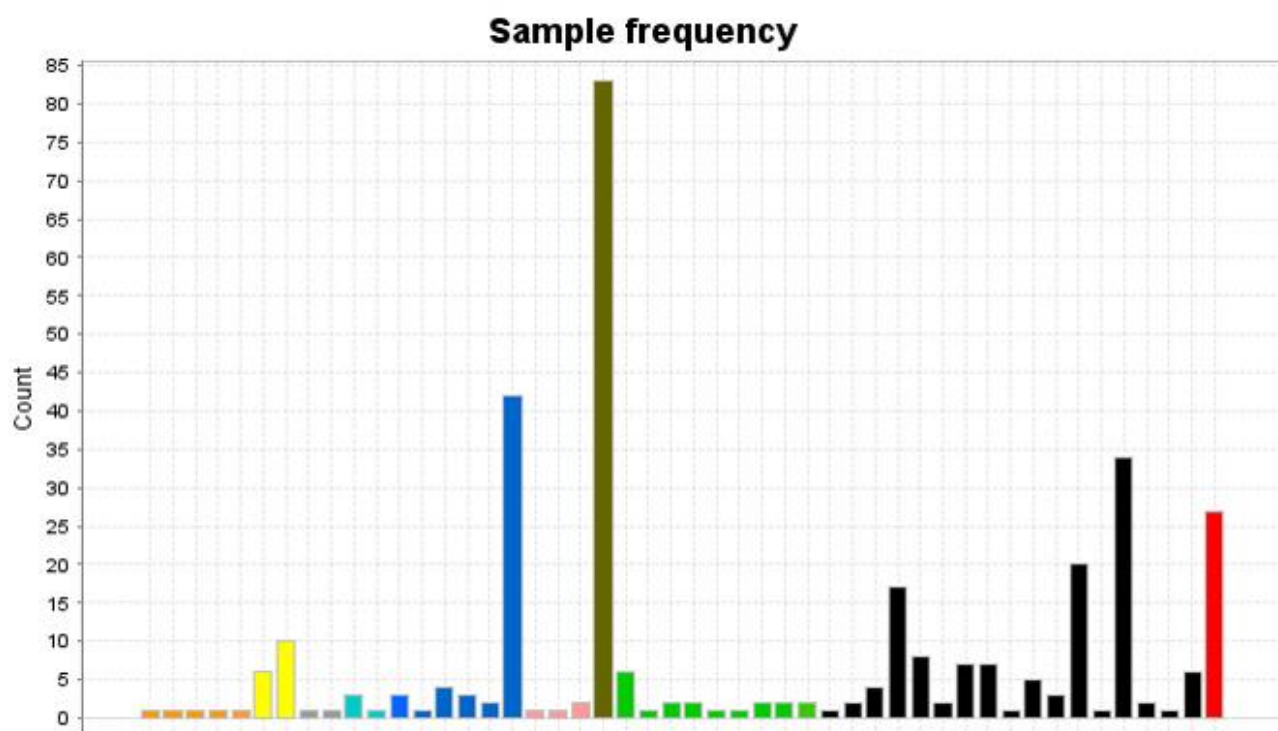


Figure 13. Sample location frequencies. The colours olive, blue, green, and black represent the Ryukyu, Mariana, Scotia, and Tongan arcs, respectively. Orange, grey, and sky blue represent the Caribbean–Colombian, Kerguelen, and Manihiki plateaus, whereas yellow indicates the Hawaiian Islands, pink (Ninety East Ridge), and red (Upper Zone of the Bushveld Complex). The Ninety East Ridge is a mid-ocean ridge on the Indian Ocean floor named for its near-parallel strike along the 90th meridian at the center of the Eastern Hemisphere.

The locations in this study included convergent margins (Tonga, Mariana, Scotia, and Ryukyu), oceanic plateaus (Caribbean–Colombian, Kerguelen, and Manihiki), oceanic island (Hawaii), and submarine ridges (Ninety East Ridge). This study relied on the concept of comparing these locations with the tectonic settings above. These settings range from ocean islands (Hawaii), convergent margins (Tonga, Mariana), and available trace element data (limited to Cr, Co, Ni, Cu, Zn, Rb, Sr, Y, Zr, Nb, and Ba) from the Upper Zone of the Bushveld Complex. Owing to the limited trace element data, an unwanted constraint was placed on several locations, disqualifying them from the study. The result is a slight skewness in the sample frequencies, evidenced by convergent margin dominance followed by oceanic plateaus (Fig. 13).

The PCA conducted in this project focused on convergent margins, oceanic plateaus, oceanic islands, and submarine ridges. Most trace element values derive from XRF analysis, with subtle variations in the methods of sample collection. Notwithstanding the high number of samples, a covariance matrix approach to the PCA was followed, as the values used in the study were at the same scale (ppm). In contrast, a correlation matrix approach could be followed with samples (in this case, trace elements) not at the same scale. Figure 14 shows the PCA results for this study.

There is an overlap between the Upper Zone data and those for Tonga, Mariana, Scotia and, to a minor extent, Hawaii (Fig. 14). The remaining locations are spread out/distal from the identified overlaps. A frequent problem with 2D biplots is a lack of accuracy in representing the dataset. However, in this study, the problem was avoided, as the software was able to draw 3D biplots. A link to the biplots is provided in the appendix. Upon rotation of the 3D biplot, only Tonga, Mariana and Scotia were close to the Upper Zone data.

The trace elements accounting for the most variation in the first principal component are Cr and Ni and, on the opposite end of the coefficient spectrum, Sr, and Ba. The same trace elements are influential in the second principal component, with the only difference being that all have positive coefficients. The first two principal components contribute ~89.247% of the total variation (Table 1) and the remaining principal components represent ~10.753% of the overall variation. The first two principal components are, therefore, crucial for analysing and describing variation in the samples in this study.

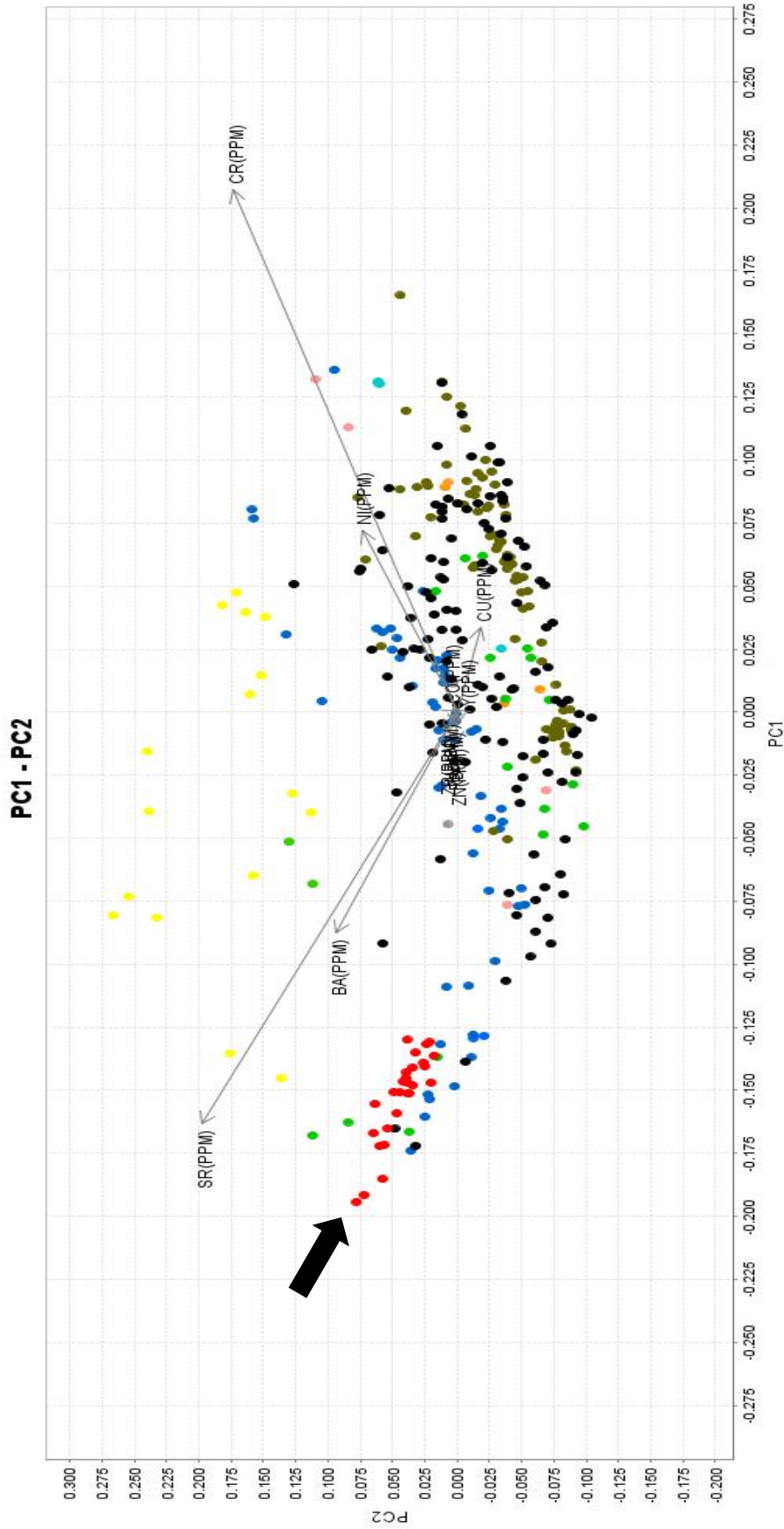


Figure 14. Biplot (2D) representing the first (PC1) and second (PC2) principal components, with the black arrow indicating the Upper Zone data (red). Note that the following locations are distinguished by the corresponding colours: Mariana (blue), Tonga (black), Scotia (green), Hawaii (yellow), Manihiki (light blue), Ryukyu (olive green), Ninety East Ridge (pink), Caribbean Colombian (orange) and Kerguelen (grey).

Table 1. Eigenvalues and cumulative frequencies of the 11 principal components

Table 1. Eigenvalues and cumulative frequencies of the 11 principal components

<u>Column 1</u>	<u>Eigenvalues</u>	<u>Percentage</u>	<u>Cumulative frequency</u>
PC1	24 762,97	54,383	54,383
PC2	15 875,30	34,864	89,247
PC3	1 760,97	3,867	93,115
PC4	1 028,91	2,260	95,374
PC5	981,41	2,155	97,530
PC6	793,30	1,742	99,272
PC7	252,06	0,554	99,826
PC8	49,68	0,109	99,935
PC9	14,93	0,033	99,967
PC10	11,00	0,024	99,992
PC11	3,82	0,008	100,000

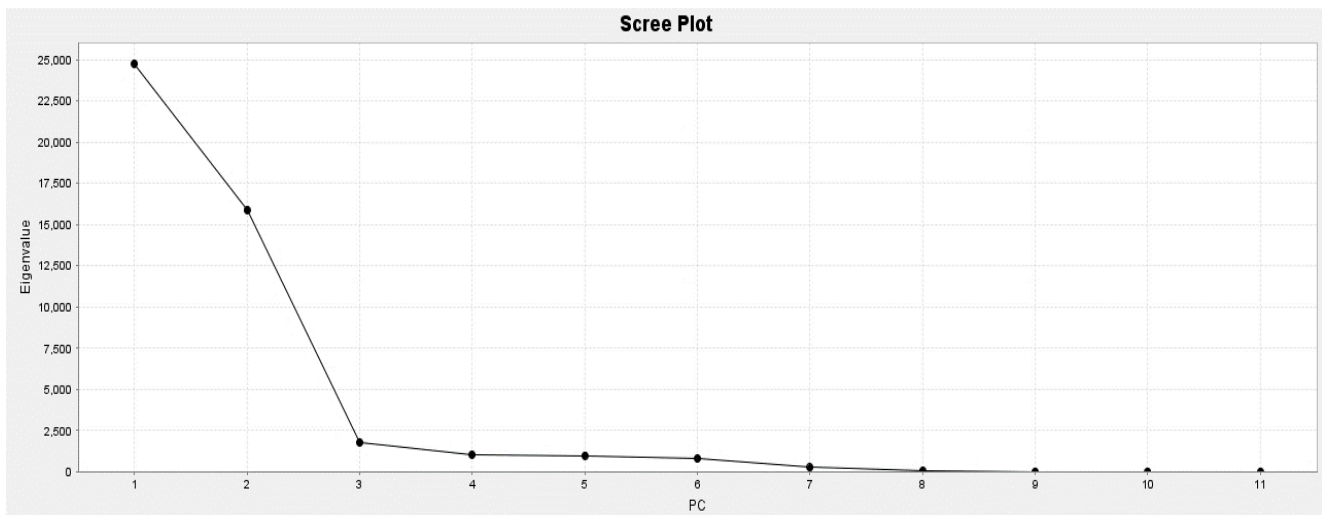


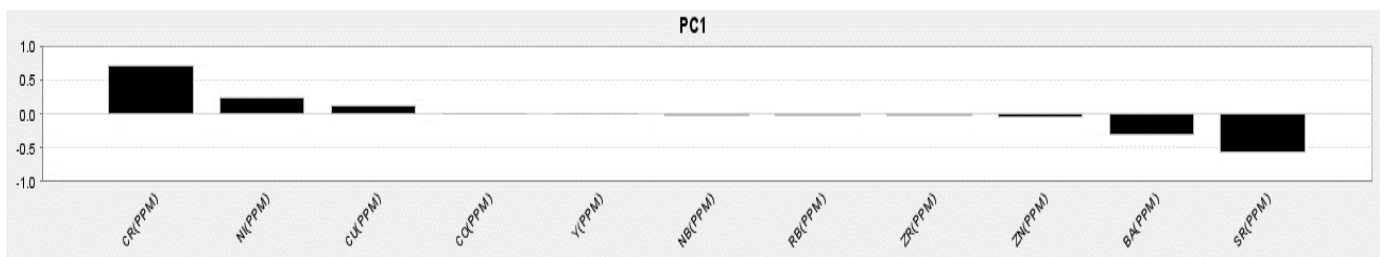
Figure 15. Scree plot of the eigenvalues generated by the principal components.

Table 2. Eigenvector contributions for all trace elements in the principal components.

<u>Eigenvectors (ppm)</u>	<u>PC1</u>	<u>PC2</u>	<u>PC3</u>	<u>PC4</u>	<u>PC5</u>	<u>PC6</u>	<u>PC7</u>	<u>PC8</u>	<u>PC9</u>	<u>PC10</u>	<u>PC11</u>
Cr	0,716	0,599	0,030	0,157	0,109	0,301	0,044	0,006	0,005	0,007	0,004
Co	0,004	0,011	-0,045	0,037	0,053	-0,102	0,363	-0,917	-0,011	-0,043	0,095
Ni	0,249	0,249	0,017	-0,434	-0,170	-0,806	-0,057	0,044	0,001	0,002	0,007
Cu	0,117	0,117	-0,942	0,060	-0,285	0,029	-0,088	-0,007	-0,024	0,030	-0,005
Zn	-0,042	-0,042	-0,171	-0,204	0,235	0,003	0,862	0,356	-0,045	0,003	0,008
Rb	-0,018	-0,018	0,017	-0,005	0,054	-0,011	-0,001	-0,050	-0,127	0,985	-0,083
Sr	-0,564	-0,564	0,011	-0,003	-0,437	0,129	0,092	0,001	0,002	0,007	-0,004
Y	0,002	0,002	-0,032	-0,146	0,014	0,071	0,018	-0,027	0,977	0,120	-0,052
Zr	-0,027	-0,027	-0,072	-0,835	0,164	0,423	-0,210	-0,141	-0,153	-0,029	0,059
Nb	-0,008	-0,008	-0,017	-0,036	0,049	-0,002	0,018	-0,088	-0,049	-0,097	-0,988
Ba	-0,303	-0,303	-0,271	0,144	0,773	-0,219	-0,243	0,000	0,036	-0,037	0,045

Overall, eigenvalues indicate to what extent the data are spread out in a specific direction. Figure 15 shows that the first two principal components represent most of the variation in the dataset. The eigenvalues for the first and second principal components vary more than the rest of the components.

a.



b.

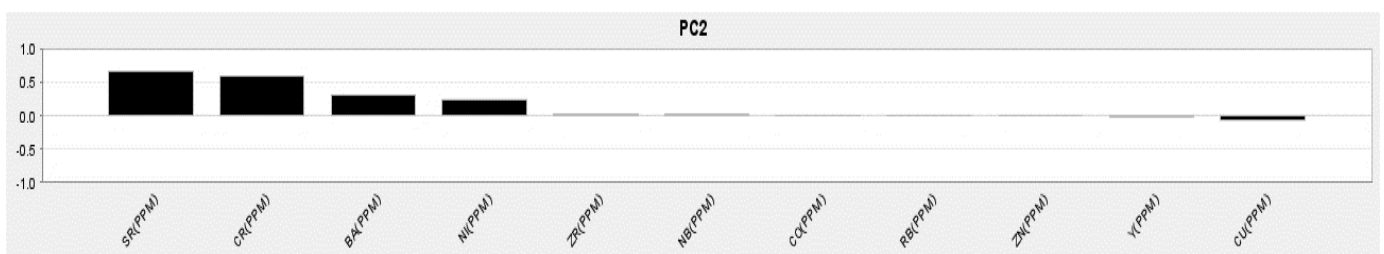
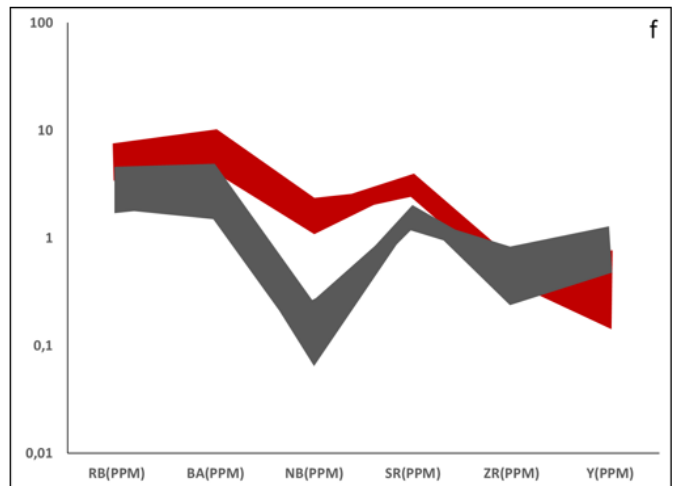
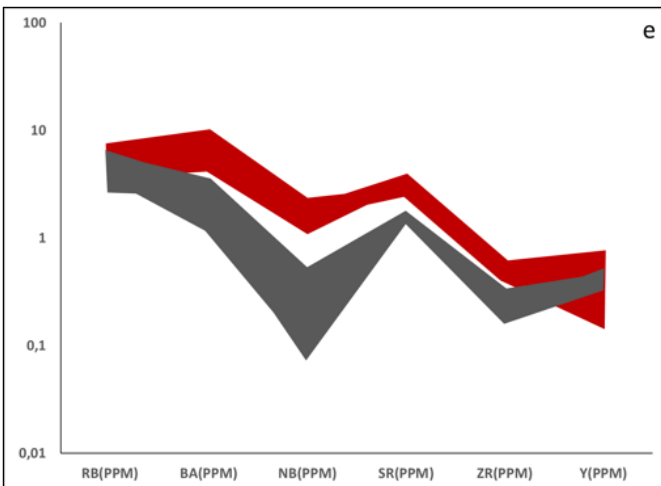
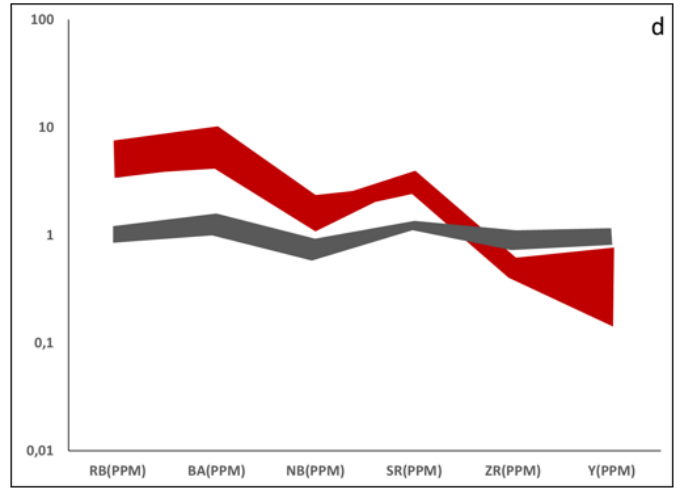
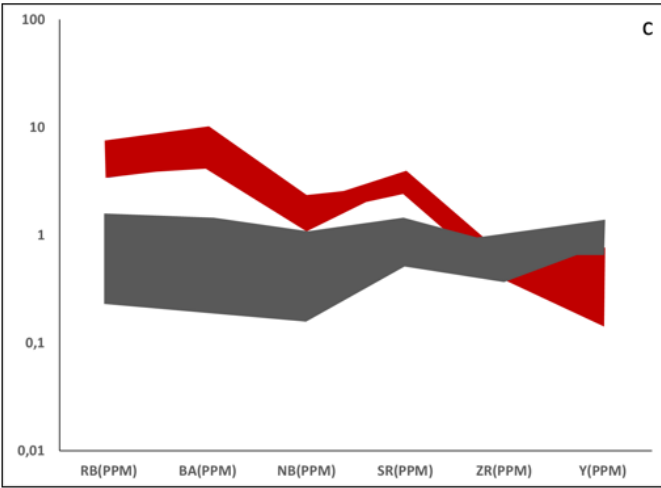
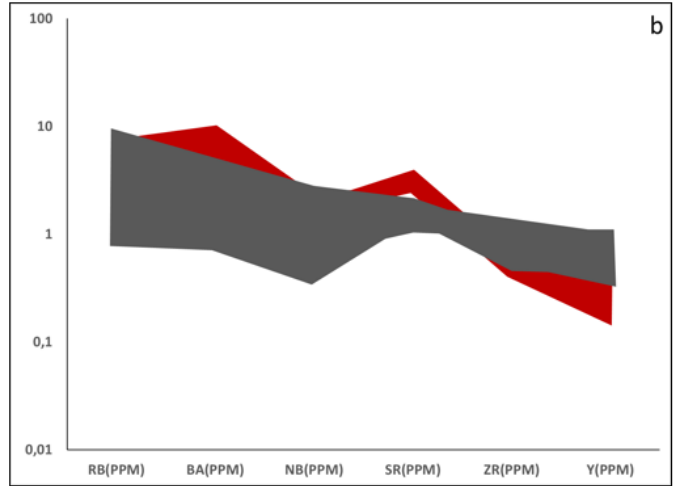
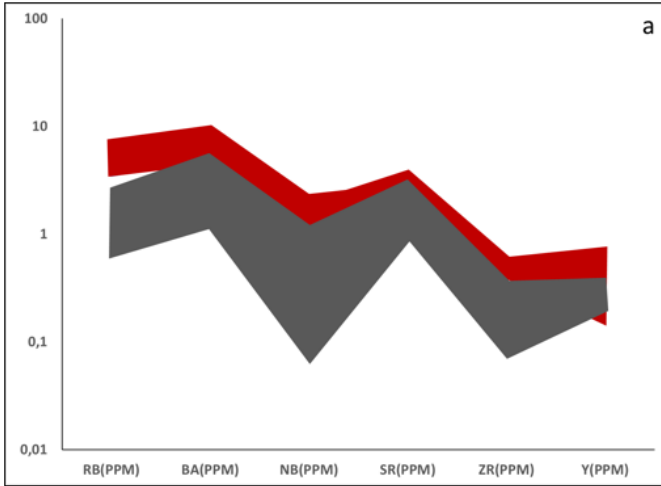


Figure 16. Eigenvector plots for a) the first (PC1), and b) the second (PC2) principal components of the dataset.

The first principal component accounts for ~54.383% of the variation (Table 1), with Cr and Ni having positive loading coefficients, and Sr and Ba with negative loading coefficients (Fig. 16a). The second principal component accounts for ca 34.864% of the variation. The most significant trace elements in the second principal component (PC2) are Sr, Cr, Ba, and Ni, all with positive loading coefficients (Fig. 16b). These observations are supplemented and supported by the eigenvectors shown in Table 2. The PCA indicated specific tectonic settings represented by Tonga, Mariana, Scotia, and Hawaii. Figure 17 shows the spider diagrams created for these tectonic settings, with MORB normalising values from Gale et al. (2013).

Comparison of Bierkraal trace element data to identified tectonic settings

The samples from Tonga generally show depletion of Y and Zr, with a negative Nb anomaly compared with those from the Bushveld that show enrichment of Sr, Ba, and Rb. The Tonga islands, Fonualei spreading centre and the Fiji Islands (Fig. 17a, e, h) show a geochemical signature most similar to that of the Bushveld. The samples from Scotia and Mariana show depletion of Nb similar to that of Tonga and the Bushveld, and consistent depletion of Zr and Y. Although certain trace elements are distributed unevenly in this dataset (Figs 18 and 19), similarities with those of the Bushveld Complex are observed. For example, Scotia and Mariana show enrichment of Ba and Sr, which are highly incompatible trace elements. The most consistent and similar trace element spider plot to the Bushveld Bierkraal data is that of the Hawaiian Islands (Fig. 20). The geochemical signature of Hawaii is consistent with that observed in the Upper Zone of the Bushveld Complex, with samples from Nihau (Fig. 20a) showing enrichment of Ba, Sr, and Nb and depletion of Zr and Y. The Hawaiian Island Kaula shows the most enrichment in highly incompatible elements, with a few samples showing depletion of Y and Zr. Generally, Hawaii shows a negative Zr anomaly.



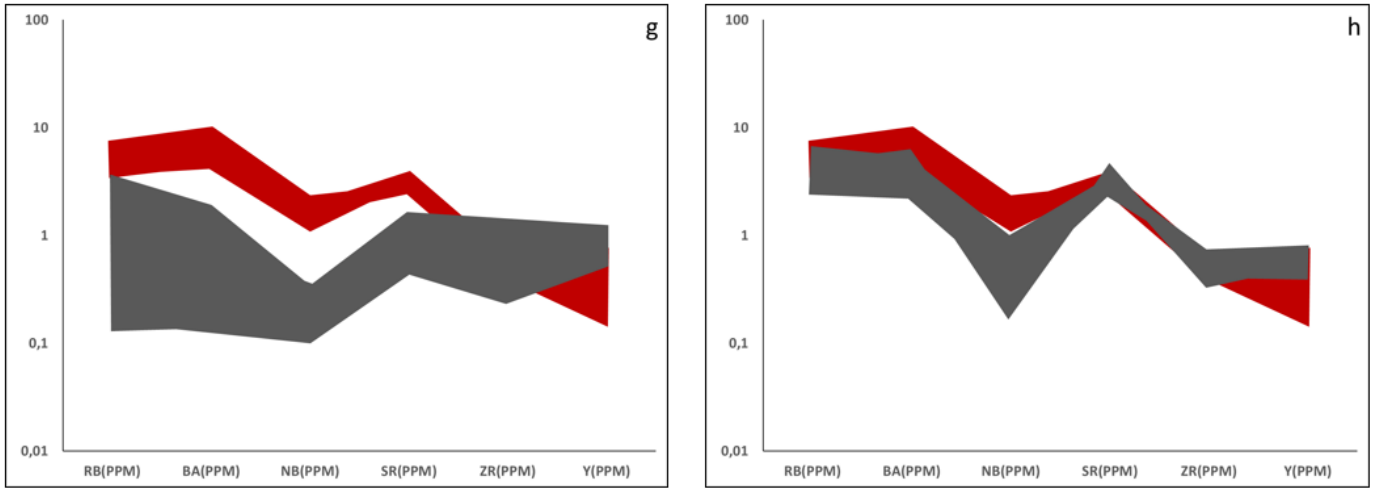
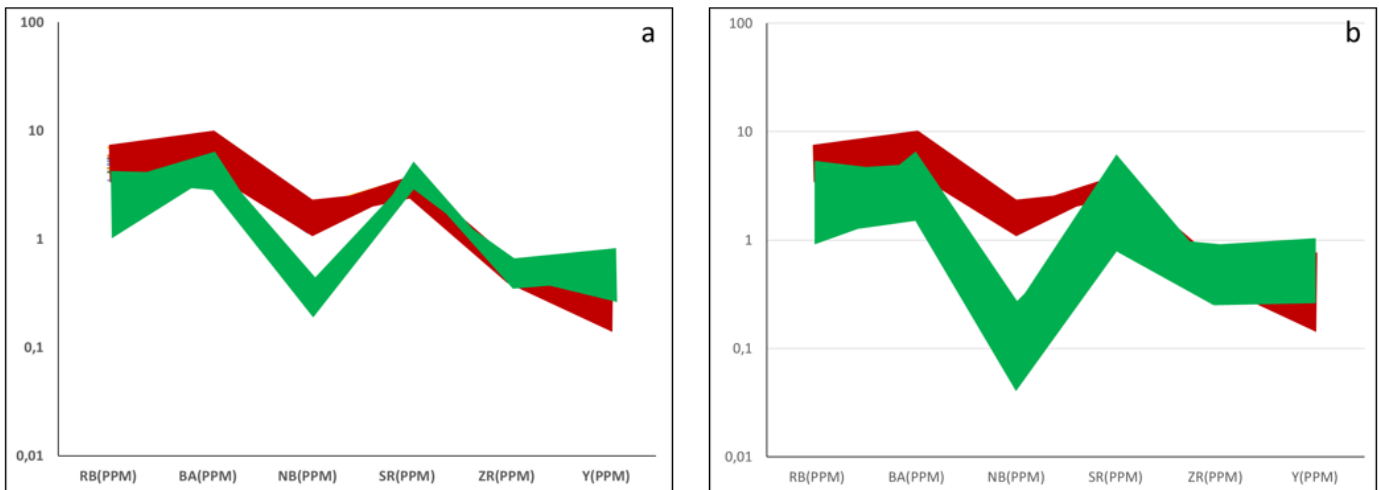


Figure 17. MORB normalised trace element concentration plots (modified after Gale et al., 2013) sampled from convergent margins around Tonga (dark-grey colour). (a) Tonga islands; (b) Rochambeau ridge–Lau basin; (c) Northwest spreading centre; (d) Niuafu'ou–Lau basin; (e) Fonualei spreading centre; (f) Eastern Lau spreading centre; (g) Central Lau spreading centre; (h) Fiji islands. The red line represents the Bierkraal data from the Upper Zone of the Bushveld Complex.



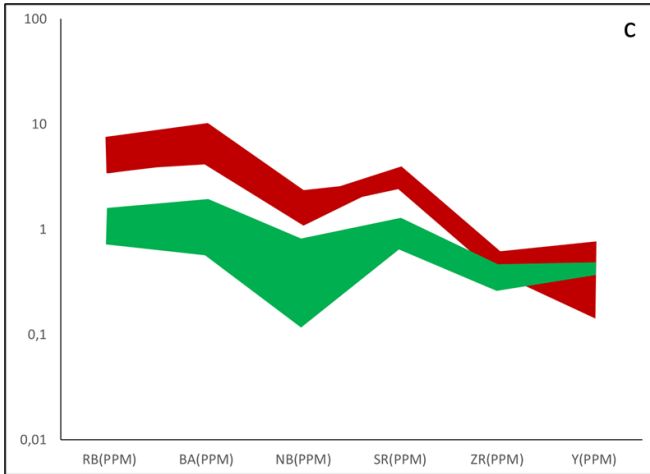
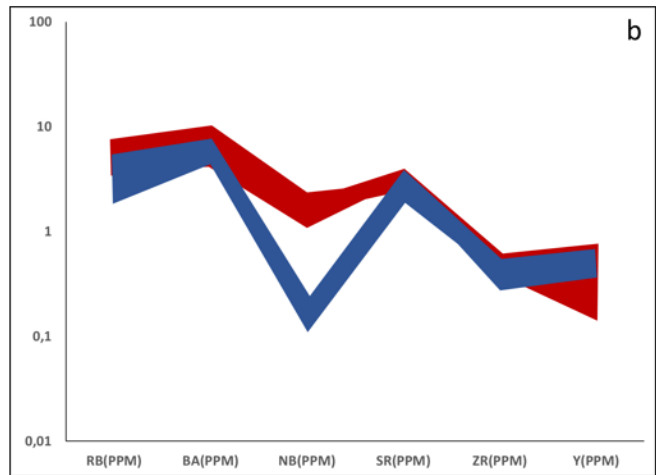
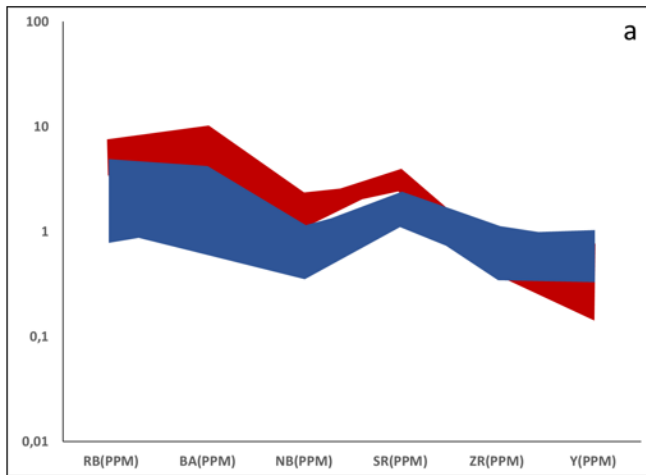


Figure 18. MORB normalised trace element concentration plot (modified after Gale et al., 2013) sampled from convergent margins around Scotia (green colour), with (a) the South Shetland Islands; (b) South Sandwich Island arc; (c) South Sandwich arc basin. The red pattern represents the Bushveld data.



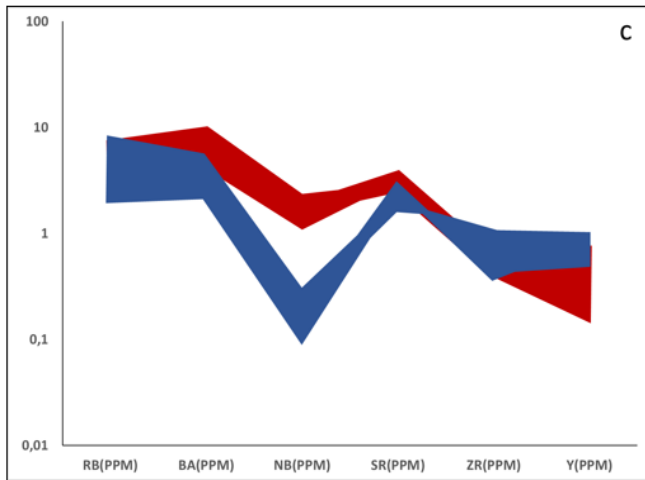
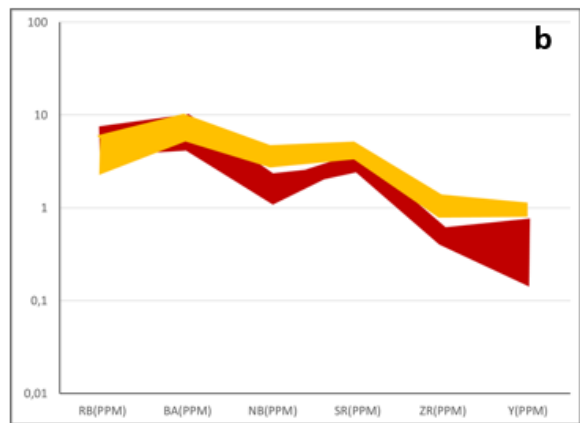
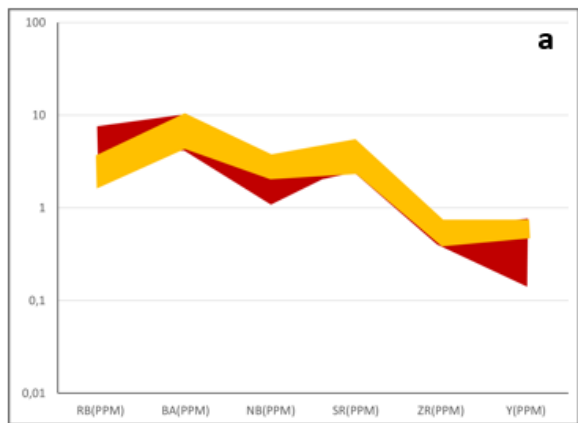


Figure 19. MORB normalised trace element concentration plot (modified after Gale et al., 2013) sampled from Mariana (blue colour), with (a) Mariana trough; (b) Mariana arc; (c) Kyushu–Palau Ridge. The red pattern represents the Upper Zone data.



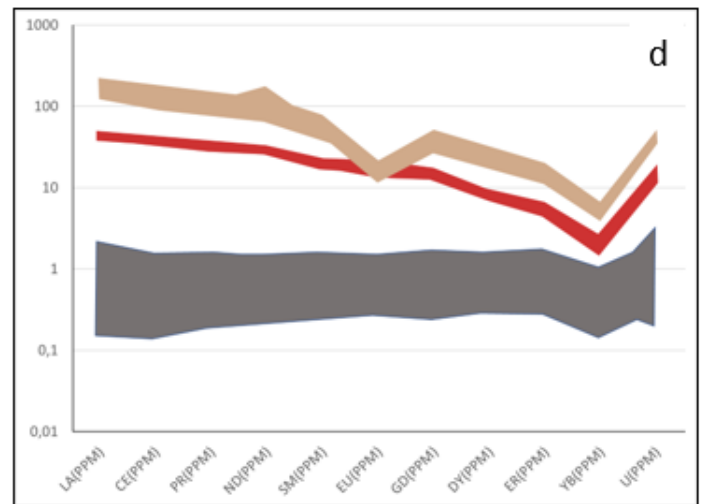
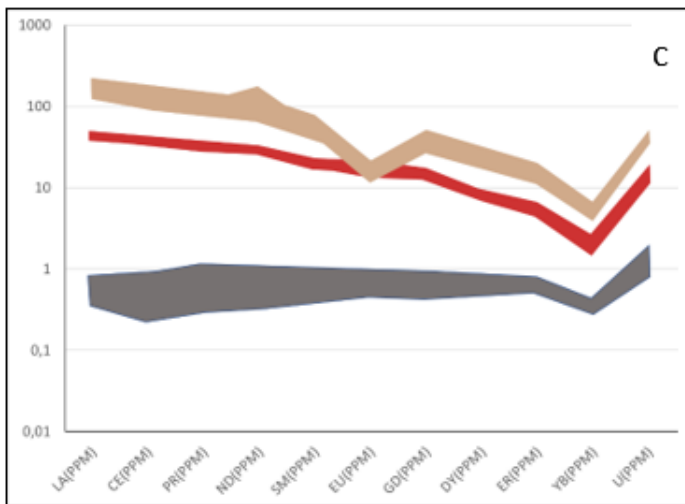
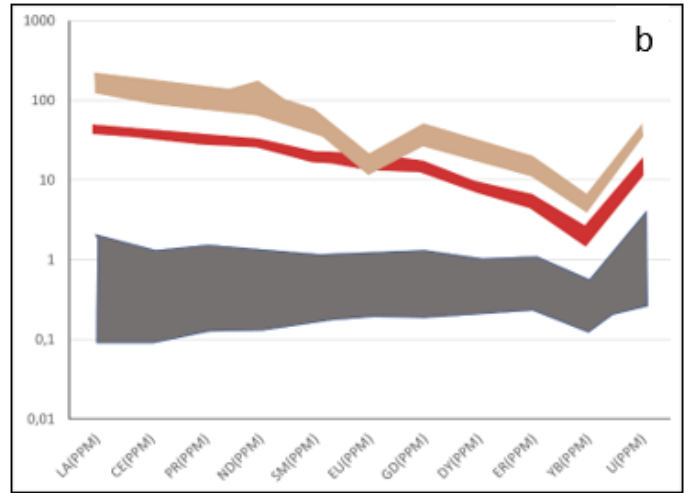
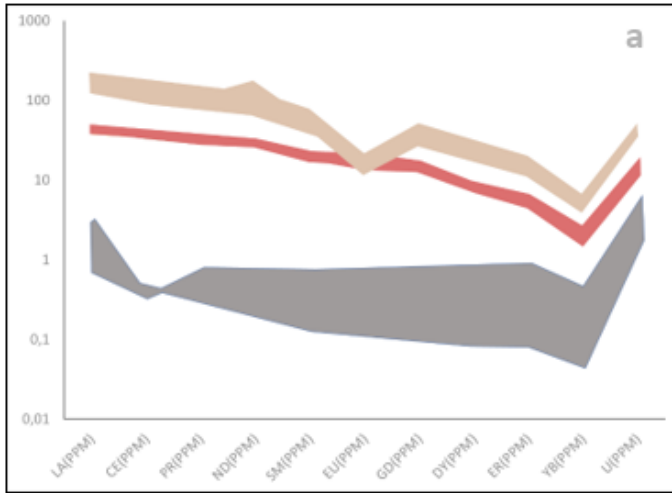
Figure

20. MORB normalised trace element concentration plot (modified after Gale et al., 2013) sampled from the Kure Atoll (or Ocean Island) of Hawaii (yellow colour), with (a) Nihau and (b) Kaula. The red pattern represents the Bushveld data.

Rare Earth Element data (apatite)

Analyses of REE data from the Upper Zone of the Bushveld Complex (after Van Tongeren & Mathez, 2012, were incorporated to complement the trace element borehole data. The REE concentrations derive from two populations of apatite around Magnetite Layer 21. The REE spider diagrams (Figs 21–24) were constructed and normalised to MORB (after Gale et al., 2013). Overall, the REE samples were collected and analysed from the top 625 m of the Upper Zone of the Bushveld Complex (Magnetite Layer 21). The REE spider plots supplemented with U (Figs 21–24) show two different patterns from the data sampled from the complex. Samples from the lower 300 m (red-shaded pattern) show relatively low REE concentrations, whereas those from the upper 325 m (light-brown pattern) have relatively higher concentrations and an apparent negative Eu anomaly. From the identified tectonic settings, no samples show a pattern similar to that observed from the upper 325 m of the complex, or the Eu anomaly. Ultimately, the only similarities between the tectonic settings and the Bushveld data pertain to the lower 300 m section. Most tectonic samples have a relatively high U concentration and visible Yb depletion compared with the rest of the REE.

The REE pattern of the Bushveld (Figs 21a–24e) shows enrichment of both light REE (LREE) and heavy REE (HREE) compared with that of Tonga. The Tonga Trench (Fig. 21a) shows the only Ce anomaly and a less-gentle pattern in the Tonga data. Tonga and the Bushveld Complex have no clear and straightforward similarities, with the closest signatures observed in the Tonga and Fiji Islands (Fig 21b, e). Figure 22 shows a flat REE pattern for Scotia. Arguably, the East Scotia Ridge (Fig. 22d) is unique in that it has an REE pattern similar to that observed from the lower 300 m of the Bushveld Complex. Note that the East Scotia Ridge samples were limited to two owing to data availability. Mariana (Fig. 23) has an REE pattern similar to that observed in Scotia. These observations imply that the patterns lack LREE and HREE compared with those of the Bushveld Complex. Hawaii (Fig. 24) shows the highest overall enrichment of REEs outside the Bushveld data.



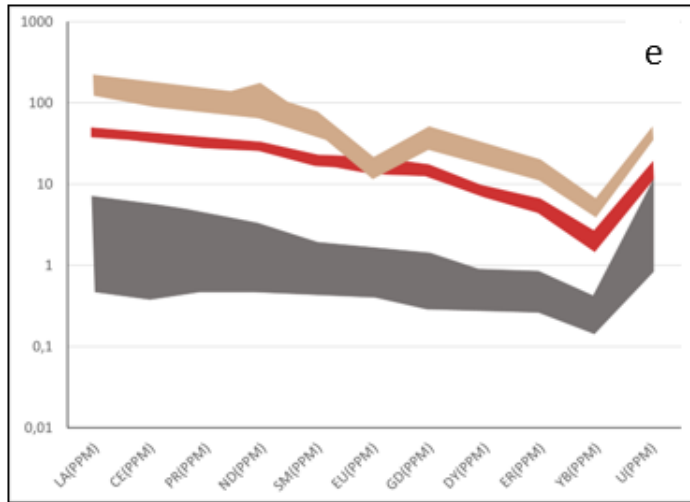


Figure 21. MORB normalised rare earth element concentrations (modified after Gale et al., 2013) sampled from convergent margins in and around Tonga (grey colour), with (a) Tonga Trench; (b) Tonga islands; (c) Tonga forearc; (d) Lau basin (e) Fiji Islands. Note that the red and light-brown lines represent two different populations of apatite sampled from the Upper Zone of the Bushveld Complex.

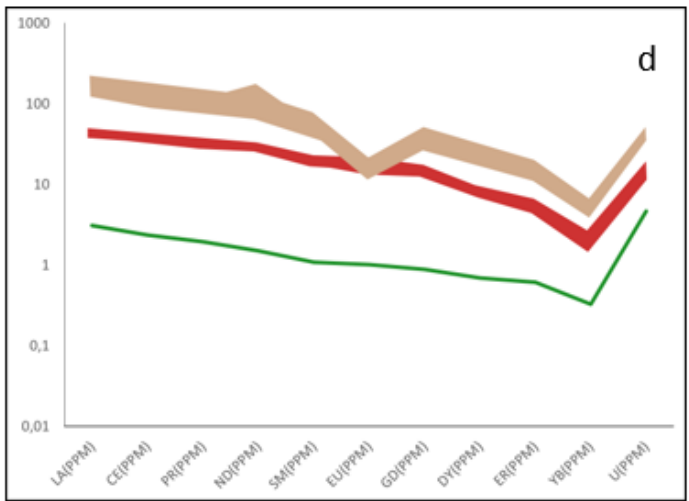
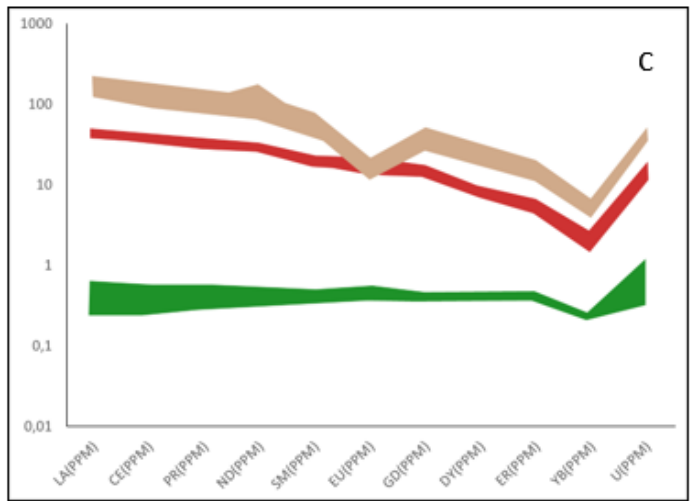
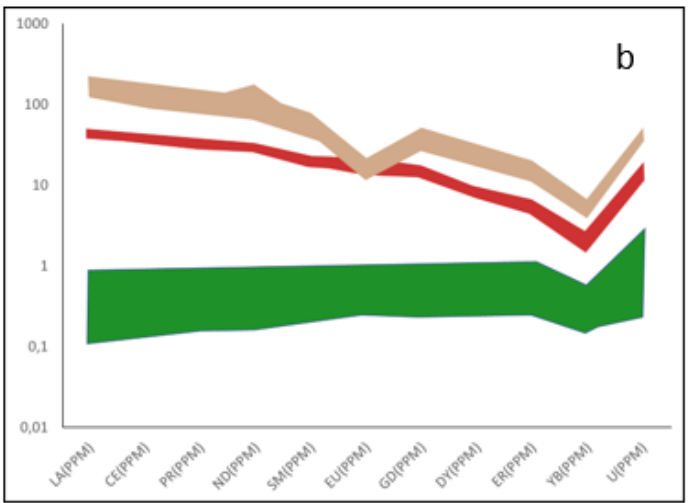
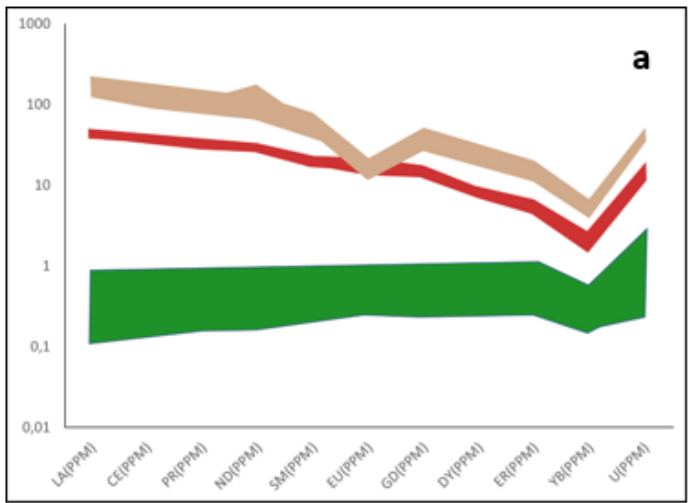
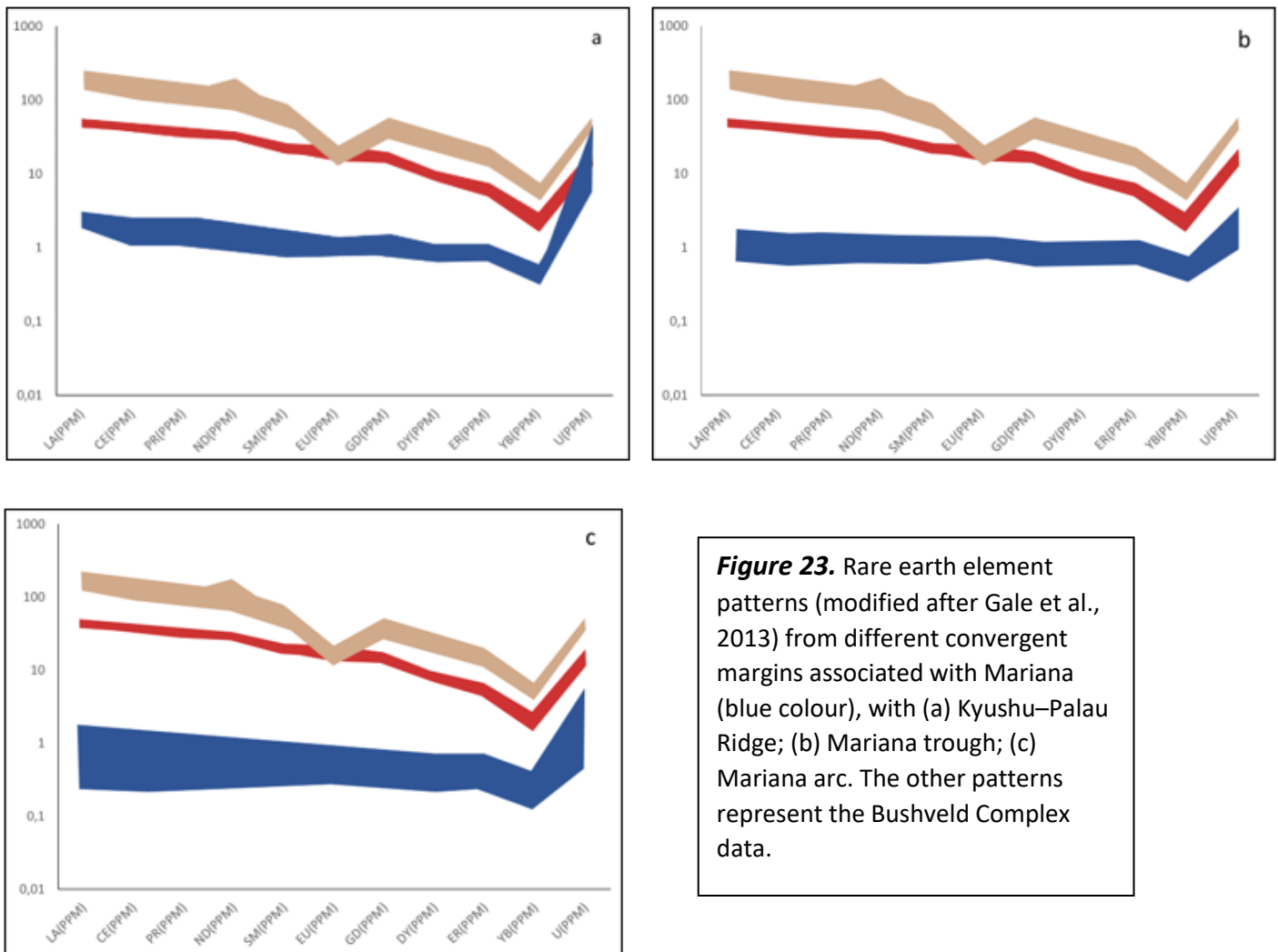


Figure 22. MORB normalised rare earth element concentrations (modified after Gale et al., 2013) sampled from different locations in Scotia (represented by the green colour), with (a) South Shetland Island arc; (b) South Sandwich Island arc; (c) South Sandwich arc basin; (d) East Scotia Ridge. Note that the red and light-brown lines represent two different populations of apatite sampled from the Upper Zone of the Bushveld Complex.



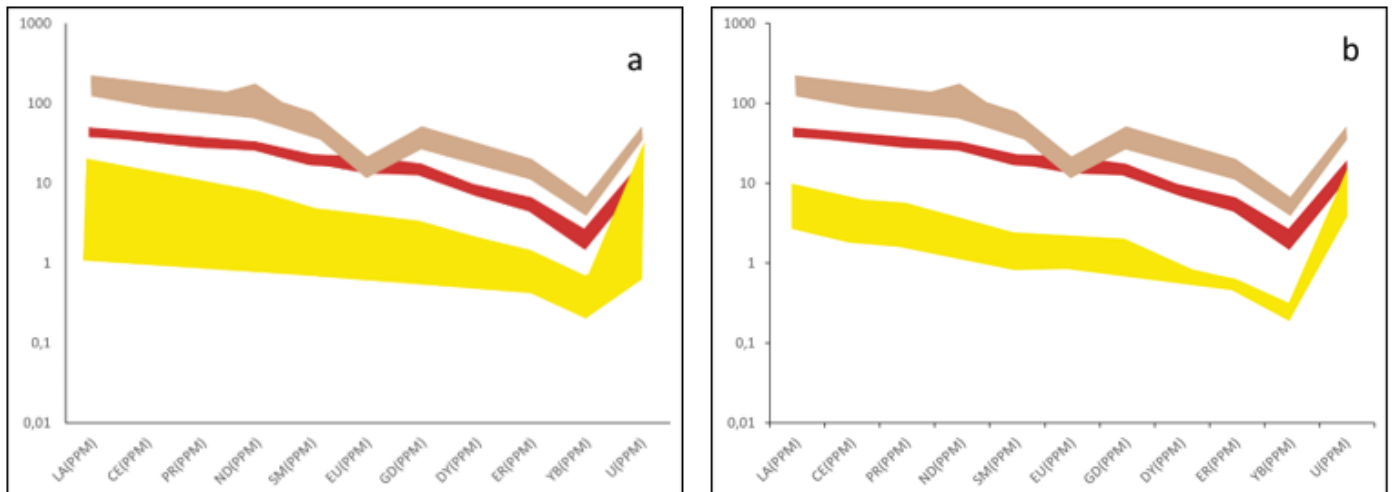


Figure 24. MORB normalised rare earth element concentrations (modified after Gale et al., 2013) sampled from the Ocean Island of Hawaii (yellow colour), with (a) the Hawaiian Islands and (b) the Hawaiian arch. Note that the red and light-brown lines represent two different populations of apatite (lower 300 m and upper 325 m, respectively) sampled from the Upper Zone of the Bushveld Complex.

CHAPTER 5 - DISCUSSION

The PCA results (Fig. 14) show clear differentiation between the data from known tectonic settings and those from the Upper Zone because the Upper Zone data plot in a relatively different location than most other tectonic settings. The settings plotting in proximity to/overlapping with the Upper Zone are Tonga, Mariana, Scotia, and Hawaii. The first three tectonic environments represent subduction-zone–arc-related settings, whereas Hawaii is an example of an oceanic island. As a result, the samples overlapping with the Upper Zone contain upper mantle components, resulting in a somewhat primitive geochemical signature. Subduction zones offer a different geochemical designation because of the influence of sediments and water that accompany the oceanic crust, which generally subducts during the convergence of plate boundaries. Subsequent plotting of discriminant diagrams should further identify geochemical similarities between the settings. Generally, the most accurate identification of tectonic settings relates to basaltic rocks, and various discriminant diagrams could be helpful tools. According to Wilson (1989), the most accurate identification of tectonic settings has been achieved for basaltic rocks that were not generated and erupted within continental plate environments. In other words, basaltic rocks that originate outside of continental settings, such as those found in oceanic environments, have been more reliably associated with specific tectonic settings.

Discriminant diagrams — Bierkraal borehole data

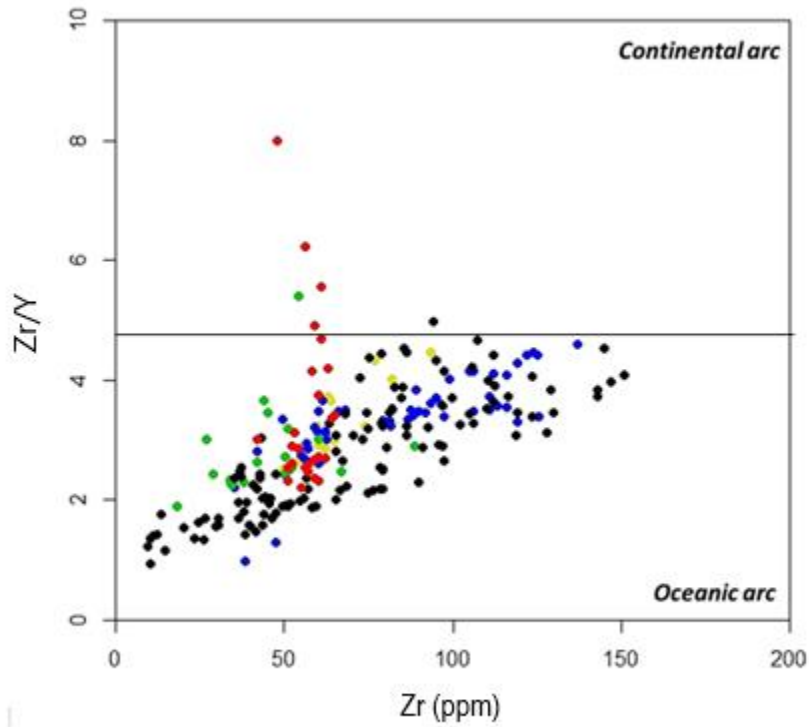


Figure 25. Volcanic discriminant diagram comparing continental and oceanic geochemical arrays (modified after Pearce, 1983). The tectonic settings are colour coded similar to the previous diagrams, with red indicating Bushveld data; black: Tonga; blue: Mariana; green: Scotia; yellow: Hawaii.

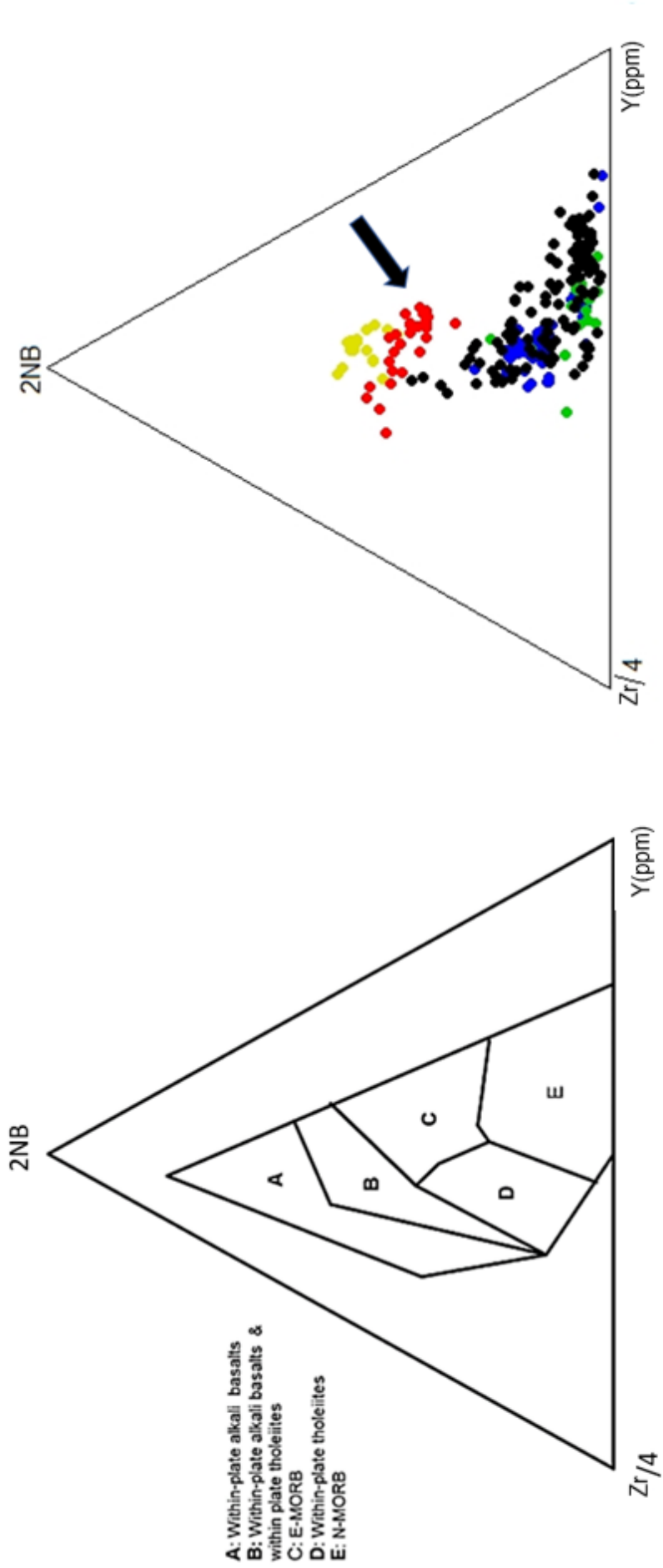


Figure 26. Ternary discriminant diagram for various MORB and continental tholeiites (modified after Meschede, 1986). The arrow indicates the Bushveld data relative to the other locations.

Figure 25 shows a volcanic discriminant diagram for subduction-related volcanic rocks, indicating that most rock samples (ca 95%) plot under the oceanic arc region. In contrast, a few samples from the Bushveld Complex (BK1) have a continental-arc geochemical signature. As the BK2 and BK3 samples have missing trace element values, they were not incorporated into this study. Only two samples from both Tonga and Scotia showed a continental-arc geochemical signature. The sample from Tonga is from the Fiji and Tonga islands, whereas that from Scotia is from the South Shetland Islands. The highest Zr/Y ratio was observed in the continental-arc sample from the Bushveld Complex, whereas oceanic arc samples from Mariana and Tonga showed the lowest concentrations of Zr/Y. The Zr concentration of the Bushveld was within 50 ppm. The Tonga samples showed the most extensive range of Zr concentrations, between 5 and 155 ppm, followed closely by those from Mariana.

The ternary discriminant diagram (Fig. 26) supplements the volcanic discriminant diagram (Fig. 25) and is biased towards MORB magma genesis. Most samples are shown as by-products of a normal (N-)MORB source, with slight variation towards either enriched (E-)MORB or within-plate tholeiites. For example, a Hawaiian source was intermediate between E-MORB and within-plate alkali basalts and within-plate tholeiites. Similarly, the Bushveld data primarily plot within the E-MORB field, with certain factions plotting as within-plate alkali basalts and within-plate tholeiites, which are identical to those plotting under the continental arc, as shown in Figure 25.

Most samples from Mariana, Tonga, and Scotia represent an N-MORB and, to a lesser extent, a within-plate tholeiite magmatic source. Based on this postulation, the magma that constitutes parts of the Upper Zone of the Bushveld derives from within-plate tectonic boundaries. The samples from Tonga plotting close to the Bushveld data are from the islands of Tonga and Fiji and the Hawaiian Islands of Nihau and Kaula.

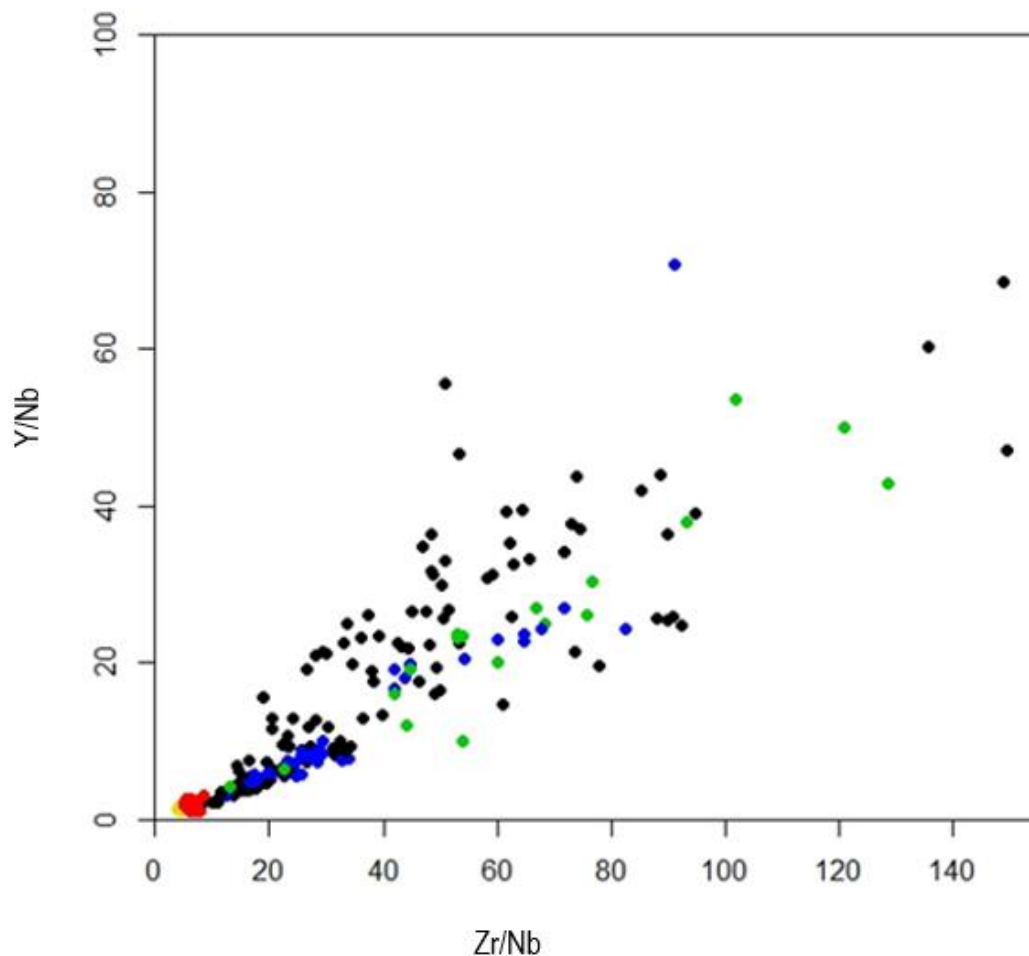


Figure 27. Y/Nb versus Zr/Nb diagram (modified after Xia and Li, 2019; Wilson, 1989).

Figure 27 shows an overlap between the Bushveld data and the data from the Hawaiian islands and Tonga (Fiji and Tonga islands). Based on interpretations from Xia and Li (2019), the overlapping data indicate an E-MORB magmatic source. The Hawaiian islands and most parts of the Bushveld data plot within the mantle plume section of the discriminant diagram. Figure 28 is modified from Figure 27, with the tectonic locations isolated against the Bushveld data.

Figure 28a shows the overlap between data from the Bushveld and Hawaii. This overlap plots within an E-MORB field, which represents the enrichment of most incompatible elements. The results presented in Chapter 4 complement this interpretation. The geochemical signature of Hawaii is consistent with that observed in the Upper Zone of the Bushveld Complex, with samples from Niihau (Fig. 20a) showing enrichment of Ba and Sr, which are LILEs, and Nb, which is a high field-strength element (HFSE), as well as depletion of

Zr and Y. The Hawaiian island of Kaula shows the most enrichment in highly incompatible elements, with a few samples depleted in Y and Zr.

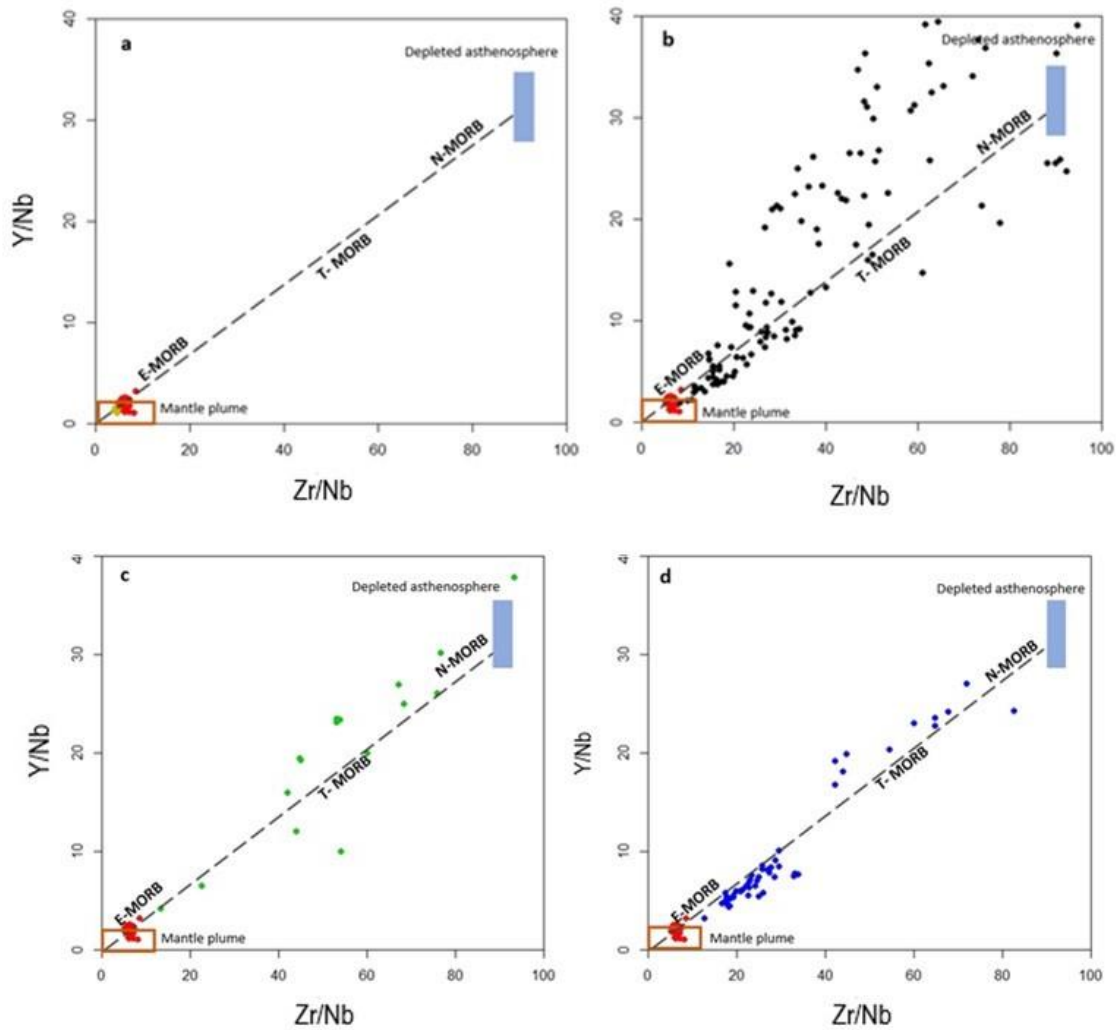


Figure 28. Y/Nb versus Zr/Nb diagram (modified after Xia and Li, 2019; Wilson, 1989), with the Bushveld data represented by the red dots. (a) Bushveld data plotted with Hawaii data in yellow; (b) Tonga in black; (c) Scotia in green; (d) Mariana in blue. T-MORB represents “Transitional Mid-Ocean

Ridge Basalt”; E-MORB represents “Enriched Mid-Ocean Ridge Basalt” and N-MORB stands for “Normal Mid-Ocean Ridge Basalt.”

The samples from Tonga (Fig. 28b) originate from different mantle parts, ranging from E-MORB to N-MORB. A significant number of samples plot within the E-MORB field close to the Bushveld data; however, only a few samples overlap with the Bushveld samples. The few samples that overlap with the Bushveld are from the islands of Fiji and Tonga, which represent basaltic rocks from the intra-oceanic arcs shown in Figure 25. The intra-oceanic arc lavas consist of basaltic andesites and basalts.

The MORB normalised spider diagrams in Chapter 4 (Fig. 17) show the generic depletion of immobile trace elements (Nb and Y) from the Bierkraal borehole data. The basaltic rocks from Tonga are relatively enriched in LILEs (Sr and Ba) and show a negative Nb anomaly, which is a geochemical signature similar to that observed in island-arc basalts. The upper mantle (N-MORB) is depleted in elements such as Sr, which is more abundant in the lower mantle (E-MORB).

Most samples from Mariana plot within the E-MORB field, with the remaining samples being intermediate between transitional (T)-MORB and N-MORB. In addition, there are no apparent overlaps between Mariana and the Bushveld. Similarly, Scotia shows no overlapping data with Bushveld data, and the Scotia samples (Fig. 28c) are distributed across all the MORB types. Although certain trace elements are unevenly distributed in this dataset (Figs 18 and 19), similarities with those of the Bushveld Complex are observed, e.g. Scotia and Mariana show enrichment in highly incompatible trace elements.

Background to identified tectonic settings

Arc-related volcanism

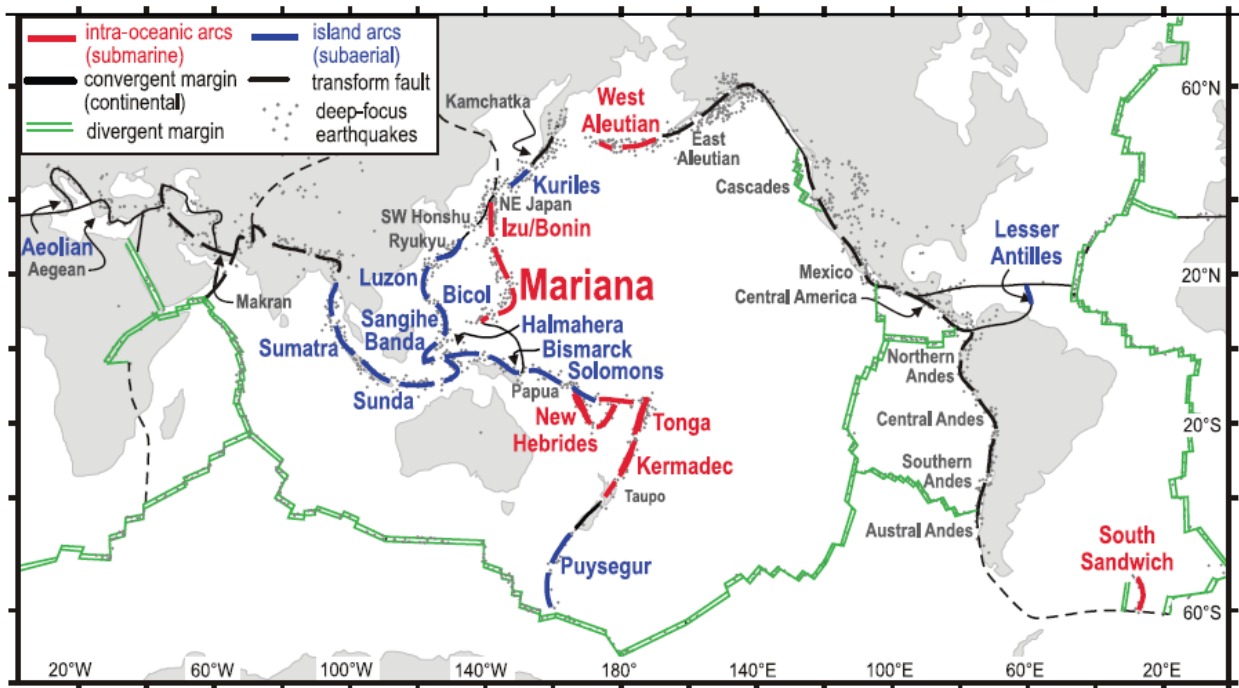


Figure 29. Locations of the most common island arcs, intra-oceanic arcs, and several plate boundaries (after De Ronde et al., 2003).

Close to 70% of volcanic activity on Earth occurs under the surface of the sea along mid-ocean ridges, where new oceanic crust forms (green lines in Fig. 29). The resulting volcanic rocks are generally basalts that usually erupt between depths of 4 000 and 2 000 m. Over the last decades, attention has been refocused on the submarine volcanic activities responsible for the formation of volcanic arcs within subduction zones (Stern, 2002). The refocus has been due to renewed interest in the mineralization products, that also indicate some of the mantle processes involved. Most island arcs, which form through continent–ocean collision, and intra-oceanic arcs, which form through ocean–ocean collision, are in the western Pacific Ocean (Fig. 29). Arc-related basalts are associated with destructive plate margins and form in areas where the oceanic lithosphere is undergoing

subduction into the mantle. Subducting oceanic lithosphere is, therefore, typical of arc-related volcanic activity, which includes island-arc, oceanic-arc, and continental-arc magmatism. The overriding plate could be continental or oceanic lithosphere, producing different geochemical characteristics. Surface volcanism, in such instances, could include both island- and intra-oceanic arcs, with the former built on the typical oceanic crust and the latter on thickened oceanic crust. The "subduction-factory", as termed by Stern (2002), describes the processing of the upper mantle and oceanic crust in a deep, broad zone within subduction zones (Stern, 2002). These factories are the primary agents responsible for recycling the oceanic crust and returning mantle material to the oceans (Fig. 30).

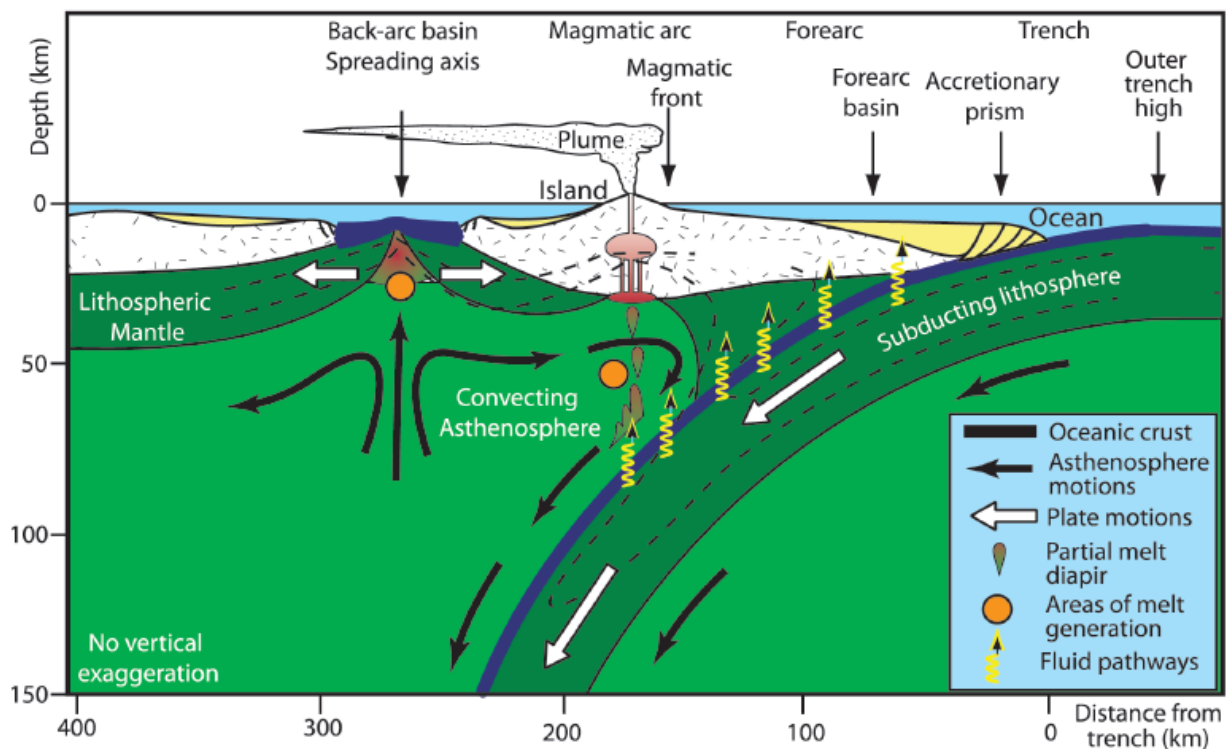


Figure 30. Cross-section through the upper 140 km in a subduction zone process, indicating several upper mantle and crustal components (after Stern, 2002).

In this section, a synopsis is presented of the tectonic and volcanic features in an intra-oceanic subduction zone. The rift zone and spreading centres in a back-arc form because of diverging plate boundaries or/and migration (seaward) of the trench (Karig, 1971). The magmatic arc is located between 100 and 250 km from the trench and above the region of melt generation (Stern, 2002). The subducting slab releases water below a depth of 100 km, which lowers the melting temperature of

the mantle, eventually causing eruption along the volcanic chains, forming the ocean floor (Stern, 2002). Approximately 75% of the submarine volcanism related to subduction zones occurs in the Kermadec–Tonga, Izu–Bonin–Mariana and New Hebrides oceanic arcs (De Ronde et al., 2001, 2003). Bird (2003) estimated that these intra-oceanic arcs comprise ~15% of the overall subduction zones on the planet. A forearc is a region where two plates interact, usually serpentine and fractured (Fig. 30). The fracturing and bending associated with a subducting plate (oceanic) cause a depression, termed trench, as shown in Figure 30.

Tonga arc

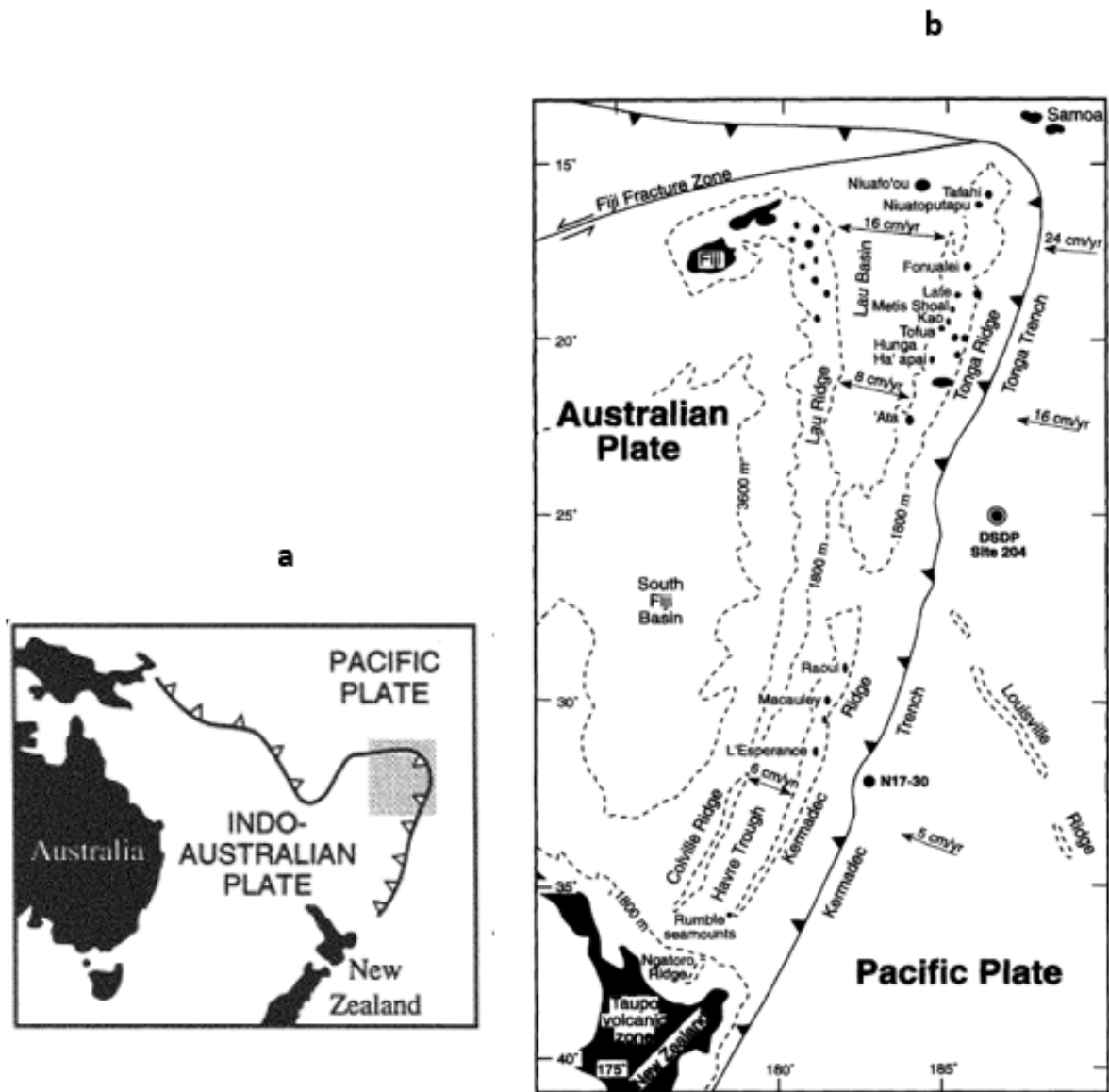


Figure 31. Maps of the Kermadec–Tonga arc system. (a) and (b) show the estimated plate motions after Hawkins (1995) and Turner et al. (1997), respectively.

The most apparent overlaps observed in the PCA between the Bushveld borehole data and Tonga data are from the Lau basin (Fig. 31b). Zellmer and Taylor (2001) described this basin as a rapidly

spreading back-arc basin located on the western segment of the Tonga arc. Several authors have attempted to explain this complex system using both major and trace element geochemistry, e.g. Pearce et al. (2007), Shaw et al. (2008), Lupton et al. (2009), Hahm et al. (2012, Lupton et al. (2012a). The Cenozoic (66.0–0.0117 Ma) Lau basin (Fig. 31b) is positioned above mantle material with strong seismicity and an underlying westward-dipping seismic region belonging to Tonga Trench subduction, with an opening rate of 1.6 cm/yr in 1995 (Hawkins, 1995). This author suggested a combination of high mantle diapir and slab rollback as the main driving force behind the crustal extension. The trapezoidal shape of the basin is interpreted as a progressive north–south opening, meaning that the orientation of the Louisville Seamount Chain constrains the apex of the basin towards the south (Hawkins, 1995).

Varying isotopic signatures were observed for the basin, ranging from Indian-type mantle (Indian Ocean) in the north to the Pacific-type mantle towards the south of the basin (Lytle et al., 2012). In addition, the same author identified a conspicuous ocean island basalt (OIB) signature in the northwestern parts of the Lau basin. A collision of the Vitiaz Trench with the Ontong Java Plateau around 10–12 Ma halted the subduction of the Pacific Plate along the northern Tonga–Solomon section of the trench. This collision led to the complex transform faults on the plate margin to the north of Fiji–Tonga, with associated rifting and spreading centres (Fig. 31b).

Hawkins (1995) suggested two styles for the tectonic opening. (1) The formation of half grabens from the initial opening, which occurred ~6 Ma, was caused by the rifting and attenuation of the forearc of the Lau Ridge. These grabens received basaltic flow simultaneous with the arc volcanism in the Lau Ridge. (2) Phase two of the tectonic opening occurred ~5.5 to 5 Ma, influenced by a southwards-moving rift system that formed a new crust through seafloor spreading (Hawkins, 1995). These events led to a second migration at ~1.5 Ma, forming an overlapping ridge. A three-limbed rift system towards the northeast part of the basin formed what Hawkins (1995) refers to as a “triple junction.” In addition, Hawkins (1995) suggested a fourth rift system towards the northwest part of the Lau basin.

Mariana arc

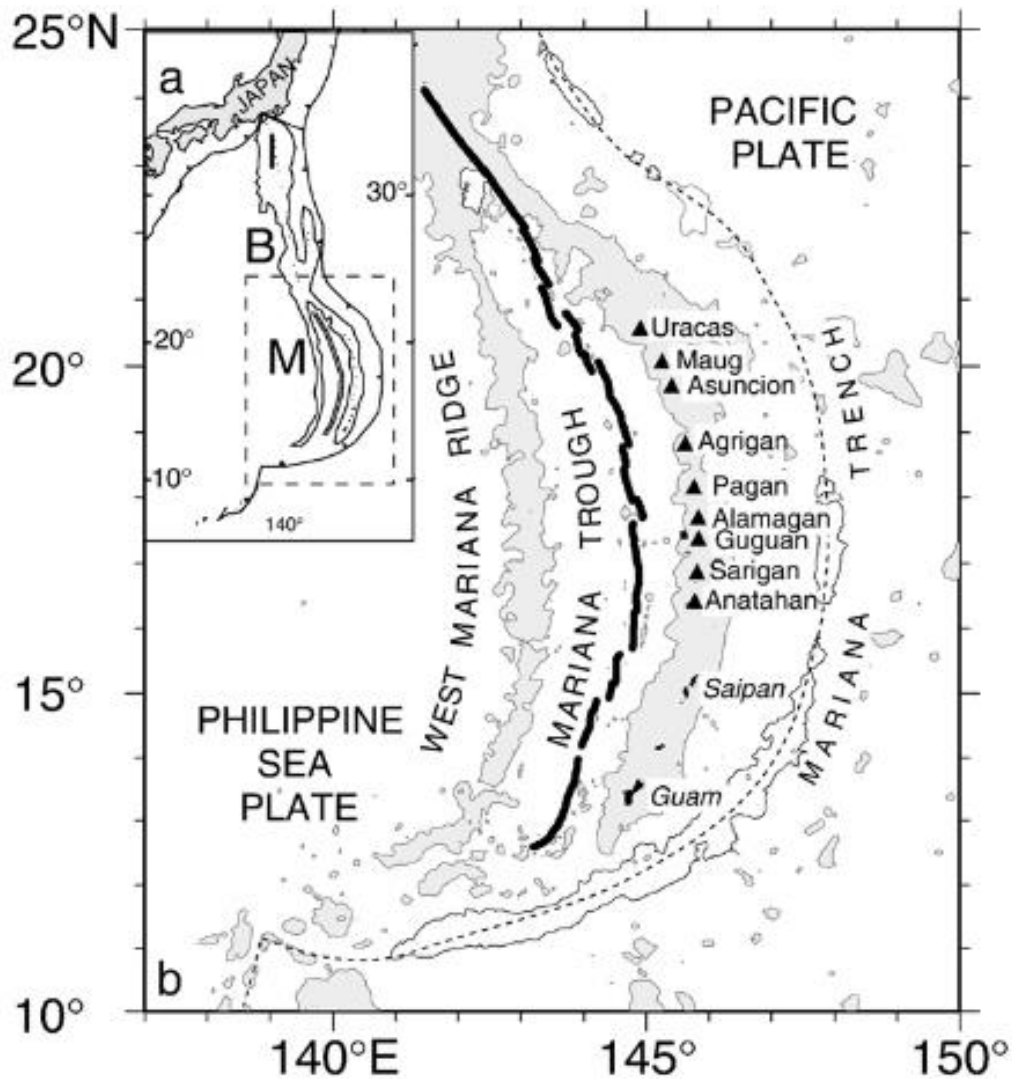


Figure 32. (a) Regional map of the Izu–Bonin–Mariana arc system; (b) tectonic setting of the Mariana arc (after Stern et al., 2003).

The Izu–Bonin–Mariana arc system (Fig. 32), which extends for 2 500 km, is part of an island arc formed on the eastern section of the Philippine Sea, where the subduction of the Pacific Plate takes place (Ishizuka et al., 2007). This subduction zone has a complex and long geological history (Stern et al., 2003). The last recorded/recent phase of subduction started with a back-arc spreading

from the Mariana trough ~ 7 Ma (Stern et al., 2003). Previous research in the area conducted by Tollstrup and Gill (2005) suggested that the magmas intruding the arc comprise various intruding components (including sedimentary and altered oceanic crust). Several authors, e.g. Plank and Langmuir (1998); Shaw et al. (2003); Plank (2005) have attempted to understand the geochemical signature and composition of the subducting crust, revealing inconsistencies along the arc. The occurrence of seamounts and oceanic islands characterise the Mariana arc, whereas Asian continental material and a lack of carbonaceous sediments form the Izu–Bonin arc. Variation in the slab composition occurs throughout the arc, with the varying angle of subduction supplementing such occurrence. All these factors contribute to the overall variation.

The magmatic arc divides into three sections, which are the Southern Seamount Province, Central Island Province, and the Northern Seamount Province. The Southern Seamount Province is situated on the western periphery of the Mariana arc and has active volcanic islands. The Central Island Province has eight island volcanoes and several seamounts. The Northern Seamount Province comprises submarine volcanism and terminates where the southern Bonin arc merges with the Mariana arc. Over 60% of the island volcanoes have a history of recent eruption, with the most recent eruption being that on Anatahan (the southernmost island). According to Trusdell et al. (2006), the first eruption of this volcano occurred in 2003. Chen et al. (2021) suggested there are more undocumented submarine eruptions in the area.

Scotia arc

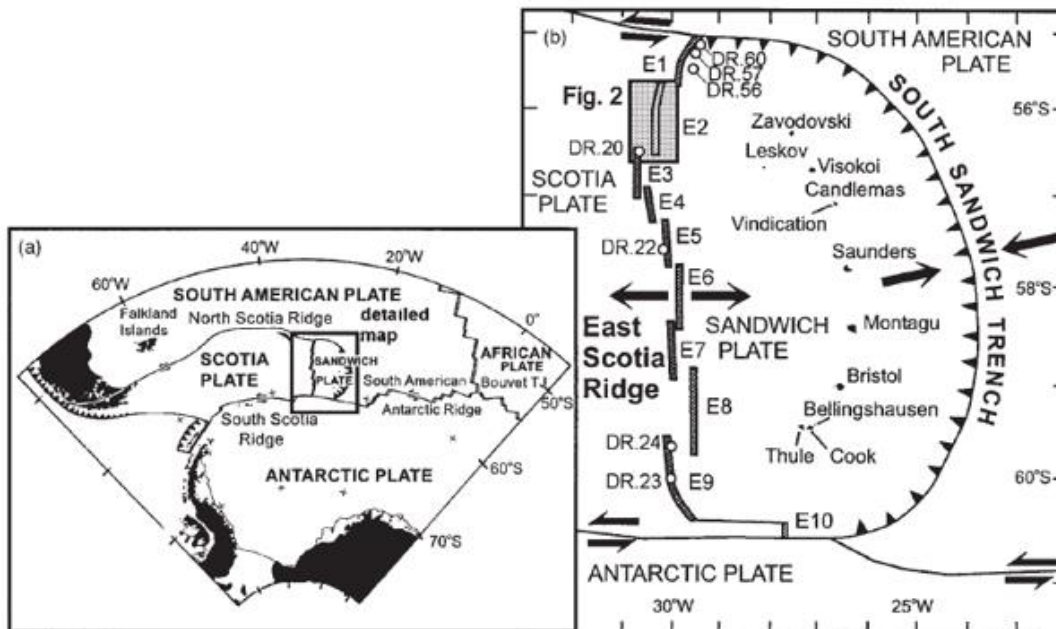


Figure 33. (a) Tectonic setting of the Scotia Ridge (east) in the Atlantic Ocean. The boxed Sandwich Plate in (a) is located between Antarctica, South America, and the Scotia Plate; (b) map showing the East Scotia Ridge and Sandwich plate. This ridge is formed from the east to west divergence of the Sandwich and Scotia plates (after Leat et al., 2000).

Three major plates are located underneath the Scotia Sea, namely the Scotia, Antarctic, and South American plates. These plates are all moving slowly at ~ 22 km/Ma, lowering the frequency of new hotspot formation in the region (Barker, 1995). The south and north sections of the Scotia Plate make up the South Scotia Ridge and North Scotia Ridge, respectively (Fig. 33). This slow-moving plate system contains a smaller Sandwich Plate that overrides the South American plate at ~ 70 – 85 km/Ma (Pelayo and Wiens, 1989). Forsyth (1975) and Brett (1977) studied the earthquakes resulting from this subduction system and postulated that the angle of subduction of the South American slab is ~ 45 – 55° west below the Sandwich Plate. The same authors suggested that the subducting South American Plate separates from the northern part of the arc in a scissor-like motion. The South Sandwich Islands formed on the South Sandwich Plate and the subduction process drives the subsequent volcanic arc. The far eastern sections of both the Scotia and Sandwich plates have an oceanic signature, with the South Sandwich Island identified as a good example of an intra-oceanic arc (Leat et al., 2000). Livermore et al. (1997) studied the East Scotia Ridge and considered it a back-arc spreading centre of

the South Sandwich Islands (Fig. 33b). Alvarez (1982) and Livermore et al. (1997) have contrasting opinions on the motion of the subducting slab, with the former suggesting that the mantle material within the vicinity is flowing eastwards, causing the slab to form a trench–arc system. The latter authors suggested that mantle material is flowing westwards from the northern end, which could indicate that the eastward motion of the Sandwich Plate is driven purely by slab rollback. Most islands in the South Sandwich area show recent volcanism. This volcanism has the oldest recorded radiometric age of ~3.1 Ma (Baker et al., 1977). The most abundant rock types found here are basalt, basaltic andesite, and dacite — ranging from tholeiitic to calc-alkaline (Baker et al., 1977). Barker (1995) regarded these islands as an example of a primitive island-arc development stage.

The ridge system (Antarctic–South America) has a slow spreading rate of ~9 km/Ma. Barker and Lawver (1988) described the system as a mid-oceanic ridge where numerous extensive faults interspace in short spreading intervals (Barker and Lawver, 1988). The eastern periphery of the ridge joins the southwest Indian and Mid-Atlantic ridges at the Bouvet Triple Junction (Fig. 33). Geochemistry, bathymetry, and ridge morphology indicate at least two mantle plumes close to the junction. (1) The Bouvet plume is located below Bouvet Island- which is located near the junction between the South American, African, and Antarctic tectonic plates, the island is mostly formed from a shield volcano—a broad, gently sloping cone formed by thin, fluid lavas—that is almost entirely covered by glaciers. At an estimated 65 km², this island locates towards the Southwest Indian Ridge (a mid-ocean ridge located along the floors of the south-west Indian Ocean and south-east Atlantic Ocean). (2) The Shona mantle plume is located below the southern Mid-Atlantic Ridge at ~52°S, where Douglass et al. (1999) sampled basalts with plume-related geochemical anomalies. The ridge shallows to a depth of 1.5 km. Kurz et al. (1998) interpreted various samples from the South American–Antarctic Ridge as indicative of a mantle plume migrating westwards towards the Sandwich Plate.

Oceanic island volcanism

In general, basaltic rocks are the main constituents of oceanic islands. These islands are a significant component of igneous petrology and contribute between 2 and 5% of all magma. They are small-scale samplers of the mantle and highlight small components of the other complex systems within the mantle.

Hawaiian islands

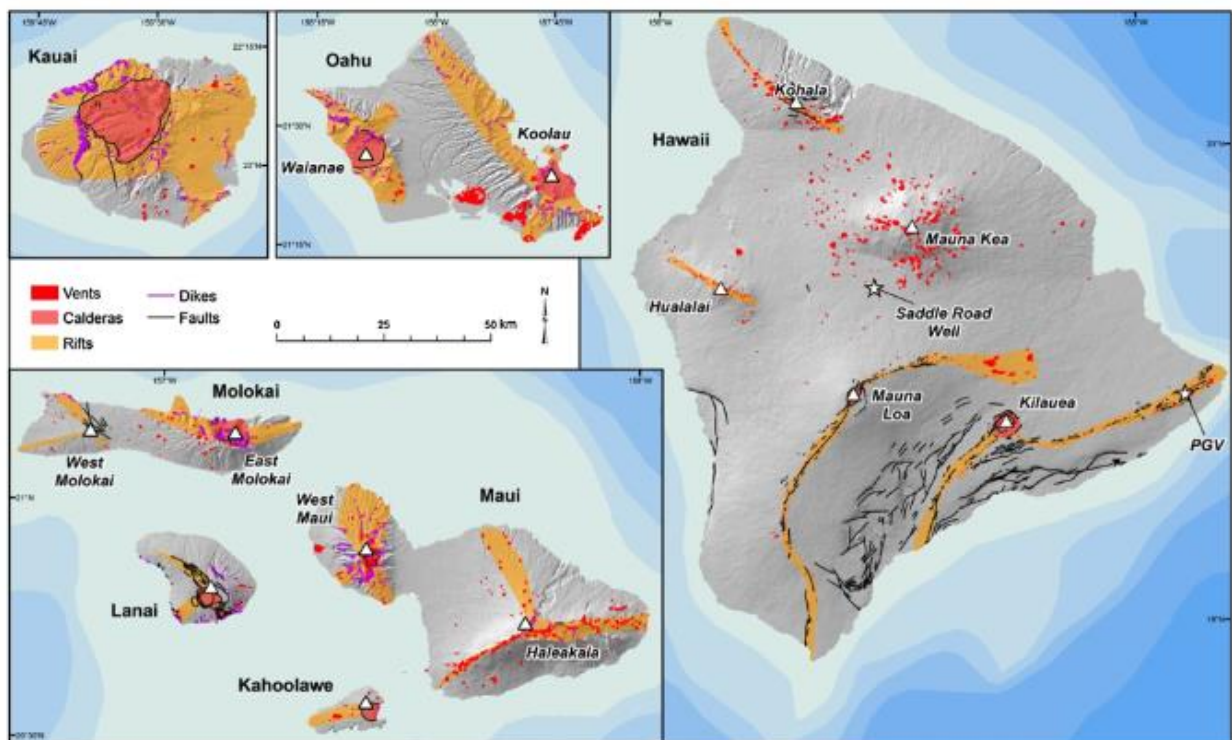


Figure 34. Islands of Hawaii. The white triangles indicate the summit of different shield volcanoes. The geological features (dike, rift, vent, caldera, and fault) are from Sherrod et al. (2007) (after Lautze et al., 2017).

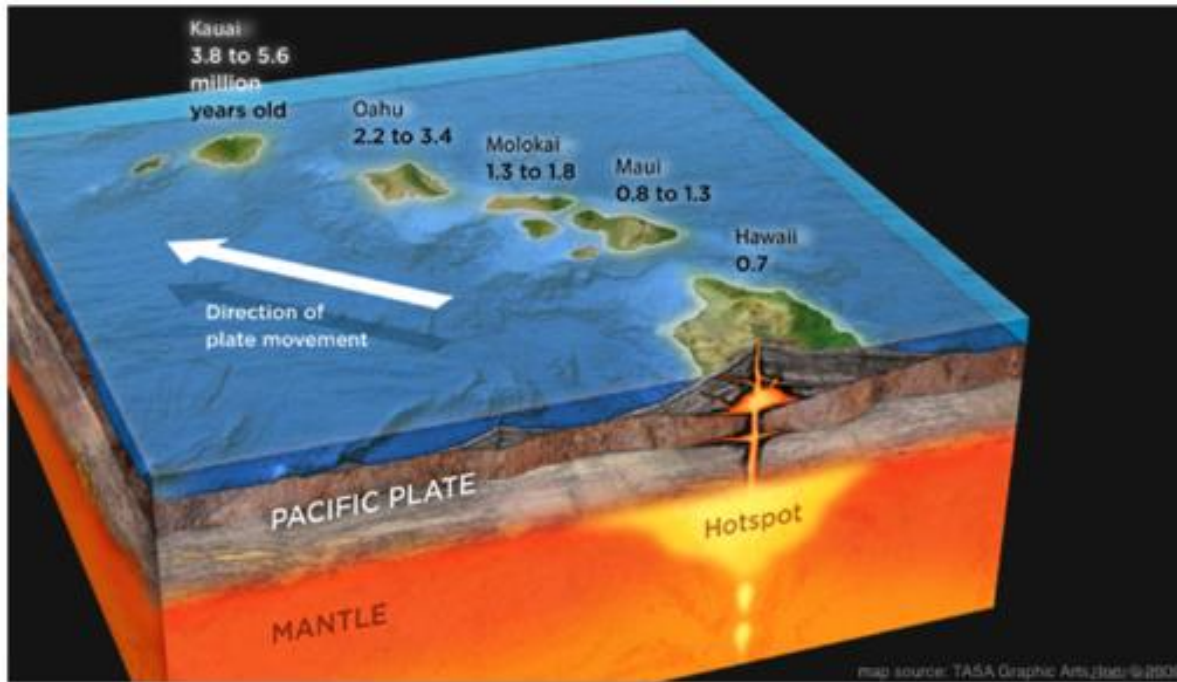


Figure 35. Map of the magma genesis for the Hawaiian islands. The respective ages of the most recognised islands indicate shield-building processes. Note that these ages decrease to the southeast (Lautze et al., 2017).

Examples of intra-oceanic volcanic activities include volcanic islands and seamounts distal to adjacent active plate boundaries within oceanic basins. These examples imply that the spreading rates of the ocean basins determine the orientation and frequency of the volcanic islands, with slow-spreading (Atlantic Ocean) rates resulting in smaller groups. In contrast, fast-spreading rates (Pacific Ocean) create linear chains (Xia and Li, 2019). The genesis of the linear volcanic chain model dates back to the 1960s (JT Wilson) and is still adopted in explaining intra-oceanic volcanism (Wilson, 1973). Such volcanism involves a stable magma source from within the mantle and a mantle plume or hotspot that underlies a moving oceanic plate. The rising hotspot or mantle plume interacts with the passing oceanic plate to facilitate the formation of a volcanic island or seamount. The motion of the oceanic plate carries the resulting volcano away from the hotspot or plume, cutting the magma supply and

ultimately the volcanism. Therefore, most geoscientists have recognised mantle plumes/hotspots as the driving force behind mid-plate volcanic activities (Kerr, 2013). However, a fascinating yet poorly explained aspect of these plumes is the ongoing volcanism at a significant distance from the ascending plume stem, even after no eruptive activity (Garcia et al., 2016). Accordingly, the seafloor spreading direction coincides with a chain of extinct volcanoes moving further away from the source and is the explanation for the formation of the islands of Hawaii. In Hawaii, shield-type volcanoes are dominant (Figs 34, 35) and they mainly produce tholeiitic basalts (Lautze et al., 2017).

Various authors have described the magmatic source (which depicts a hotspot) as the Hawaiian plume. The migration of these shield volcanoes away from the plume forms alkalic lavas, which erupt during the rejuvenation stage. Dana et al. (1980) first recognised this 'second' phase of volcanism around Hawaii. In the current study, the second phase is called 'rejuvenation'. In this context, the term rejuvenation stage refers to volcanism occurring after a prolonged period of little to no volcanic activity in areas of previous shield volcanism, which could be 0.25–2.5 Ma (Ozawa et al., 2005). This second stage of volcanism occurs in and around shield volcanoes in several oceanic islands, including Kerguelen, Samoa, and the Canary Islands (Hoernle and Schmincke, 1993). The resulting magmas/lavas have various compositions, including basanite, alkali olivine basalt, nephelinite, and melilite (Garcia et al., 1986; Clague & Dalrymple, 1987; Fekiacova et al., 2007). The subaerial volcanism has drawn similarities with submarine lavas from the seafloor surrounding the Hawaiian islands (periphery), as mentioned by Lipman et al. (1989) and Frey et al. (2000). Some suggestions are that alkali lavas form through partial melt generated from decompression and lithospheric uplift. The rejuvenated stage volcanism (which is volcanism occurring after a prolonged period of no volcanic activity) occurs above the flexural arc at a distance of ~200 km from the axis centre (Garcia et al., 2016). Over the years, the flexural arc has experienced distinct volcanic activity because the area is 200 km from the hotspot axis with prior volcanism (Frey et al., 2000).

Implications of the results for the potential tectonic environment

The plate tectonic theory postulates that mid-oceanic ridges form at divergent plate boundaries (Fig. 30). At divergent plate boundaries, tectonic plates move away from each other, creating a gap where new oceanic crust is formed (Xia and Li, 2019). In such boundaries, new oceanic lithosphere (mantle ± crust) forms because of the partial melting of the mantle lherzolite (Xia and Li, 2019). Therefore, adiabatic decompression occurs within the narrow zones where magma is upwelling. This process explains how basaltic magma forms and its injection through tensional discontinuities into thin zones located at the ridge axis. The vast amount of magma solidifies within

layered intrusions and dykes, but sometimes erupts on the surface as pillow lavas. However, newly formed basaltic rocks are transported away from the axis through continued seafloor spreading (Wilson, 1989). Generally, MORBs have the following properties (1) most are tholeiitic, apart from a few that form part of the alkaline series; (2) depletion of incompatible elements in N-MORB generally reflects depletions within the source; (3) E-MORB shows a distinct pattern enriched in most incompatible elements, such as OIBs.

A number of samples from the Bierkraal area (BK1) in Figure 1 show a continental-arc geochemical signature, which could reflect magmatic contamination through mixing and assimilation with the continental crust. This process could result from newly formed magma melting pre-existing continental crust at shallower levels. Various authors (Wilson, 1989; Wang and Glover, 1992) noted that several continental basalts exhibit mixed geochemical identities, e.g. showing subduction-related and intraplate volcanic characteristics. Lee et al. (2007) suggested that upwelling magma migrates through a broader stratum saturated in pyroxene and garnet, whereas magma migrating through thinner terranes crystallises olivine-rich units. The transition of the samples in Bierkraal consists of continental arc signatures intertwined with MORB signatures. With the possibility of contamination already explained by Wilson (1989), questions remain on the type of crustal contaminant.

In contrast, the geochemical signatures of an oceanic arc reflect magma with little or no influence from the continental crust. Note that an extension of mid-oceanic ridges through most major oceanic basins has an estimated total length of over 60 000 km (Xia and Li, 2019). Figure 26 shows samples in different mid-oceanic ridge environments and within-plate basalts and tholeiites. Most samples from Bierkraal show an E-MORB geochemical signature similar to that identified for Hawaii. The Y/Nb versus Zr/Nb diagram in Figure 28a overlaps the Bierkraal data and Hawaii data. The data plot is in an E-MORB field representing primitive mantle material. The oceanic islands of Hawaii formed from mantle plumes, i.e. small-scale samplers of the fertile mantle. In other words, the magma originated from the mantle sources. The magma originates from melting hot mantle material within the plume.

Table 3. *Growth stages, approximate age, and rock types of Niihau and Kaula (after Cousens and Clague, 2015).*

	Niihau	Kaula
Shield stage		
Age range (Ma)	5,8 - 4,3	5,6 - 5,4
Rock types	tholeiitic basalt	tholeiitic basalt
Post-shield stage		
Age range (Ma)	N/A	5,4 - 4,8
Rock types		transitional basalt
Rejuvenated stage		
Age range (Ma)	3,7 - 0,15	2,3 - 0,3
Rock types	alkalic basalt, basanite	alkalic basalt

This interpretation that Hawaii formed from mantle plumes could well align with the magmatic plume model suggested by Hatton and Schweitzer (1995) for the formation of the Bushveld Complex, as the distinguishing features observable in the complex are consistent with the magmatic plume model. For example, Sharpe et al. (1981) identified a radial distribution of satellite bodies and intrusive centres. Elevated Sr, Ba, and Nb concentrations complement this distribution, potentially indicating crustal influence (Kruger and Marsh, 1982; Sharpe & Hulbert, 1985). This interpretation ties in with the high Mg, V, Ti, and Fe concentrations observed in the Upper zone. One possible avenue for explaining the Upper Zone's geochemical signature could include the Archaean crust's melting.

Apatite rare earth element data from Magnetite Layer 21

This study included an analysis of REEs of the top 625 m of the Upper Zone in the eastern Bushveld Complex. Apatite, the mineral in focus, is unique as it is the only identified mineral capable of hosting REEs (Cawthorn, 2013). Recent data have indicated significantly distinct REE contents from the apatite in multiple superimposed segments of the Upper Zone. Van Tongeren and Mathez (2012) identified these data as evidence for large-scale immiscibility towards the complex boundary. Cawthorn (2013) re-interpreted the data as a by-product of the trapped liquid shift effect.

Among the identified tectonic settings, no samples display a pattern similar to that observed from the upper 325 m apatite population of the Bushveld Complex. Van Tongeren and Mathez (2012) described this population as having three times the concentration of REEs in the underlying

population, with a negative Eu anomaly. In contrast, similarities exist between the underlying 300 m apatite population and some settings indicated in this study. The lower 300 m population consists of multiple magnetite gabbroic and plagioclase-magnetite-ilmenite cumulate layers. These rocks contain cumulus apatite and comparatively low REE content, with little to no Eu anomalies (Van Tongeren and Mathez, 2012). Therefore, most spider diagrams (Figs 21–24) show pertinent similarities between the tectonic settings (e.g. Tonga, Mariana, and Hawaii) and the Bushveld apatite data. There are no clear and straightforward similarities between Tonga and the Bushveld Complex, with the closest signatures being observed in the Tonga and Fiji islands (Fig. 21b, e). Mariana (Fig. 23) has an REE pattern similar to that observed in Scotia. This finding implied that the patterns show depletion of LREE and HREE compared with those of the Bushveld Complex. Outside of the Bushveld data, Hawaii (Fig. 24) has the highest overall enrichment of REEs.

Although Figure 22 generally shows a flat REE pattern for Scotia, the East Scotia Ridge (Fig. 22d in this study) is arguably unique, as its REE pattern is similar to that observed from the lower 300 m of the Bushveld Complex. In the recent past, structural investigations of coeval intrusions in the Bushveld Complex led some authors (Olsson et al., 2011) to argue that the magma forming the Bushveld Complex originated from a back-arc setting that relates to the Magondi and Limpopo orogenic belts (Olsson et al., 2011). Calc alkaline compositions, boninitic affinities observed in the Marginal Zone (Bushveld Complex), and the high Cl/F ratios in the Main and Critical zones form the basis of this argument (Olsson et al., 2010). Despite all this evidence, the high $\delta^{18}\text{O}$ recorded in the RLS contradicts a subduction-related setting. The oxygen isotope composition of a region can provide valuable insights into its tectonic setting (Cavosie et al., 2005). High ^{18}O values are generally not expected in subduction-related environments where one tectonic plate is subducting beneath another (Ellam and Harmon, 1990; Cavosie et al., 2005). This is because the subducting plate is often made up of oceanic crust and sediments, which have lower ^{18}O levels due to their origin in seawater (Ellam and Harmon, 1990; Cavosie et al., 2005). Due to data availability, the East Scotia Ridge samples were limited to two.

East Scotia Ridge

As shown in Figure 21d, the samples were normalised to MORB (after Gale et al., 2013). These samples derive from East Scotia Ridge segment E2 (Fig. 33b) – dredge 157. This segment is located in the back arc of the East Scotia Ridge, with an axial high typical of oceanic ridges that have been subjected to fast-spreading ridges, possibly indicating inflated segments (Leat et al., 2000). These authors described this segment as inflated through excessive generation of magma. Livermore et al. (1997) initially suggested that various partially melted mantle materials underlie this segment compared with the rest of the ridge, with several postulations based on seismic, bathymetric, sonar, and side-scan data. As regards dimensions, this segment forms a 70 km extension towards the southern E3 segment (Fig. 33b) (Livermore et al., 1997). The depth of the segment increases from 2.6 km at the summit to 3.5 km at the tip of the segment. Below a depth of 3.1 km, at the edge of the central part of this segment, there is an area of favourable topography formed by constructive volcanic structures (Leat et al., 2000). Livermore et al. (1997) referred to this structure as the “Mermaid’s Purse”. The structure measures 0.6 km high and 2 km wide (north–south), with a graben on its summit. Seismic data from Livermore et al. (1997) identified a melt lens positioned below the Mermaid’s Purse, which is less than 1 km thick east–west, 3 km deep, 20 km long, and comparatively similar to that identified by Collier and Sinha (1990) beneath the Lau basin back-arc setting. The Mermaid’s Purse and the melt lens, combined with the lack of a rift valley, indicate a potentially fast-spreading mid-oceanic centre (Batiza et al., 1996).

Geochemical overlaps and discrepancies

Overall, the geochemical data from the Bierkraal boreholes in the western limb and the apatite REE data from the eastern limb (Upper Zone) of the Bushveld Complex are crucial for narrowing down potential tectonic settings that exhibit similar signatures. The Bierkraal borehole data indicate six trace elements (Rb, Ba, Nb, Sr, Zr, Y) for plotting the spider diagrams (after Gale et al., 2013). Nevertheless, the location most synonymous with Bushveld data appears to be that of the Hawaiian islands of Kaula and Nihau. Hawaii also exhibits more depletions in elements such as Nb and Y compared with the Bushveld.

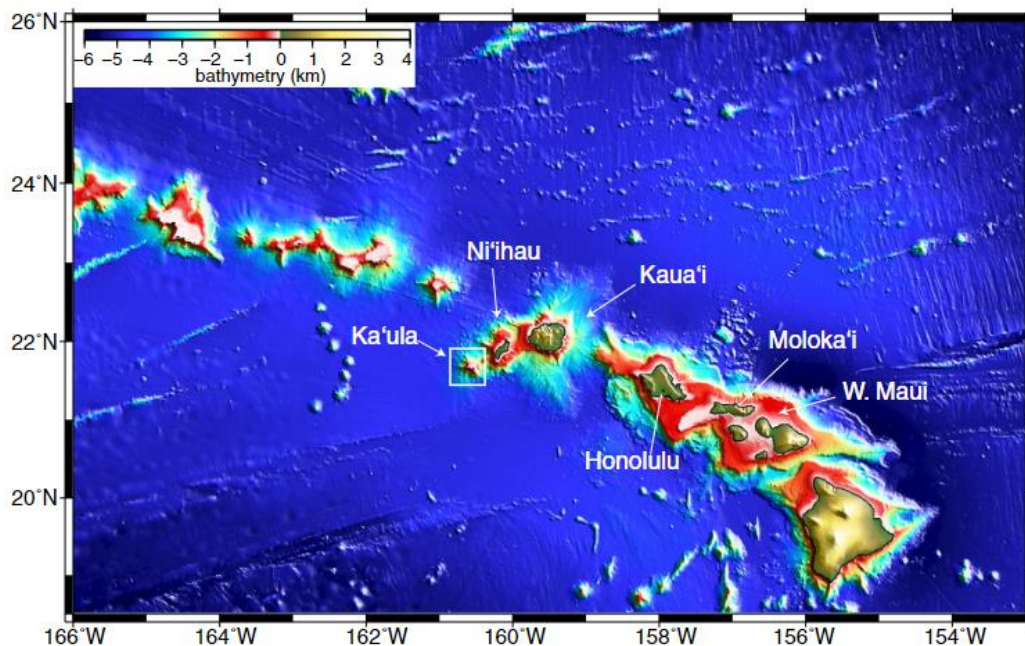


Figure 36. Bathymetry map showing the locations of the two samples in Hawaii, namely Kaula and Niihau (after Garcia et al., 2016).

Samples from the Bushveld and Hawaii (Fig. 20) show relative enrichment in Sr, Ba, and Rb, which are fluid-mobile LILEs. These incompatible trace elements possibly migrated with the magma from the mantle in an island-arc system. Island arcs are generally interpreted as a calc-alkaline system comprising andesite, basalt, dacite and rhyolite (Gill, 1970). To a certain extent, the islands of Fiji and Tonga also show overlaps with the Bierkraal trace element data.

The whole rock trace element data (Bierkraal) in figures 17 a, e, f, and h show similarities with the Tonga islands, Lau basin spreading centre, and Fiji Islands, respectively. It is generally accepted that mixing of Indian- and Pacific-type mantle material occurs in the north section of the Lau basin, with an accompanying enigmatic OIB signature (Tian et al., 2011). The lateral flow mantle material (termed Samoan hotspot) in the Lau basin potentially follows the western movements of the Pacific Plate (7 cm/yr, as mentioned by Koppers et al. (2011). The mantle plume material becomes entrained in the basin through toroidal magmatic flow along the edges of the Pacific Plate (Schellart, 2004; Schellart et al., 2007). As such, the similarities imply that the Upper Zone has a geochemical signature

that can be related to subduction-arc settings. The geochemical trace element signatures of these subduction-arc settings possibly involve an enriched MORB source.

On the other hand, the REE data show a more general overlap with the identified tectonic settings. The most similar geochemical signature is between the lower 300 m segment of the Upper Zone, characterised by multiple layers of magnetite, and the East Scotia Ridge (a divergent plate environment associated with a back-arc basin). This interpretation could well support the model by Hatton (1998), who suggested that the Bushveld Complex formed as a product of subducting plate margins located at the edge of the Kaapvaal Craton. However, reservations could well be placed on this interpretation due to the limitations incurred from the low number of samples in this study, as well as the high $\delta^{18}\text{O}$ recorded in the RLS.

E-MORB source vs Archaean crustal input

Overall, the geochemical signatures from both the trace element and apatite data, range between E-MORB and OIB. Theoretically, these signatures are indicative of an enriched mantle source. Practically, an enriched geochemical signature can be derived from different magmatic processes. As such, different mantle processes can be possible for the assimilation and upwelling of the magmatic fluids to form the Bushveld Complex. Note that the Bushveld Complex was formed in an open system, where different variables (identified and unidentified) had a significant influence. In this study, emphasis was placed on the tectonic environment in which the magma originated. In this study, the geochemistry of basaltic rocks is considered a predictive indicator in determining the likely tectonic setting in which the parental magma originated. As such, an E-MORB source, in the context of the Bushveld, would require a prolonged volcanic event, where magma migrates in large volumes. Considering that the Kaapvaal craton stabilized (~ 2.7 Ga) long before the formation of Bushveld Complex (2.06 Ga), the Bushveld Complex formed in a relatively short period of time, estimated at ~ 100 Ka by Cawthorn and Walraven (1998).

Several types of subcontinental lithosphere (including Archaean and Phanerozoic) formed during the earth's history. Arndt et al. (2009) suggests that the subcontinental lithosphere is made up of residues of different mantle plumes. The Kaapvaal craton, one of the best-preserved Archaean cratons, hosts some of the oldest recorded rocks globally. De Wit et al. (1992) identify multiple plume related volcanism across different parts of the Kaapvaal craton. This study is based on the idea that the RLS and subsequent Upper Zone, formed from multiple pulses of plagioclase-bearing magma, deposited on the discontinuities as sills. During magmatic upwelling in this open system, crustal

contamination probably occurred. Although the contamination process is not finely detailed, this study suggests that at some stage in the upwelling process, the magma possibly interacted with the Archaean crust, giving the magma a relatively primitive geochemical signature (Pearce, 2008). Historically, the Archaean crust is rich in Fe and Mg, which can be found in olivine-rich rocks. Geochemically, the signature of Archean basalts can range between OIB and MORB (Arndt et al., 2009).

CHAPTER 6 - SUMMARY AND CONCLUSIONS

Evaluation and understanding of layered intrusions could provide crucial information for comprehending the dynamism of different magmatic processes combined with the emplacement of magma in different tectonic environments. This study focuses on the UUMZ of the Bushveld Complex, specifically the Bierkraal borehole data (western limb) and complementary apatite REE data (eastern limb). The complex generally shows a wide range of magmas, ranging from Fe-rich (more primitive) to Si-rich (evolved), formed from varying geological processes. Preliminary results from the western limb showed a general depletion of K and Zr. The general assumption in this study is that these trace elements were incorporated into water molecules, leading to their overall deficit. The study aims to correlate this postulation with MORB. Assuming that the source of the UUMZ magma is directly proportional to the tectonic environment, one of the objectives of this study was to understand the genesis and origin of the parental magma. A multidisciplinary approach was followed, i.e. employing a combination of geostatistics and programming elements to analyse the database. As a result, different models of the magma genesis for forming the Bushveld Complex were tested.

In the approach followed, the available trace element data from the western limb guide built a basaltic-based database of rock samples from different tectonic settings – including convergent plate margin, oceanic island, submarine ridge, and oceanic plateau. A PCA analysis was conducted of the database through various software such as GCDkit, R, and ioGAS™. This analysis formed part of a multivariate statistical approach that generated a probability distribution for the selected trace elements. This approach created correlated variables and linear functions from the available trace element array. The findings of this study propose that the UUMZ originated from a solitary magma chamber that obtained its molten material from a specific tectonic environment. The results of the PCA showed clear differentiation between the data from known tectonic settings and that of the UUMZ. The data shown in Figure 14 is plotted in different locations with little to no overlaps. The UUMZ shows overlap with Tonga, Mariana, Scotia, and, less so, Hawaii. Following these results, a series of discriminant diagrams (Chapter 5) shows further analyses for geochemical similarities and discrepancies between the UUMZ and the identified locations. Notably, three of the identified overlaps (Tonga, Mariana, and Scotia) represent subduction-zone–arc-related settings, whereas Hawaii is an example of an oceanic island. Historically, all these settings represent parts of the upper mantle with relatively primitive geochemical signatures.

Most rock samples (ca 95%) are classified as oceanic-arc type based on a volcanic discriminant diagram (after Pearce, 1983). Six settings showed a continental-arc geochemical signature, with four

representing the UUMZ. The remaining two samples are from the Tonga/Fiji Islands and the South Shetland Islands (Scotia). As shown in a ternary discriminant diagram (Fig. 26), after Meschede (1986), the Bushveld trace element data are interpreted as by-products, primarily E-MORB and within-plate tectonic boundaries. A third discriminant diagram of Y/Nb versus Zr/Nb (after Xia and Li, 2019; Wilson, 1989) indicates Bushveld data as classified under E-MORB. In addition, the diagram shows an overlap between the data of the Bushveld and those of the Hawaiian islands of Nihau and Kaula. John T Wilson, a renowned geophysicist and geologist, developed a model for forming linear volcanic chains in the 1960s. This model involves a stable magmatic source from within the mantle, a mantle plume/hotspot, and an underlying mobile oceanic plate. A rising hotspot or mantle plume interacts with the passing oceanic plate to facilitate the formation of volcanic islands. In the current study, apatite REE data from the top 625 m of the Upper Zone in the eastern Bushveld Complex complement the Bierkraal data. The PCA conducted in this study excluded the apatite REE data. Van Tongeren and Mathez (2012) showed two distinct REE apatite populations, one in the top 325 m and the other in the lower 300 m of the stratigraphy. Regardless, similarities between the identified settings and the lower 300 m population were evident. Regarding the similarities, the most apparent and identical geochemical signature is between the Bushveld and the East Scotia Ridge. This ridge represents a fast-spreading back-arc basin setting (Leat et al., 2000).

In conclusion, the two datasets (trace element and REE) represent different formation and emplacement environments. As a result, this limits the range of geological processes the study investigated during magmatic genesis. The Bierkraal borehole data show a geological signature synonymous with that of oceanic islands. Although highly unlikely in the Bushveld context, this interpretation could well align with the magmatic plume model Hatton and Schweitzer (1995) suggested to form the complex. Although distinguishing features observable in the complex are consistent with the magmatic plume model, the volume of magma that erupted to form the entire Bushveld Complex cannot be generated solely by heat generated from a magmatic plume at great depth without extending parts of the lithosphere. Sharpe et al. (1981) identified a radial distribution of satellite bodies and intrusive centres. Elevated Sr, Ba, and Nb concentrations complement this distribution, potentially indicating some crustal influence (Kruger and Marsh, 1982; Sharpe & Hulbert,

1985; Auret et al., 1989). This model could be explained by the melting of Archaean crust at depth. The geochemical signatures observed from the trace element data vary between an E-MORB and an OIB source. These signatures are synonymous with those observed in Archaean basaltic rocks.

In contrast, the apatite REE data showed a geochemical signature synonymous with a back-arc basin setting. This tectonic setting could explain the depletion in K and Zr through water stripping in a subduction zone environment. This interpretation could well support the model by Hatton (1998), suggesting that the Bushveld Complex formed as a product of subducting plate margins located at the edge of the Kaapvaal Craton. Notwithstanding, a subduction zone setting in the context of the Bushveld Complex could be possible; however, there appears to be a deficiency in geological data and evidence. Despite the deficiency and inconclusive data, high $\delta^{18}\text{O}$ recorded in the RLS contradict the subduction zone model to some reasonable extent. The REE and trace element data inconsistencies could well indicate the problems associated with petrogenesis in open geological systems. Therefore, more trace element and REE data must be collected on the Upper Zone and upper Main Zone of the Bushveld Complex, which should be analysed to improve understanding.

References

2015. *Visualisation, 3D Modelling and Spatial Analysis of the Rustenburg Layered Suite, Bushveld Igneous Complex, South Africa*. University of Pretoria.

2015. *A mineralogical and geochemical review of Cycles V and VI of the Upper Zone of the Bushveld Complex*.

Alvarez, W., 1982. Geological evidence for the geographical pattern of mantle return flow and the driving mechanism of plate tectonics. *Journal of Geophysical Research: Solid Earth*, 87(B8), pp. 6697-6710.

Armstrong, R.A., Compston, W., Retief, E.A., Williams, I.T., and Welke, H.J., 1991. Zircon ion microprobe studies bearing on the age and evolution of the Witwatersrand triad. *Precambrian Research*, 53(3-4), pp. 243-266.

Arndt, N.T., Coltice, N., Helmstaedt, H. and Gregoire, M., 2009. Origin of Archean subcontinental lithospheric mantle: Some petrological constraints. *Lithos*, 109(1-2), pp.61-71.

Baker, P.E., Buckley, F. and Rex, D.C., 1977. Cenozoic volcanism in the Antarctic. *Philosophical Transactions of the Royal Society of London. B, Biological Sciences*, 279(963), pp.131-142.

Barker, P.F., 1995. Tectonic framework of the east Scotia Sea. *Back arc Basins*, pp.281-314.

Barker, P.F. and Lawver, L.A., 1988. South American-Antarctic plate motion over the past 50 Myr, and the evolution of the South American-Antarctic Ridge. *Geophysical Journal International*, 94(3), pp. 377-386.

Barker, P.F., 1995. Tectonic framework of the east Scotia Sea. *Back arc Basins*, pp. 281-314.

Barnes, S. and Maier, W., 2002. Platinum-group elements and microstructures of Normal Merensky Reef from Impala Platinum Mines, Bushveld Complex. *Journal of Petrology*, 43(1), pp. 103-128.

Batiza, R., Niu, Y., Karsten, J.L., Boger, W., Potts, E., Norby, L. and Butler, R., 1996. Steady and non-steady state magma chambers below the East Pacific Rise. *Geophysical Research Letters*, 23(3), pp. 221-224.

Bhattacharjee, C. and Mondal, S.K., 2021. Geochemistry of Fe-Ti oxide and sulfide minerals in gabbroic rocks and magnetite of the Archean Mayurbhanj mafic complex (eastern India): magma fractionation, thermometry and oxygen fugacity of re-equilibration, and implications for Ni-Cu mineralization. *Ore Geology Reviews*, 131, p.104005.

Bird, P., 2003. An updated digital model of plate boundaries. *Geochemistry, Geophysics, Geosystems*, 4(3).

Brett, C.P., 1977. Seismicity of the South Sandwich Islands region. *Geophysical Journal International*, 51(2), pp.453-464.

Bristow, C.S. and Best, J.L., 1993. Braided rivers: perspectives and problems. *Geological society, London, special publications*, 75(1), pp.1-11.

Bryan, S. and Ernst, R., 2008. Revised definition of large igneous provinces (LIPs). *Earth-Science Reviews*, 86(1-4), pp. 175-202.

Buchanan, D.L., Nolan, J., Suddaby, P., Rouse, J.E., Viljoen, M.J. and Davenport, J.W.J., 1981. The genesis of sulfide mineralization in a portion of the Potgietersrus Limb of the Bushveld Complex. *Economic Geology*, 76(3), pp.568-579.

Buick, I.S., Maas, R. and Gibson, R., 2001. Precise U–Pb titanite age constraints on the emplacement of the Bushveld Complex, South Africa. *Journal of the Geological Society*, 158(1), pp. 3-6.

Bumby, A.J., Eriksson, P.G. and Van der Merwe, R., 1998. Compressive deformation in the floor rocks to the Bushveld Complex (South Africa): Evidence from the Rustenburg Fault Zone. *Journal of African Earth Sciences*, 27(3-4), pp. 307-330.

Button, A., Pretorius, D.A., Jansen, H., Stockmeyer, V., Hunter, D.R., Wilson, J.F., Wilson, A.H., Vermal, C.F., Lee, C.A. and Stegman, J.G., 1981. The cratonic environment. In *Developments in Precambrian Geology* (Vol. 2, pp. 501-639). Elsevier.

Cameron, E.N. and Desborough, G.A., 1964. Origin of certain magnetite-bearing pegmatites in the eastern part of the Bushveld Complex, South Africa. *Economic Geology*, 59(2), pp.197-225.

Cavosie, A.J., Valley, J.W. and Wilde, S.A., 2005. Magmatic $\delta^{18}\text{O}$ in 4400–3900 Ma detrital zircons: A record of the alteration and recycling of crust in the Early Archean. *Earth and Planetary Science Letters*, 235(3-4), pp.663-681.

Cawthorn, R.G., 2015. The Bushveld Complex, South Africa. In *Layered intrusions* (pp. 517-587). Springer, Dordrecht.

Cawthorn, D.M., Steinman, H.A. and Hoffman, L.C., 2013. A high incidence of species substitution and mislabelling detected in meat products sold in South Africa. *Food control*, 32(2), pp.440-449.

Cawthorn, R.G., Lee, C.A., Schouwstra, R.P. and Mellowship, P., 2002. Relationship between PGE and PGM in the Bushveld Complex. *The Canadian Mineralogist*, 40(2), pp. 311-328.

Cawthorn, R. and Walraven, F., 1998. Emplacement and crystallization time for the Bushveld Complex. *Journal of Petrology*, 39(9), pp. 1669-1687.

Cawthorn, R.G., Meyer, P.S., and Kruger, F.J., 1991. Major addition of magma at the Pyroxenite Marker in the western Bushveld Complex, South Africa. *Journal of Petrology*, 32(4), pp. 739-763.

Cawthorn, R.G. and McCarthy, T.S., 1985. Incompatible trace element behaviour in the Bushveld Complex. *Economic Geology*, 80(4), pp. 1016-1026.

Chen, S., Wang, Z., Gao, R. and Zhou, Y., 2023. Mantle sources of Cenozoic volcanoes around the South China Sea revealed by geochemical and isotopic data using the principal component analysis. *Journal of Oceanology and Limnology*, pp.1-13.

Cheney, E.S. and Twist, D., 1991. The conformable emplacement of the Bushveld mafic rocks along a regional unconformity in the Transvaal succession of South Africa. *Precambrian Research*, 52(1-2), pp.115-132.

Chaumba, J.B., 2022. A review of the emplacement and formation of magmatic platinum-group elements-enriched deposits in large layered mafic/ultramafic intrusions, with special reference

to the “big three”(Stillwater Complex, Great Dyke, and Bushveld Complex). *Journal of African Earth Sciences*, 194, p.104603.

Clague, D.A. and Dalrymple, G.B., 1987. The Hawaiian-Emperor volcanic chain, Part 1, geologic evolution.

Coertze, F.J., 1970. The geology of the western part of the Bushveld Igneous Complex. *Geol. Soc. South Africa, Spec. Pub*, 1, pp. 5-22.

Collier, J. and Sinha, M., 1990. Seismic images of a magma chamber beneath the Lau Basin back-arc spreading centre. *Nature*, 346(6285), pp. 646-648.

Condie, K. and Wronkiewicz, D., 1990. The Cr/Th ratio in Precambrian pelites from the Kaapvaal Craton as an index of craton evolution. *Earth and Planetary Science Letters*, 97(3-4), pp. 256-267.

Cousens, B.L. and Clague, D.A., 2015. Shield to rejuvenated stage volcanism on Kauai and Niihau, Hawaiian Islands. *Journal of Petrology*, 56(8), pp. 1547-1584.

Cousins, C.A., Feringa, G., and Haughton, S.H., 1964. The chromite deposits of the western belt of the Bushveld Complex. *The geology of some ore deposits in Southern Africa*, 2, pp. 183-202.

Coward, N. and Cronan, D.S., 1987. A geostatistical evaluation of geochemical data in regard to bedrock and placer mineral exploration in the SW Pacific. *Marine Mining*, 6(3), pp. 205-221.

Dana, G.P., Smith, J.W. and Trudell, L.G., 1980. shallow oil shale deposits of southern Uinta Basin, Utah. *AAPG Bulletin*, 64(5), pp. 696-696.

De Ronde, C., Faure, K., Bray, C., Chappell, D. and Wright, I., 2003. Hydrothermal fluids associated with seafloor mineralization at two southern Kermadec arc volcanoes, offshore New Zealand. *Mineralium Deposita*, 38(2), pp. 217-233.

De Ronde, C.E. and De Wit, M.J., 1994. Tectonic history of the Barberton greenstone belt, South Africa: 490 million years of Archaean crustal evolution. *Tectonics*, 13(4), pp. 983-1005.

De Ronde, C.E., Baker, E.T., Massoth, G.J., Lupton, J.E., Wright, I.C., Feely, R.A. and Greene, R.R., 2001. Intra-oceanic subduction-related hydrothermal venting, Kermadec volcanic arc, New Zealand. *Earth and Planetary Science Letters*, 193(3-4), pp. 359-369.

De Ronde, C.E., Faure, K., Bray, C.J., Chappell, D.A., and Wright, I.C., 2003. Hydrothermal fluids associated with seafloor mineralization at two southern Kermadec arc volcanoes, offshore New Zealand. *Mineralium Deposita*, 38(2), pp. 217-233.

De Wit, M.J., de Ronde, C.E., Tredoux, M., Roering, C., Hart, R.J., Armstrong, R.A., Green, R.W., Peberdy, E. and Hart, R.A., 1992. Formation of an Archaean continent. *Nature*, 357(6379), pp.553-562.

De Wit, M. and Tinker, J., 2004. Crustal structures across the central Kaapvaal craton from deep-seismic reflection data. *South African Journal of Geology*, 107(1-2), pp. 185-206.

Douglass, J., Schilling, J.G. and Fontignie, D., 1999. Plume-ridge interactions of the Discovery and Shona mantle plumes with the southern Mid-Atlantic Ridge (40°–55° S). *Journal of Geophysical Research: Solid Earth*, 104(B2), pp. 2941-2962.

Garcia, M.O., Frey, F.A. and Grooms, D.G., 1986. Petrology of volcanic rocks from Kaula Island, Hawaii. *Contributions to Mineralogy and Petrology*, 94(4), pp.461-471.

Eales, H.V. and Cawthorn, R.G., 1996. The Bushveld Complex. In *Developments in petrology* (Vol. 15, pp. 181-229). Elsevier.

Eales, H.V. and Cawthorn, R.G., 1996. The bushveld complex. In *Developments in petrology* (Vol. 15, pp. 181-229). Elsevier.

Eglington, B.M. and Armstrong, R.A., 2004. The Kaapvaal Craton and adjacent orogens, southern Africa: A geochronological database and overview of the geological development of the craton. *South African Journal of Geology*, 107(1-2), pp. 13-32.

Ellam, R.M. and Harmon, R.S., 1990. Oxygen isotope constraints on the crustal contribution to the subduction-related magmatism of the Aeolian Islands, southern Italy. *Journal of Volcanology and Geothermal Research*, 44(1-2), pp.105-122.

Eriksson, P.G. and Clendenin, C.W., 1990. A review of the Transvaal Sequence, South Africa. *Journal of African Earth Sciences (and the Middle East)*, 10(1-2), pp. 101-116.

Eriksson, P.G., Hattingh, P.J. and Altermann, W., 1995. An overview of the geology of the Transvaal Sequence and Bushveld Complex, South Africa. *Mineralium Deposita*, 30(2), pp. 98-111.

Ferguson, J. & Botha, E., 1963. Some aspects of igneous layering in the basic zones of the Bushveld Complex. *South African Journal of Geology*, 66(1), pp.259-282.

Fekiacova, Z., Abouchami, W., Galer, S.J.G., Garcia, M.O. and Hofmann, A.W., 2007. Origin and temporal evolution of Ko'olau Volcano, Hawaii: Inferences from isotope data on the Ko'olau Scientific Drilling Project (KSDP), the Honolulu Volcanics and ODP Site 843. *Earth and Planetary Science Letters*, 261(1-2), pp. 65-83.

Fischer, L.A., Wang, M., Charlier, B., Namur, O., Roberts, R.J., Veksler, I.V., Cawthorn, R.G. and Holtz, F., 2016. Immiscible iron-and silica-rich liquids in the Upper Zone of the Bushveld Complex. *Earth and Planetary Science Letters*, 443, pp.108-117.

Forsyth, D.W., 1975. The early structural evolution and anisotropy of the oceanic upper mantle. *Geophysical Journal International*, 43(1), pp. 103-162.

Frey, F.A., Clague, D., Mahoney, J.J. and Sinton, J.M., 2000. Volcanism at the edge of the Hawaiian plume: Petrogenesis of submarine alkalic lavas from the North Arch volcanic field. *Journal of Petrology*, 41(5), pp. 667-691.

Gale, A., Dalton, C., Langmuir, C., Su, Y. and Schilling, J., 2013. The mean composition of ocean ridge basalts. *Geochemistry, Geophysics, Geosystems*, 14(3), pp. 489-518.

Garcia, M.O., Weis, D., Jicha, B.R., Ito, G. and Hanano, D., 2016. Petrology and geochronology of lavas from Kaula Volcano: Implications for rejuvenated volcanism of the Hawaiian mantle plume. *Geochimica et Cosmochimica Acta*, 185, pp .278-301.

Guilbert, J.M., 1962. The Origin of the Chromitites Below the Steelpoort Main Seam of the Bushveld Complex. The University of Wisconsin-Madison.

Gill, J.B., 1970. Geochemistry of Viti Levu, Fiji, and its evolution as an island arc. *Contributions to Mineralogy and Petrology*, 27(3), pp. 179-203.

Hamilton, J.O., 1977. Sr isotope and trace element studies of the Great Dyke and Bushveld mafic phase and their relation to early Proterozoic magma genesis in southern Africa. *Journal of Petrology*, 18(1), pp. 24-52.

Harvey, P.K. and Atkin, B.P., 1982. The estimation of mass absorption coefficients by Compton scattering: Extensions to the use of Rh K α Compton radiation and intensity ratios. *American Mineralogist*, 67(5-6), pp. 534-537.

Hatton, C.J., 1995. Mantle plume origin for the Bushveld and Ventersdorp magmatic provinces. *Journal of African Earth Sciences*, 21(4), pp. 571-577.

Hatton, C.J., 1998. The super ocean cycle. *Oceanographic Literature Review*, 9(45), pp. 1564-1565.

Hawkins, J.W., 1995. *The geology of the Lau Basin*. In Back arc Basins (pp. 63-138). Springer, Boston, MA.

Hegner, E., Kröner, A. and Hofmann, A.W., 1984. Age and isotope geochemistry of the Archaean Pongola and Usushwana suites in Swaziland, southern Africa: A case for crustal contamination of mantle-derived magma. *Earth and Planetary Science Letters*, 70(2), pp. 267-279.

Hoernle, K.A.J. and Schmincke, H.U., 1993. The role of partial melting in the 15-Ma geochemical evolution of Gran Canaria: A blob model for the Canary hotspot. *Journal of Petrology*, 34(3), pp. 599-626.

Hofmann, A.W., 1997. Mantle geochemistry: the message from oceanic volcanism. *Nature*, 385(6613), pp.219-229.

Hofmann, A.W., 2003. Sampling mantle heterogeneity through oceanic basalts: isotopes and trace elements. *Treatise on geochemistry*, 2, p.568.

Ishizuka, O., Taylor, R.N., Yuasa, M., Milton, J.A., Nesbitt, R.W., Uto, K. and Sakamoto, I., 2007. Processes controlling along-arc isotopic variation of the southern Izu–Bonin arc. *Geochemistry, Geophysics, Geosystems*, 8(6).

Jackson, M.G. and Dasgupta, R., 2008. Compositions of HIMU, EM1, and EM2 from global trends between radiogenic isotopes and major elements in ocean island basalts. *Earth and Planetary Science Letters*, 276(1-2), pp.175-186.

Jahn, B.M. and Condie, K.C., 1995. Evolution of the Kaapvaal Craton as viewed from geochemical and Sm • Nd isotopic analyses of intracratonic pelites. *Geochimica et Cosmochimica Acta*, 59(11), pp.2239-2258.

Janousek, V., Farrow, C.M. and Erban, V., 2006. Interpretation of whole-rock geochemical data in igneous geochemistry: Introducing Geochemical Data Toolkit (GCDkit). *Journal of Petrology*, 47(6), pp. 1255-1259.

Jansen, H., 1970. Volcanic rocks and associated sediments in the southern portion of the Waterberg basin.

Jimenez-Espinosa, R., Sousa, A.J. and Chica-Olmo, M., 1993. Identification of geochemical anomalies using principal component analysis and factorial kriging analysis. *Journal of Geochemical Exploration*, 46(3), pp.245-256.

Karig, D.E., 1971. Origin and development of marginal basins in the western Pacific. *Journal of Geophysical Research*, 76(11), pp. 2542-2561.

Keir-Sage, E., Leybourne, M.I., Jugo, P.J., Grobler, D.F. and Mayer, C.C., 2021. Assessing the extent of local crust assimilation within the Flatreef, northern limb of the Bushveld Igneous Complex, using sulfur isotopes and trace element geochemistry. *Mineralium Deposita*, 56, pp.91-102.

Kerr, R.A., 2013. *Geophysical exploration linking deep earth and backyard geology*.

Koppers, A.A., Gowen, M.D., Colwell, L.E., Gee, J.S., Lonsdale, P.F., Mahoney, J.J. and Duncan, R.A., 2011. New $^{40}\text{Ar}/^{39}\text{Ar}$ age progression for the Louisville hot spot trail and implications for inter-hot spot motion. *Geochemistry, Geophysics, Geosystems*, 12(12).

Kruger, F.J., 2005. Filling the Bushveld Complex magma chamber: Lateral expansion, roof and floor interaction, magmatic unconformities, and the formation of giant chromitite, PGE and Ti-V-magnetite deposits. *Mineralium Deposita*, 40(5), pp. 451-472.

Kruger, F.J., Cawthorn, R.G. and Walsh, K.L., 1987. Strontium isotopic evidence against magma addition in the Upper Zone of the Bushveld Complex. *Earth and Planetary Science Letters*, 84(1), pp. 51-58.

Kruger, F.J. and Marsh, J.S., 1982. Significance of $^{87}\text{Sr}/^{86}\text{Sr}$ ratios in the Merensky cyclic unit of the Bushveld Complex. *Nature*, 298(5869), pp. 53-55.

Kurz, M.D., le Roex, A.P. and Dick, H.J., 1998. Isotope geochemistry of the oceanic mantle near the Bouvet triple junction. *Geochimica et Cosmochimica Acta*, 62(5), pp.841-852.

Lautze, N., Thomas, D., Hinz, N., Apuzen-Ito, G., Frazer, N. and Waller, D., 2017. Play fairway analysis of geothermal resources across the State of Hawaii: 1. Geological, geophysical, and geochemical datasets. *Geothermics*, 70, pp. 376-392.

Leat, P., Fretwell, P., Tate, A., Larter, R., Martin, T., Smellie, J., Jokat, W. and Bohrmann, G., 2016. Bathymetry and geological setting of the South Sandwich Islands volcanic arc. *Antarctic Science*, 28(4), pp. 293-303.

Leat, P.T., Livermore, R.A., Millar, I.L. and Pearce, J.A., 2000. Magma supply in back-arc spreading centre segment E2, East Scotia Ridge. *Journal of Petrology*, 41(6), pp. 845-866.

Lee, C.T.A., Luffi, P., Plank, T., Dalton, H., and Leeman, W.P., 2009. Constraints on the depths and temperatures of basaltic magma generation on Earth and other terrestrial planets using new thermobarometers for mafic magmas. *Earth and Planetary Science Letters*, 279(1-2), pp.20-33.

Le Roux, P.J., Le Roex, A.P., Schilling, J.G., Shimizu, N., Perkins, W.W. and Pearce, N.J.G., 2002. Mantle heterogeneity beneath the southern Mid-Atlantic Ridge: trace element evidence for contamination of ambient asthenospheric mantle. *Earth and Planetary Science Letters*, 203(1), pp.479-498.

Lee, J.H., Yang, S.J., White, N.C., Shin, D. and Kim, E.J., 2022. Whole-rock geochemistry and mineral compositions of gabbroic rocks and the associated Fe–Ti (–V) oxide deposit in the Gonamsan intrusion, South Korea. *Ore Geology Reviews*, 148, p.105054.

Lenhardt, N. and Eriksson, P.G., 2012. Volcanism of the Palaeoproterozoic Bushveld large igneous Province: the Rooiberg Group, Kaapvaal Craton, South Africa. *Precambrian Research*, 214, pp. 82-94.

Li, H., Chen, Y., Zheng, H., Huang, P., Yang, P., Chen, Q., Weng, X., He, D. and Song, S., 2021. Effect of geological origin of apatite on reverse flotation separation of phosphate ores using phosphoric acid as depressant. *Minerals Engineering*, 172, p.107182.

Lipman, P.W., Clague, D.A., Moore, J.G. and Holcomb, R.T., 1989. South Arch volcanic field— Newly identified young lava flows on the sea floor south of the Hawaiian Ridge. *Geology*, 17(7), pp. 611-614.

Livermore, R., Cunningham, A., Vanneste, L. and Larter, R., 1997. Subduction influence on magma supply at the East Scotia Ridge. *Earth and Planetary Science Letters*, 150(3-4), pp. 261-275.

Lupton, J.E., Arculus, R.J., Resing, J., Massoth, G.J., Greene, R.R., Evans, L.J. and Buck, N., 2012. Hydrothermal activity in the Northwest Lau Back arc Basin: Evidence from water column measurements. *Geochemistry, Geophysics, Geosystems*, 13(5).

Lupton, J.E., Arculus, R.J., Greene, R.R., Evans, L.J. and Goddard, C.I., 2009. Helium isotope variations in seafloor basalts from the Northwest Lau Back arc Basin: Mapping the influence of the Samoan hotspot. *Geophysical Research Letters*, 36(17).

Lytle, M.L., Kelley, K.A., Hauri, E.H., Gill, J.B., Papia, D. and Arculus, R.J., 2012. Tracing mantle sources and Samoan influence in the northwestern Lau back-arc basin. *Geochemistry, Geophysics, Geosystems*, 13(10).

Mathez, E.A., Van Tongeren, J.A. and Schweitzer, J., 2013. On the relationships between the Bushveld Complex and its felsic roof rocks, part 1: Petrogenesis of Rooiberg and related felsites. *Contributions to Mineralogy and Petrology*, 166(2), pp. 435-449.

McCourt, S., 1995. The crustal architecture of the Kaapvaal crustal block South Africa, between 3.5 and 2.0 Ga. *Mineralium Deposita*, 30(2), pp. 89-97.

Merkle, R.K. and Von Gruenewaldt, G., 1986. Compositional variation of Co-rich pentlandite; relation to the evolution of the Upper Zone of the western Bushveld Complex, South Africa. *The Canadian Mineralogist*, 24(3), pp. 529-546.

Meschede, M., 1986. A method of discriminating between different types of mid-ocean ridge basalts and continental tholeiites with the Nb-Zr-Y diagram. *Chemical Geology*, 56(3-4), pp.207-218.

Naldrett, A.J., Wilson, A., Kinnaird, J. and Chunnett, G., 2009. PGE tenor and metal ratios within and below the Merensky Reef, Bushveld Complex: implications for its genesis. *Journal of Petrology*, 50(4), pp.625-659.

Naldrett, A., Kinnaird, J., Wilson, A., Yudovskaya, M. and Chunnett, G., 2011. Genesis of the PGE-enriched Merensky Reef and chromitite seams of the Bushveld Complex.

Niu, Y., 2021. Lithosphere thickness controls the extent of mantle melting, depth of melt extraction and basalt compositions in all tectonic settings on Earth—A review and new perspectives. *Earth-Science Reviews*, 217, p.103614.

Olsson, J.R., Söderlund, U., Hamilton, M.A., Klausen, M.B. and Helffrich, G.R., 2011. A late Archean radiating dyke swarm as possible clue to the origin of the Bushveld Complex. *Nature Geoscience*, 4(12), pp.865-869.

Olsson, J.R., Söderlund, U., Klausen, M.B. and Ernst, R.E., 2010. U–Pb baddeleyite ages linking major Archean dyke swarms to volcanic-rift forming events in the Kaapvaal craton (South Africa), and a precise age for the Bushveld Complex. *Precambrian Research*, 183(3), pp. 490-500.

Ozawa, A., Tagami, T. and Garcia, M.O., 2005. Unspiked K–Ar dating of the Honolulu rejuvenated and Ko ‘olau shield volcanism on O ‘ahu, Hawaii. *Earth and Planetary Science Letters*, 232(1-2), pp.1-11.

Pearce, J.A., 2008. Geochemical fingerprinting of oceanic basalts with applications to ophiolite classification and the search for Archean oceanic crust. *Lithos*, 100(1-4), pp.14-48.

Pearce, J.A., Kempton, P.D. and Gill, J.B., 2007. Hf–Nd evidence for the origin and distribution of mantle domains in the SW Pacific. *Earth and Planetary Science Letters*, 260(1-2), pp.98-114.

Pearce, J.A. and Parkinson, I.J., 1993. Trace element models for mantle melting: application to volcanic arc petrogenesis. Geological Society, London, Special Publications, 76(1), pp.373-403.

Pearce, J.A., and Peate, D.W., 1995. Tectonic implications of the composition of volcanic arc magmas. *Annual review of Earth and Planetary Sciences*, 23, pp. 251-286.

Pearce, J.A., 1983. Role of the sub-continental lithosphere in magma genesis at active continental margins.

Pelayo, A.M. and Wiens, D.A., 1989. Seismotectonics and relative plate motions in the Scotia Sea region. *Journal of Geophysical Research: Solid Earth*, 94(B6), pp. 7293-7320.

Plank, T., 2005. Constraints from thorium/lanthanum on sediment recycling at subduction zones and the evolution of the continents. *Journal of Petrology*, 46(5), pp. 921-944.

Plank, T., and Langmuir, C.H., 1998. The chemical composition of subducting sediment and its consequences for the crust and mantle. *Chemical Geology*, 145(3-4), pp. 325-394.

Pretorius, D.A., 1976. Handbook of strata-bound and stratiform ore deposits II. In *Regional studies and specific deposits, v. 6*. Amsterdam: Elsevier.

Robb, S.J. and Mungall, J.E., 2020. Testing emplacement models for the Rustenburg Layered Suite of the Bushveld Complex with numerical heat flow models and plagioclase geospeedometry. *Earth and Planetary Science Letters*, 534, p. 116084.

Scoates, J.S., Wall, C.J., Friedman, R.M., Weis, D., Mathez, E.A. and VanTongeren, J.A., 2021. Dating the Bushveld Complex: Timing of crystallization, duration of magmatism, and cooling of the world's largest layered intrusion and related rocks. *Journal of Petrology*, 62(2), p.eгаа107.

Scoon, R.N. and Teigler, B., 1994. Platinum-group element mineralization in the critical zone of the western Bushveld Complex; I, Sulfide-poor chromitites below the UG-2. *Economic Geology*, 89(5), pp. 1094-1121.

Scoon, R.N. and Mitchell, A.A., 2012. The Upper Zone of the Bushveld Complex at Roossenekal, South Africa: geochemical stratigraphy and evidence of multiple episodes of magma replenishment. *South African Journal of Geology*, 115(4), pp.515-534.

Schellart, W.P., Freeman, J., Stegman, D.R., Moresi, L. and May, D., 2007. Evolution and diversity of subduction zones controlled by slab width. *Nature*, 446(7133), pp.308-311.

Sharpe, M.R. and Hulbert, L.J., 1985. Ultramafic sills beneath the eastern Bushveld Complex; mobilized suspensions of early lower zone cumulates in a parental magma with boninitic affinities. *Economic Geology*, 80(4), pp. 849-871.

Sharpe, MR, Bahat, D. and Von Gruenewaldt, G., 1981. The concentric elliptical structure of feeder sites to the Bushveld Complex and possible economic implications. *South African Journal of Geology*, 84(3), pp. 239-244.

Shaw, A.M., Hauri, E.H., Fischer, T.P., Hilton, D.R. and Kelley, K.A., 2008. Hydrogen isotopes in Mariana arc melt inclusions: Implications for subduction dehydration and the deep-Earth water cycle. *Earth and Planetary Science Letters*, 275(1-2), pp.138-145.

Sherrod, D.R., Murai, T. and Tagami, T., 2007. New K–Ar ages for calculating end-of-shield extrusion rates at West Maui volcano, Hawaiian island chain. *Bulletin of volcanology*, 69(6), pp.627-642.

Skursch, O., Corfu, F., Tegner, C., Leshner, C.E., Andreasen, R., Hagen-Peter, G.A. and Vervoort, J.D., 2022. Zircon U–Pb chronology and Hf isotopes of the Lebowa Granite Suite and petrogenesis of the Bushveld Complex, South Africa. *Contributions to Mineralogy and Petrology*, 177(2), p.26.

Smith, W.D. and Maier, W.D., 2021. The geotectonic setting, age and mineral deposit inventory of global layered intrusions. *Earth-Science Reviews*, 220, p.103736.

Smol'kin, V.F. and Mokrushin, A.V., 2022. Paleoproterozoic Layered Intrusions of the Monchegorsk Ore District: Geochemistry and U–Pb, Sm–Nd, Re–Os Isotope Analysis. *Minerals*, 12(11), p.1432.

Spandler, C., Mavrogenes, J. and Arculus, R., 2005. Origin of chromitites in layered intrusions: Evidence from chromite-hosted melt inclusions from the Stillwater Complex. *Geology*, 33(11), pp.893-896.

Stern, C.R., and De Wit, M.J., 2003. Rocas Verdes ophiolites, southernmost South America: Remnants of progressive stages of development of oceanic-type crust in a continental margin back-arc basin. *Geological Society, London, Special Publications*, 218(1), pp.665-683.

Stern, R., 2002. Subduction zones. *Reviews of Geophysics*, 40(4), pp. 3-1-3-38.

Taniuchi, H., Kuritani, T. and Nakagawa, M., 2020. Generation of calc-alkaline andesite magma through crustal melting induced by emplacement of mantle-derived water-rich primary magma: Evidence from Rishiri Volcano, southern Kuril Arc. *Lithos*, 354, p.105362.

Tegner, C., Cawthorn, R. and Kruger, F., 2006. Cyclicity in the Main and Upper Zones of the Bushveld Complex, South Africa: Crystallization from a Zoned Magma Sheet. *Journal of Petrology*, 47(11), pp. 2257-2279.

Stracke, A., 2012. Earth's heterogeneous mantle: A product of convection-driven interaction between crust and mantle. *Chemical Geology*, 330, pp.274-299.

Tian, L., Castillo, P.R., Hilton, D.R., Hawkins, J.W., Hanan, B.B. and Pietruszka, A.J., 2011. Major and trace element and Sr-Nd isotope signatures of the northern Lau Basin lavas: Implications for the

composition and dynamics of the back-arc basin mantle. *Journal of Geophysical Research: Solid Earth*, 116(B11).

Tinker, J., De Wit, M. and Grotzinger, J., 2002. Seismic stratigraphic constraints on Neoproterozoic–Paleoproterozoic evolution of the western margin of the Kaapvaal Craton, South Africa. *South African Journal of Geology*, 105(2), pp. 107-134.

Tollstrup, D.L. and Gill, J.B., 2005. Hafnium systematics of the Mariana arc: Evidence for sediment melt and residual phases. *Geology*, 33(9), pp. 737-740.

Trusdell, F.A., Moore, R.B., Sako, M., White, R.A., Koyanagi, S.K., Chong, R., and Camacho, J.T., 2005. The 2003 eruption of Anatahan Volcano, Commonwealth of the Northern Mariana Islands: chronology, volcanology, and deformation. *Journal of Volcanology and Geothermal Research*, 146(1-3), pp.184-207.

Tukey, J.W., 1977. *Exploratory data analysis* (Vol. 2, pp. 131-160).

Turner, S., Hawkesworth, C., Rogers, N., Bartlett, J., Worthington, T., Hergt, J., Pearce, J. and Smith, I., 1997. 238U-230Th disequilibria, magma petrogenesis, and flux rates beneath the depleted Tonga-Kermadec island arc. *Geochimica et Cosmochimica Acta*, 61(22), pp. 4855-4884.

Uken, R., 1998. *The geology and structure of the Bushveld Complex metamorphic aureole in the Olifants River area* (Doctoral dissertation).

Van Tongeren, J.A. and Mathez, E.A., 2013. Incoming magma composition and style of recharge below the Pyroxenite Marker, Eastern Bushveld Complex, South Africa. *Journal of Petrology*, 54(8), pp. 1585-1605.

VanTongeren, J.A. and Mathez, E.A., 2012. Large-scale liquid immiscibility at the top of the Bushveld Complex, South Africa. *Geology*, 40(6), pp.491-494.

VanTongeren, J.A., 2018. Mixing and unmixing in the Bushveld Complex magma chamber. *Processes and Ore Deposits of Ultramafic-Mafic Magmas through Space and Time*, pp.113-138.

Von Brunn, V. and Hobday, D.K., 1976. Early Precambrian tidal sedimentation in the Pongola Supergroup of South Africa. *Journal of Sedimentary Research*, 46(3), pp. 670-679.

Von Gruenewaldt, G., 1979. A review of some recent concepts of the Bushveld Complex, with particular reference to sulfide mineralization. *The Canadian Mineralogist*, 17(2), pp. 233-256.

Von Gruenewaldt, G., 1973. The modified differentiation index and the modified crystallization index as parameters of differentiation in layered intrusions. *South African Journal of Geology*, 76(1), pp. 53-61.

Von Gruenewaldt, G. & Hatton, C.J., 1987. Platinum-group metals-a resource in the tailings of chromium mines in South Africa. *Journal of the Southern African Institute of Mining and Metallurgy*, 87(9), pp.265-268.

Wager, L.R. and Brown, G.M., 1967. Layered igneous rocks. WH Freeman.

Walraven, F. and Wolmarans LG., 1979. *Stratigraphy of the upper part of the Rustenburg Layered Suite, Bushveld Complex, in western Transvaal*.

Walraven, F., Armstrong, R.A., and Kruger, F.J., 1990. A chronostratigraphic framework for the north-central Kaapvaal craton, the Bushveld Complex and the Vredefort structure. *Tectonophysics*, 171(1-4), pp.23-48.

Walraven, F. & Hattingh, E., 1993. Geochronology of the Nebo granite, Bushveld complex. *South African Journal of Geology*, 96(1), pp. 31-41.

Wang, P. and Glover, L., 1992. A tectonics test of the most commonly used geochemical discriminant diagrams and patterns. *Earth-Science Reviews*, 33(2), pp. 111-131.

Watchorn, M.B., 1980. Fluvial and tidal sedimentation in the 3000 Ma Mozaan basin, South Africa. *Precambrian Research*, 13(1), pp. 27-42.

Webb, S.J., Ashwal, L.D. and Cawthorn, R.G., 2011. Continuity between eastern and western Bushveld Complex, South Africa, confirmed by xenoliths from kimberlite. *Contributions to Mineralogy and Petrology*, 162(1), pp.101-107.

Weilers, B.F., 1990. *A review of the Pongola Supergroup and its setting on the Kaapvaal Craton*. University of the Witwatersrand.

Wignall, P., 2001. Large igneous provinces and mass extinctions. *Earth-Science Reviews*, 53(1-2), pp. 1-33.

Wilson, M., 1989. Review of igneous petrogenesis: A global tectonic approach. *Terra Nova*, 1(2), pp. 218-222.

Wilson, M.G.C. and Anhaeusser, C.R., 1998. The Mineral Resources of (p. 740). Council for Geosciences, South Africa.

Xia, L. and Li, X., 2019. Basalt geochemistry as a diagnostic indicator of tectonic setting. *Gondwana Research*, 65, pp.43-67.

Xia, F., Wang, H. and Jia, Y., 2014. Rediscovering black phosphorus as an anisotropic layered material for optoelectronics and electronics. *Nature Communications*, 5(1).

Yao, Z., Mungall, J.E. and Jenkins, M.C., 2021. The Rustenburg Layered Suite formed as a stack of mush with transient magma chambers. *Nature Communications*, 12(1), p.505.

Yuan, Q., Namur, O., Fischer, L., Roberts, R., Lü, X. and Charlier, B., 2017. Pulses of plagioclase-laden magmas and stratigraphic evolution in the Upper Zone of the Bushveld Complex, South Africa. *Journal of Petrology*, 58(8), pp. 1619-1643.

Yudovskaya, M.A., Kinnaird, J.A., Costin, G., McCreesh, M., Shilovskikh, V., Kovalchuk, E. and Kuzmin, D., 2022. Formation of spinel-orthopyroxene symplectites by reactive melt flow: Examples from the northern Bushveld Complex and implications for mineralization in layered intrusions. *Economic Geology*, 117(8), pp.1935-1960.

Zhang, Z.J., Zhou, Y. and Zhang, P., 2023. Crucial Geochemical Signal Identification for Cu-Fertile Magmas in Paleo-Tethyan Arc Based on Machine Learning. *Mathematical Geosciences*, pp.1-30.

Zellmer, K.E. and Taylor, B., 2001. A three-plate kinematic model for Lau Basin opening. *Geochemistry, Geophysics, Geosystems*, 2(5).

Zintwana, M.P., Cawthorn, R.G., Ashwal, L.D., Roelofse, F. and Cronwright, H., 2012. Mercury in the Bushveld complex, South Africa, and the Skaergaard intrusion, Greenland. *Chemical Geology*, 320, pp.147-155.